



Aerosol characteristics and particle production in the upper troposphere over the Amazon Basin

Meinrat O. Andreae^{1,12}, Armin Afchine², Rachel Albrecht³, Bruna Amorim Holanda¹, Paulo Artaxo⁴, Henrique M. J. Barbosa⁴, Stephan Borrmann¹, Micael A. Cecchini^{5,3}, Anja Costa², Maximilian Dollner^{9,13}, Daniel Fütterer⁶, Emma Järvinen¹⁰, Tina Jurkat⁶, Thomas Klimach¹, Tobias Konemann¹, Christoph Knote⁹, Martina Krämer², Trismono Krisna⁸, Luiz A. T. Machado⁵, Stephan Mertes⁷, Andreas Minikin^{6,16}, Christopher Pöhlker¹, Mira L. Pöhlker¹, Ulrich Pöschl¹, Daniel Rosenfeld¹⁴, Daniel Sauer⁶, Hans Schlager⁶, Martin Schnaiter¹⁰, Johannes Schneider¹, Christiane Schulz¹, Antonio Spanu^{6,13}, Vinicius B. Sperling⁵, Christiane Voigt^{6,15}, Adrian Walser^{9,6}, Jian Wang^{1,11}, Bernadett Weinzierl^{6,13}, Manfred Wendisch⁸, and Helmut Ziereis⁶

¹Biogeochemistry, Multiphase Chemistry, and Particle Chemistry Departments, Max Planck Institute for Chemistry, Mainz, Germany

²Forschungszentrum Jülich, Jülich, Germany

³Instituto de Astronomia, Geofísica e Ciências Atmosféricas, Universidade de São Paulo, São Paulo, Brazil

⁴Institute of Physics, University of São Paulo, São Paulo, Brazil

⁵National Institute for Space Research (INPE), São José dos Campos, Brazil

⁶German Aerospace Center (DLR), Institute of Atmospheric Physics (IPA), Weßling, Germany

⁷Leibniz Institute for Tropospheric Research, Leipzig, Germany

⁸Leipzig Institute for Meteorology, Leipzig University, Leipzig, Germany

⁹Meteorological Institute, Ludwig Maximilian University, Munich, Germany

¹⁰Institute for Meteorology and Climate Research, Karlsruhe Institute of Technology, Karlsruhe, Germany

¹¹Brookhaven National Laboratory, Upton, NY, USA

¹²Scripps Institution of Oceanography, University of California San Diego, La Jolla, CA, USA

¹³University of Vienna, Aerosol Physics and Environmental Physics, Vienna, Austria

¹⁴Institute of Earth Sciences, The Hebrew University of Jerusalem, Jerusalem, Israel

¹⁵Institute of Atmospheric Physics (IPA), Johannes Gutenberg University, Mainz, Germany

¹⁶German Aerospace Center (DLR), Flight Experiments, Oberpfaffenhofen, Germany

Correspondence: Meinrat O. Andreae (m.andreae@mpic.de)

Received: 25 July 2017 – Discussion started: 1 August 2017

Revised: 8 November 2017 – Accepted: 5 December 2017 – Published: 25 January 2018

Abstract. Airborne observations over the Amazon Basin showed high aerosol particle concentrations in the upper troposphere (UT) between 8 and 15 km altitude, with number densities (normalized to standard temperature and pressure) often exceeding those in the planetary boundary layer (PBL) by 1 or 2 orders of magnitude. The measurements were made during the German–Brazilian cooperative aircraft campaign ACRIDICON–CHUVA, where ACRIDICON stands for “Aerosol, Cloud, Precipitation, and Radiation Interactions and Dynamics of Convective Cloud Systems” and

CHUVA is the acronym for “Cloud Processes of the Main Precipitation Systems in Brazil: A Contribution to Cloud Resolving Modeling and to the GPM (global precipitation measurement)”, on the German High Altitude and Long Range Research Aircraft (HALO). The campaign took place in September–October 2014, with the objective of studying tropical deep convective clouds over the Amazon rainforest and their interactions with atmospheric trace gases, aerosol particles, and atmospheric radiation.

Aerosol enhancements were observed consistently on all flights during which the UT was probed, using several aerosol metrics, including condensation nuclei (CN) and cloud condensation nuclei (CCN) number concentrations and chemical species mass concentrations. The UT particles differed sharply in their chemical composition and size distribution from those in the PBL, ruling out convective transport of combustion-derived particles from the boundary layer (BL) as a source. The air in the immediate outflow of deep convective clouds was depleted of aerosol particles, whereas strongly enhanced number concentrations of small particles (< 90 nm diameter) were found in UT regions that had experienced outflow from deep convection in the preceding 5–72 h. We also found elevated concentrations of larger (> 90 nm) particles in the UT, which consisted mostly of organic matter and nitrate and were very effective CCN.

Our findings suggest a conceptual model, where production of new aerosol particles takes place in the continental UT from biogenic volatile organic material brought up by deep convection and converted to condensable species in the UT. Subsequently, downward mixing and transport of upper tropospheric aerosol can be a source of particles to the PBL, where they increase in size by the condensation of biogenic volatile organic compound (BVOC) oxidation products. This may be an important source of aerosol particles for the Amazonian PBL, where aerosol nucleation and new particle formation have not been observed. We propose that this may have been the dominant process supplying secondary aerosol particles in the pristine atmosphere, making clouds the dominant control of both removal and production of atmospheric particles.

1 Introduction

Aircraft measurements in the upper troposphere (UT) have consistently shown large regions with very high aerosol particle number concentrations, typically in the tens of thousands of particles per cm^3 , with the strongest enhancements reported in tropical and subtropical regions (Clarke et al., 1999; Andreae et al., 2001; de Reus et al., 2001; Krejci et al., 2003; Lee et al., 2003; Young et al., 2007; Ekman et al., 2008, 2012; Yu et al., 2008; Froyd et al., 2009; Weigelt et al., 2009; Borrmann et al., 2010; Clarke and Kapustin, 2010; Mirme et al., 2010; Waddicor et al., 2012; Reddington et al., 2017; Rose et al., 2017). Twohy et al. (2002) observed particle concentrations up to $45\,000\text{ cm}^{-3}$ in the UT over North America and suggested that they had been formed in situ from gas-phase precursors brought up by deep convection. Weigel et al. (2011) found similar concentrations in the UT over tropical America, Africa, and Australia, which they attributed to new particle formation from sulfuric acid and possibly organics. Most of these elevated aerosol concentrations are in the nucleation- and Aitken-mode size ranges, i.e., at

particle diameters smaller than about 90 nm, with maxima typically between 20 and 60 nm (e.g., de Reus et al., 2001; Lee et al., 2003; Weigel et al., 2011; Waddicor et al., 2012). They generally occur as layers of a few hundred to a few thousand meters in thickness, often extending over large horizontal distances, and are found over continents as well as over the most remote oceanic regions. The high concentrations of these aerosols in the UT are of great significance for the climate system, because they make this region an important reservoir of particles for the transport both downward into the planetary boundary layer (PBL) (Clarke et al., 1999, 2013; J. Wang et al., 2016) and upward into the tropical transition layer (TTL) and the lower stratosphere (Brock et al., 1995; Weigel et al., 2011; Randel and Jensen, 2013), where they can grow into the optically and cloud-microphysically active size range.

Based on observations over the remote Pacific and supported by extensive subsequent investigations, Clarke and coworkers proposed an aerosol life cycle model in which convection lifts marine boundary layer air with nucleation precursor molecules into the upper troposphere, where nucleation takes place in the detrainment zone, followed by aerosol growth and descent through the troposphere into the boundary layer (Clarke, 1992, 1993; Clarke et al., 1998). These measurements were carried out over the oceans and implied sulfuric acid, likely from dimethyl sulfide and sulfur dioxide oxidation, as the molecule driving aerosol nucleation. Clarke and Kapustin (2002) wrote that “the tropics commonly have low aerosol mass but very high number concentrations in the upper free troposphere (FT) that appear to form from sulfuric acid (nucleation) in convective regions and near cloud edges. These age and subside to become effective cloud condensation nuclei (CCN) when mixed into the marine boundary layer”.

When enhanced UT particle concentrations in the accumulation mode (larger than about 90 nm) have been observed, the enrichment was frequently attributed to sources of sulfur dioxide (SO_2) and other combustion emissions, especially biomass burning (BB), based on correlations with combustion tracers, such as carbon monoxide (CO), and air mass trajectories (e.g., Andreae et al., 2001; Clarke and Kapustin, 2010; Weigel et al., 2011; Clarke et al., 2013). After having been lofted to the UT by deep convection, particles in this size range can be transported over hemispheric distances, because removal processes are very inefficient at these altitudes (Andreae et al., 2001; Clarke and Kapustin, 2010).

The enhanced particle concentrations in the ultrafine (UF) size range (here defined as particles smaller than 90 nm), on the other hand, cannot be explained by transport from the lower troposphere, since they by far exceed typical concentrations in the PBL and these particles generally are too short-lived to survive deep convection and long-range transport. Therefore, nucleation and new particle formation (NPF) from gas-phase precursors brought into the UT by the outflow from deep convection have been proposed as the source

of these enhanced UF particle concentrations (Clarke et al., 1999; Twohy et al., 2002; Krejci et al., 2003; Lee et al., 2003; Young et al., 2007; Froyd et al., 2009; Merikanto et al., 2009; Weigel et al., 2011; Waddicor et al., 2012). High actinic flux, low pre-existing aerosol surface area, and low temperatures make the UT an environment that is highly conducive to nucleation and NPF.

The nature of the gaseous species involved in particle nucleation and growth has been the subject of some debate (Kulmala et al., 2006). Most of the earlier papers attributed the nucleation to H_2SO_4 in combination with H_2O and NH_3 , especially in marine and anthropogenically influenced regions, where a sufficient supply of sulfur gases from either dimethyl sulfide (DMS) oxidation or pollution sources is available (e.g., Clarke et al., 1999; Twohy et al., 2002; Lee et al., 2003; Merikanto et al., 2009). However, there is growing evidence that, in most cases, there is not enough H_2SO_4 available to explain the observed rates of growth. Therefore, the condensation of organics has been proposed to dominate particle growth after nucleation, especially over unpolluted vegetated areas such as the Amazon Basin (Ekman et al., 2008; Weigel et al., 2011; Waddicor et al., 2012; Murphy et al., 2015).

In fact, H_2SO_4 does not even have to be the initially nucleating species in all cases. Recent studies conducted as part of the Cosmics Leaving Outdoor Droplets (CLOUD) project have shown that organic vapors alone can produce particle nucleation (Kirkby et al., 2016) and that nearly all nucleation throughout the present-day atmosphere involves ammonia or biogenic organic compounds (Dunne et al., 2016). Highly oxygenated multifunctional organic compounds (HOMs) formed by ozonolysis of α -pinene were found to nucleate aerosol particles, especially when aided by ions. Extremely low-volatility organic compounds (ELVOCs, which may be at least in part identical to HOMs) are also produced from the O_3 - or OH-initiated oxidation of biogenic volatile organic compounds (BVOCs) (Jokinen et al., 2015). Following nucleation by the lowest-volatility species, with increasing particle size, the condensation of progressively more volatile compounds is facilitated by the decrease in the Kelvin effect (Tröstl et al., 2016). These laboratory studies were confirmed by field observations at a mountain site in the free troposphere (Jungfraujoch, Switzerland), where NPF was found to take place through condensation of HOMs, in this case from anthropogenic precursor VOCs, within 1–2 days after being lofted from the PBL (Bianchi et al., 2016).

The production of particles in the UT may be a key component of the atmospheric budget of optically and cloud-microphysically active aerosols, especially in pristine or relatively unpolluted regions, as was suggested in a modeling study by Merikanto et al. (2009). Studies in the Amazon have shown that NPF almost never takes place under clean conditions in the PBL over the Amazon Forest (Zhou et al., 2001; Martin et al., 2010; Andreae et al., 2015) and rarely occurs over the taiga forest in remote Siberia (Heintzenberg

et al., 2011, and unpublished data). Over the Amazon, downward transport of aerosols from the FT has been identified as an important, if not the dominant, source of particles to the lower troposphere (LT) (Zhou et al., 2001; Roberts et al., 2001; J. Wang et al., 2016). In turn, the concentrations of aerosols in the PBL have a pronounced influence on the characteristics of convection and thereby influence cloud radiative forcing and atmospheric dynamics (Sherwood, 2002; Rosenfeld et al., 2008, 2014; Fan et al., 2012; Stolz et al., 2015; Cecchini et al., 2017).

Understanding the processes that control the aerosol burden in the pristine atmosphere is an essential prerequisite for assessing the magnitude of the climate forcing by anthropogenic aerosols, since it forms the baseline from which anthropogenic forcing is derived. Because of the strong non-linearity of the relationship between particle number concentration and cloud-mediated aerosol effects, the uncertainty regarding the aerosol burden of the pristine atmosphere is the largest contributor to the uncertainty in estimates of anthropogenic aerosol climate forcing (Carslaw et al., 2013, 2017). For example, model calculations suggest that the inclusion of ion-induced particle formation from biogenic HOMs in the natural atmosphere reduces the cloud-albedo radiative forcing by about one-third because of the higher albedo calculated for the clouds in the pre-industrial atmosphere (Gordon et al., 2016).

In this paper, we present the results of aerosol measurements made in the upper troposphere across the Amazon Basin during the ACRIDICON–CHUVA campaign on the German High Altitude and Long Range Research Aircraft (HALO) during September and October 2014 (Wendisch et al., 2016). ACRIDICON stands for “Aerosol, Cloud, Precipitation, and Radiation Interactions and Dynamics of Convective Cloud Systems”; CHUVA is the acronym for “Cloud Processes of the Main Precipitation Systems in Brazil: A Contribution to Cloud Resolving Modeling and to the GPM (global precipitation measurement)”. We characterize these UT aerosol particles in terms of their microphysical and chemical properties, and contrast them with the LT aerosols. From their spatial distribution and their relationship to deep convection and convective outflow, we derive hypotheses about their mode of formation. Finally, we discuss the role of upper tropospheric aerosol formation in the life cycle of the atmospheric aerosol.

2 Methods

The observations discussed in this paper were collected aboard the HALO aircraft (<http://www.halo.dlr.de/>), a modified ultra-long-range business jet G550 (manufactured by Gulfstream, Savannah, USA). Because of its high ceiling altitude (up to 15 km) and long endurance (up to 8 h with a scientific payload), HALO is capable of collecting airborne measurements of cloud microphysical and radiative proper-

ties, aerosol characteristics, and chemical tracer compounds in the upper troposphere, in and around tropical deep convective clouds. The aircraft and its instrumentation are described in the ACRIDICON-CHUVA overview paper by Wendisch et al. (2016).

In situ meteorological and avionics data were obtained at 1 Hz from the BASIC HALO Measurement And Sensor System (BAHAMAS). This data set includes pressure, temperature, wind direction and speed, humidity, water vapor mixing ratio, aircraft position, and altitude. All concentration data have been normalized to standard temperature and pressure (STP; $T = 273.15$ K and $p = 1000$ hPa).

2.1 The HALO aerosol submicrometer inlet

All aerosol sampling was conducted using the HALO aerosol submicrometer inlet (HASI), designed for HALO by the German Aerospace Center (DLR) in collaboration with envirocope GmbH (Frankfurt, Germany) with the aim of providing up to 30 L min^{-1} sample air flow (divided over four sample lines) to aerosol instruments mounted inside the aircraft cabin. HASI samples the air on top of the fuselage outside of the aircraft boundary layer. The air stream is aligned in the inlet using a front shroud and decelerated by a factor of approximately 15. Four sample tubes with 6.2 mm outer diameter and frontal diffusors protrude into the decelerated air stream. The design goal is to allow regulating the sample airflow in each of the four sample lines to achieve isokinetic sampling conditions according to the actual speed of the aircraft. Since the automatic adjustment had not been implemented at the time of the field experiment, the flow was fixed to values providing near-isokinetic sampling for typical flight conditions based on geometric considerations and preliminary flow simulations for the initial design of the inlet. The geometric design should prevent large cloud droplets and ice crystals from entering the sample lines directly. The inlet position is located in the shadow zone for larger ice crystals, which precludes artifacts by shattering and breakup of larger ice particles at the inlet tip (Witte, 2008). Judging from the first measurements with HASI, it appears that measurements of interstitial aerosol in liquid clouds are affected by artifacts, while in ice clouds there is no indication for such artifacts. The data selection procedures to exclude artifacts are discussed in Sect. 2.2.

2.2 Condensation nuclei

Condensation nuclei (CN) number concentrations (N_{CN}) were measured using the Aerosol Measurement System (AMETYST). This system was designed to provide an instrument package for HALO to measure basic microphysical properties of the ambient atmospheric aerosol (integral number concentration, submicrometer size distribution, fraction of non-volatile particles, and particle absorption coefficient). AMETYST includes four butanol-based condensa-

tion particle counters (CPCs, modified Grimm CPC 5.410 by Grimm Aerosol Technik, Ainring, Germany) with flow rates of 0.6 and 0.3 L min^{-1} , configured with different nominal lower cutoff diameters at 4 and 10 nm (set via the temperature difference between saturator and condenser). In addition, two differential mobility analyzers (Grimm M-DMAs) with a nominal size range between 5.5 and 350 nm using ^{241}Am radioactive sources as aerosol neutralizers are part of the system.

Two of the four CPCs are generally set to measure the integral particle concentrations, while for the two other CPCs the configuration is selectable depending on measurement priorities. They can be used either as detectors for the DMAs or for additional integral concentration measurements. The DMAs can either be set to select specific diameters or operated as a differential mobility particle sizer (DMPS) system scanning the size distribution at predefined diameter steps. The integration times at each step have to be chosen such that meaningful statistics can be achieved depending on the measurement strategy. AMETYST also includes an optional thermodenuder, which heats a section of the sample line to 250°C for the measurement of the non-volatile particle fraction.

The raw CPC data are corrected using an empirical, pressure-dependent flow correction to account for changes in the volume flow at different flight altitudes (D. Fütterer, PhD thesis, in preparation). Particle losses in the sampling lines have been estimated with the particle loss calculator by von der Weiden et al. (2009). Accounting for these effects leads to an increase of the effective cutoff diameter for all CPCs. The effective cutoffs are calculated as a convolution of the pressure-dependent CPC counting efficiency and the size-dependent transmission efficiency of the sample lines. The data reported here were taken by the CPC operated at 0.6 L min^{-1} , with a nominal cutoff of 4 nm. Due to inlet losses, the effective cutoff diameter increases to 9.2 nm at 1000 hPa, 11.2 nm at 500 hPa, and 18.5 nm at 150 hPa. This implies that the present setup of AMETYST essentially does not detect nucleation-mode particles below 10 nm at low altitudes and below 20 nm in the UT. Typical uncertainties of CPC number concentration measurements are estimated to be of the order of 5 to 10 % (Petzold et al., 2011).

To eliminate artifacts from cloud hydrometeors and bias from local pollution, we excluded measurements using the following criteria. (1) All cloud passages below 6 km were removed. During passages through water clouds, the CPCs showed erratic, unreasonably high number concentrations that are probably caused by droplet shattering at the probe tip. Cloud passages were identified from the observation of elevated concentrations of particles $> 3 \mu\text{m}$ using the hydrometeor probes (see below). (2) In the mixed-phase and ice-phase regimes, all cloud passages were inspected for possible shattering artifacts, and suspect data were rejected. Cloud passages through pure ice clouds did not show evidence of hydrometeor shattering. (3) The flight segments

during departure and approach to Manaus airport were removed to avoid pollution from the airport and its surroundings. (4) Flights segments through the Manaus urban plume, which was sampled during joint flight experiments with the DOE G1 aircraft and in the course of tracer studies in the PBL, were excluded in order to provide a sampling representative of the dry season atmosphere over the Amazon Basin away from local pollution. (5) Fire plumes that were sampled deliberately to study fresh emissions were not analyzed for this paper. (6) Segments where the aircraft passed through its own exhaust were also excluded from the analyzed data set.

2.3 Aitken-mode aerosol size spectra

To obtain aerosol size spectra for particles up to 300 nm diameter, the DMAs within AMETYST were connected to two of the CPCs and operated in scanning mode for selected flight sequences (especially during longer flight legs, where relatively homogeneous conditions can be assumed). The size range covered by the scans was typically between 20 and 300 nm diameter in nine steps. To improve the time resolution, the two DMPS were usually set to scan the same sequence in opposite directions. The DMPS data were then analyzed by taking into account a correction for multiple charges following Wiedensohler (1988) after normalizing the measured concentrations to standard atmospheric conditions. To derive modal parameters for the particle size distribution, a bimodal log-normal fit to the data points was computed.

2.4 Accumulation-mode aerosol particles

For the purposes of this paper, we define the accumulation mode as the particle size range from 90 to 600 nm and the total number concentration in this size class as the accumulation-mode number concentration, N_{acc} . The particle concentrations in this range were measured with an optical particle counter (OPC), the Ultra-High Sensitivity Aerosol Spectrometer (UHSAS; Droplet Measurement Technologies, Inc., Longmont, CO, USA) (Cai et al., 2008; Brock et al., 2011). The UHSAS combines a high-power infrared laser ($\lambda = 1054$ nm) and a large solid angle range in a sideways direction for the detection of light scattered by individual particles. Due to the resulting almost-monotonic increase of instrument response with particle size, the UHSAS enables high-resolution measurements (100 selectable channels). The high laser intensity enables the detection of particle diameters down to about 60 nm, with the upper limit being approximately 1 μm . Due to changes in the laser and instrument parameter settings during the campaign, only the size range from ~ 90 to ~ 600 nm is considered here. Particle concentrations of up to 3000 cm^{-3} are recorded without significant counting coincidence losses (Cai et al., 2008). The airborne instrument version is mounted in an underwing canister and equipped with a forward-facing diffusor inlet. The slowed airflow is subsampled by a second inlet at approxi-

mately isokinetic conditions. The sample is not actively dried before the measurement but due to combined heating effects the measured diameters can be assumed to be close to their dry diameters (Chubb et al., 2016). The UHSAS was calibrated with monodisperse polystyrene latex (PSL) spheres of known refractive index and size. The evaluation of the OPC calibration results and the derivation of realistic uncertainty estimates for the OPC size distributions are outlined in a recent study by Walser et al. (2017).

2.5 Cloud condensation nuclei

The number concentration of CCN (N_{CCN}) was measured with a continuous-flow streamwise thermal gradient CCN counter (CCNC, model CCN-200, DMT, Longmont, CO, USA) (Roberts and Nenes, 2005; Rose et al., 2008). The CCN-200 consists of two columns, in which particles with critical supersaturations (S) above a preselected value are activated and form water droplets. Droplets with diameters $\geq 1\ \mu\text{m}$ are detected by an OPC at the exit of the column. The inlet flow rate of the column was 0.5 L min^{-1} with a sheath-to-aerosol flow ratio of 10. The water pump was operated at the CCNC setting of “high” liquid flow. Variations in ambient pressure have a strong influence on S inside the CCNC. For this purpose, a novel constant pressure inlet without significant particle losses was deployed on HALO. The instrument was calibrated before, during, and after the campaign at different pressures and flow rates according to Rose et al. (2008). For the data used in this study, we sampled from the HASI inlet and measured at $S = 0.52 \pm 0.05\%$ and a time resolution of 1 Hz.

Since the flow in the instrument was kept constant for the data used here, the error in S was dominated by the calibration uncertainty, as described by Pöhlker et al. (2016); it is estimated to be in the range of 10%. According to Krüger et al. (2014), the error in N_{CCN} is based on the counting error of the measured particle number and is 10% of N_{CCN} for large concentrations; given that mostly low concentrations prevailed, the mean error was about 20% of N_{CCN} .

2.6 Cloud droplet and ice particle measurements

While measurements of liquid water and ice hydrometeor concentrations are not a subject of this paper, they were used to determine whether the aircraft was sampling inside clouds and if so, whether the cloud particles were liquid or frozen. For this purpose, we used data from the Cloud Droplet Probe (CDP) and the Cloud and Aerosol Spectrometer with Depolarization (CAS-DPOL), both of which are based on the principle of forward scattering detection. The CDP detects particles with sizes from 3 to 50 μm and classifies them into size histograms of bin widths between 1 and 2 μm . The CAS-DPOL covers the size range of 0.6–50 μm in 17 bins of varying width. The probes are described in Voigt

et al. (2017) and probes and data correction techniques in Weigel et al. (2016).

Information regarding the ice particle properties was obtained from the Particle Habit Imaging and Polar Scattering probe (PHIPS-HALO), a single-particle cloud probe that measures microphysical and angular light scattering properties of individual particles (Abdelmonem et al., 2016). The instrument is composed of a stereoscopic imager that takes two brightfield images from the particles under a viewing angle difference of 120° . Simultaneously to collecting the images, the scattering component of the instrument measures the angular scattering function of the particles from 18 to 170° with an angular resolution of 8° . The optical resolution of the imager is about $2.5\ \mu\text{m}$.

2.7 Aerosol mass spectrometer

For in situ chemical analysis of submicrometer aerosol particles, a compact time-of-flight aerosol mass spectrometer (C-ToF-AMS) (Drewnick et al., 2005; Schmale et al., 2010) was operated aboard HALO. The C-ToF-AMS was sampling from the HASI inlet for ambient aerosol measurements. The aerosol particles enter the instrument via a pressure-controlled inlet and are focused into a narrow beam by an aerodynamic lens. In the vacuum chamber, the particles are flash vaporized and the resulting gas-phase molecules are ionized by electron impact. The ions are guided into the time-of-flight mass spectrometer, separated by their mass-to-charge ratio, and detected by a microchannel plate detector. The C-ToF-AMS was operated with a time resolution of 30 s, providing mass concentrations of particulate organics, nitrate, sulfate, chloride, and ammonium.

2.8 Refractory black carbon

An eight-channel Single Particle Soot Photometer (SP2; Max Planck Institute for Chemistry) was used to detect and quantify refractory black carbon (rBC) particles using laser-induced incandescence (Stephens et al., 2003; Schwarz et al., 2006). The instrument measures the time-dependent scattering and incandescence signals produced by individual aerosol particles when crossing a laser beam (Nd:YAG; $\lambda = 1064\ \text{nm}$). The particles containing rBC cores absorb the laser light and evaporate within the optical chamber, emitting thermal radiation (incandescence). The peak intensity of the incandescence signal, recorded by two photomultiplier tubes over two different wavelength intervals, is linearly proportional to the mass of the rBC in the particle (Laborde et al., 2013). At the detector settings used, the instrument is sensitive to rBC cores in the nominal size range of $70\text{--}500\ \text{nm}$ mass-equivalent diameter, assuming a density of $1.8\ \text{g cm}^{-3}$. The SP2 also detects the intensity of the light scattered by the particles using an avalanche photodetector in order to determine the optical size of purely scattering particles in the diameter range of $200\text{--}400\ \text{nm}$.

The SP2 incandescence signal was calibrated several times (at the beginning, during, and at the end of the campaign) using size-selected fullerene soot particles. The scattering signal was calibrated using either spherical polystyrene latex size standards (208 , 244 , and $288\ \text{nm}$) or ammonium sulfate particles of different diameters selected by a differential mobility analyzer (DMA).

2.9 Trace gases

Ozone (O_3) was measured by a dual-cell ultraviolet (UV) absorption detector (TE49C, Thermo Scientific) operating at a wavelength of $254\ \text{nm}$. Signal differences from a cell with the sample air and a parallel cell with ozone-scrubbed air are used to infer the concentration of O_3 . Sample air was drawn into the instrument through the standard HALO gas inlet via a Teflon PFA line using an external pump at a nominal flow rate of $1\ \text{L min}^{-1}$. The calibration of the instrument is traceable to the O_3 standard of the Global Atmosphere Watch station at Hohenpeißenberg, Germany. The data output of the instrument is corrected for the temperature and pressure in the absorption cells. The precision of the O_3 measurements is 2% or $1\ \text{ppb}$, whichever is larger; the accuracy is 5% . Details on the use of this instrument can be found in Huntrieser et al. (2016).

Carbon monoxide (CO) was detected with a fast-response fluorescence instrument (AL5002, Aerolaser, Garmisch, Germany) (Gerbig et al., 1999). The detection of CO is based on the excitation of CO at $150\ \text{nm}$ using a CO_2 resonance UV lamp. The fluorescence light is detected by a UV-sensitive photomultiplier. The CO detector was calibrated in-flight using onboard calibration and zero gas sources. Data are recorded at $1\ \text{Hz}$. The precision and accuracy are $3\ \text{ppb}$ and 5% , respectively.

Nitrogen monoxide (NO) and total reactive nitrogen (NO_y) were measured by a dual-channel chemiluminescence detector (CLD-SR, Eco Physics). For the NO_y channel, the chemiluminescence detector is combined with a custom-built Au converter, which reduces all oxidized reactive nitrogen species to NO (Ziereis et al., 2000). Detection of ambient NO is performed via reaction with O_3 in a chamber and the luminescence signal of the excited NO_2 produced by this reaction. Both detector channels are equipped with a pre-reaction chamber for determination of cross-reactions of O_3 with interfering species. Sampling of ambient air is conducted via a standard HALO gas inlet using a Teflon line. The precision and accuracy of the measurements depend on the ambient concentrations; typical values are 5 and 7% (NO) and 10 and 15% (NO_y), respectively.

2.10 Trajectories and air mass history analysis

Back trajectories were calculated for each flight minute, starting at the location of the HALO aircraft and using the FLEXible PARTicle dispersion model (FLEXPART) ver-

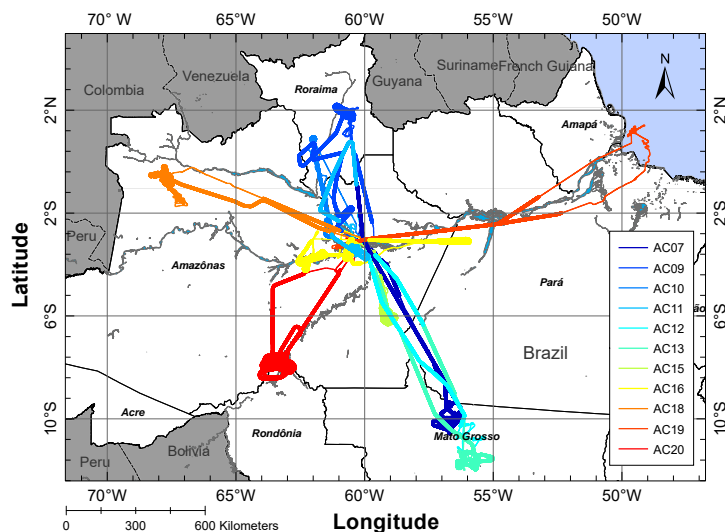


Figure 1. Tracks of the flights on which measurements at high altitude were made during ACRIDICON–CHUVA. The flight segments at altitudes > 8 km are shown as heavier lines.

sion 9.02 (Stohl et al., 1998, 2005; Stohl and Thomson, 1999; Seibert and Frank, 2004). Trajectories were driven by 6-hourly analyses, interlaced with the 3 h forecasts, from the Global Forecast System (GFS) of the National Centers for Environmental Prediction (NCEP), provided on a $0.5^\circ \times 0.5^\circ$ horizontal grid (<http://www.nco.ncep.noaa.gov/pmb/products/gfs/>, last accessed 8 September 2016). For each trajectory, 10 000 “particles” (infinitesimally small air parcels) are released and followed back in time for 10 days. Subgrid-scale processes, like convection and turbulence, act stochastically on each “particle”, resulting in a trajectory location probability distribution at each point in time. For convenience, the location probability distribution is simplified using a clustering algorithm, calculating five cluster centers of most probable trajectory locations (Stohl et al., 2002) with NCEP GDAS1 data and model vertical velocities. For simplicity, out of the five clusters, we consider only the center cluster given by FLEXPART. Therefore, all trajectories mentioned hereafter refer to the center trajectory. Additional trajectory calculations were performed using the Hybrid Single-Particle Lagrangian Integrated Trajectory (HYSPPLIT) model (Stein et al., 2015).

We examined the history of the sampled air masses for interactions with deep convection using the FLEXPART trajectories and GOES (Geostationary Operational Environmental Satellite) imagery. Every 1 min flight position was traced back in time in 1 h steps up to 120 h. Each position was then matched in time to the closest GOES-13 infrared brightness temperature (T_b). As a proxy for deep convection, we searched for cloud top T_b below -30°C and looked up the minimum T_b in a $1^\circ \times 1^\circ$ box around the center of the back-traced parcel. An example of this procedure is available in the Supplement (Figs. S1–S3). From these data, we recorded the

time difference between the moment that HALO was sampling the air mass and its encounter with deep convection, possibly including multiple contacts with deep convection. We also noted the “deepest convection” (minimum T_b) encountered by the parcels and their height at the time of the encounter, as well as the number of hours that the parcel was within boxes with deep convection ($T_b < -30^\circ\text{C}$).

3 Results and discussion

3.1 The ACRIDICON–CHUVA campaign

The ACRIDICON–CHUVA flights covered most of the Amazon Basin, reaching from the Atlantic coastal waters in the east to near the Colombian border in the west, and from the Guyanese border in the north to the arc of deforestation in the south. The flight tracks of the flights analyzed in this paper are shown in Fig. 1, where the flight segments at altitudes > 8 km are shown as heavier lines. The dates of the flights and other supporting information are given in the overview paper by Wendisch et al. (2016).

3.2 Synoptic situation and chemical context

3.2.1 Meteorological overview

During boreal summer, the Intertropical Convergence Zone (ITCZ) undergoes a seasonal northward shift towards the northernmost part of South America, so that in this season almost all of the Amazon Basin is in the meteorological Southern Hemisphere. Examination of cloud top height and precipitation images showed that during the campaign (6 September to 1 October 2014) the ITCZ was located be-

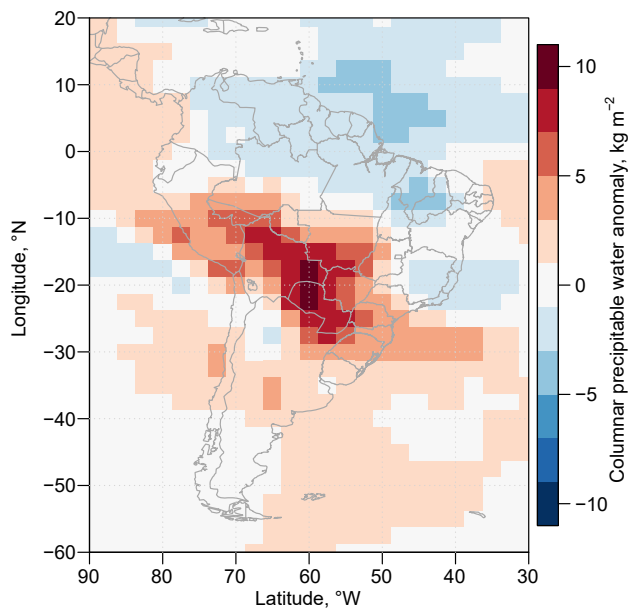


Figure 2. Columnar precipitable water anomaly for September 2014 (based on the 1981–2010 average NCEP/NCAR reanalysis).

tween about 4 and 12° N but was often not very well defined over South America (<http://www.worldview.earthdata.nasa.gov>, last accessed 13 January 2017). This seasonal shift establishes the large-scale thermodynamic conditions that define the dry season over the Amazon Basin, characterized by synoptic-scale subsidence, a relatively dry PBL and middle troposphere, and warm temperatures at the top of the PBL, resulting in elevated convective inhibition energy (CINE) (Fu et al., 1999; Wang and Fu, 2007; Collow et al., 2016). During the dry season, there is less shallow convection, cloud cover, and rainfall than in the wet season, but the convection that does occur is more organized with pronounced vertical development because of the simultaneous presence of high convective available potential energy (CAPE) and high CINE (Machado et al., 2004; Collow et al., 2016; Giangrande et al., 2017; Zhuang et al., 2017). The deep convective cloud fraction peaks in the late afternoon and evening (16:00 to 24:00 LT) with a cloud fraction maximum between 9 and 13 km altitude and a minimum near and above the freezing level between 4 and 7 km (Collow et al., 2016; Zhuang et al., 2017).

During the ACRIDICON–CHUVA campaign, the intense warm sea surface temperature (SST) anomaly that had earlier prevailed in the southern South Atlantic and a less intense cold SST anomaly in the northern South Atlantic and near the Equator were strongly reduced, and a warm SST anomaly in the equatorial Pacific was building to form the 2015 El Niño (see also Martin et al., 2016). Consequently, the pattern of wind and omega (vertical motion) field anomalies decreased to nearly normal conditions. However, during

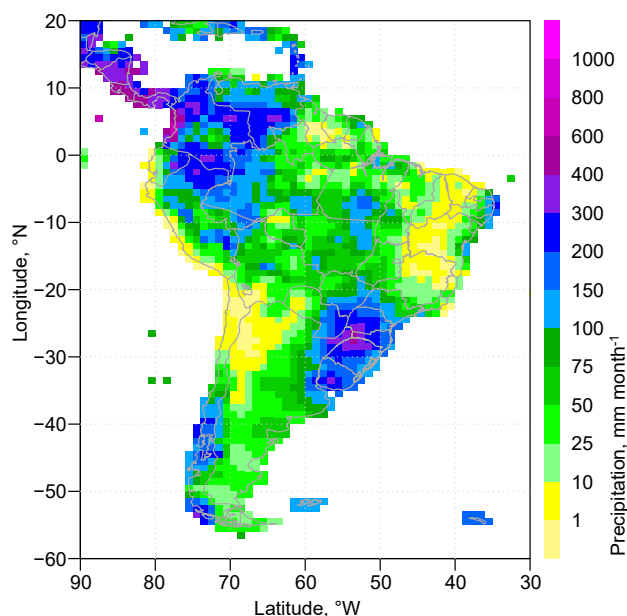


Figure 3. Total rainfall (millimeters per month, 1° resolution) for September 2014. Data are from the Global Precipitation Climatology Centre (GPCC).

the campaign, there was a clear northeast–southwest contrast with drier conditions in the northeast and wetter ones in the southwest, as seen in the columnar precipitable water anomaly data from the NCEP Climate Forecast System version 2 reanalysis (Fig. 2) (Saha et al., 2017). The majority of HALO flights were over the drier anomaly or the neutral region. As a consequence of this drier anomaly, these regions presented warmer temperatures and lower relative humidity than the normal climatology. The synoptic pattern during the campaign resulted in a spatial rainfall distribution with a meridional pattern, with more intense rainfall in the west, around 300 mm in September, and less than 100 mm in the eastern Amazon (Fig. 3). Nine cold fronts penetrated into Brazil during September; however, only two moved northward and they had little interaction with Amazon convection. Only the cold front on 20 to 23 September was able to organize convection in the south of the Amazon Basin.

Figure 4 shows the low- (850 hPa) and high-level (200 hPa) wind fields during September 2014. The mean low-level flow at 850 hPa shows the typical easterly winds throughout the Amazon Basin (Fig. 4a), decelerating near the Andes and curving to the subtropics. At high levels (Fig. 4b), there is a weak anticyclonic circulation over the southern basin, featuring the initial increased deep convection in the transition from the dry to the wet season (September) and the development of the Bolivian High during the onset of the wet season (December to March) (Virji, 1981; Zhou and Lau, 1998).

During the research flights, HALO reached maximum altitudes of 12.6 to 14.4 km a.s.l., corresponding to potential

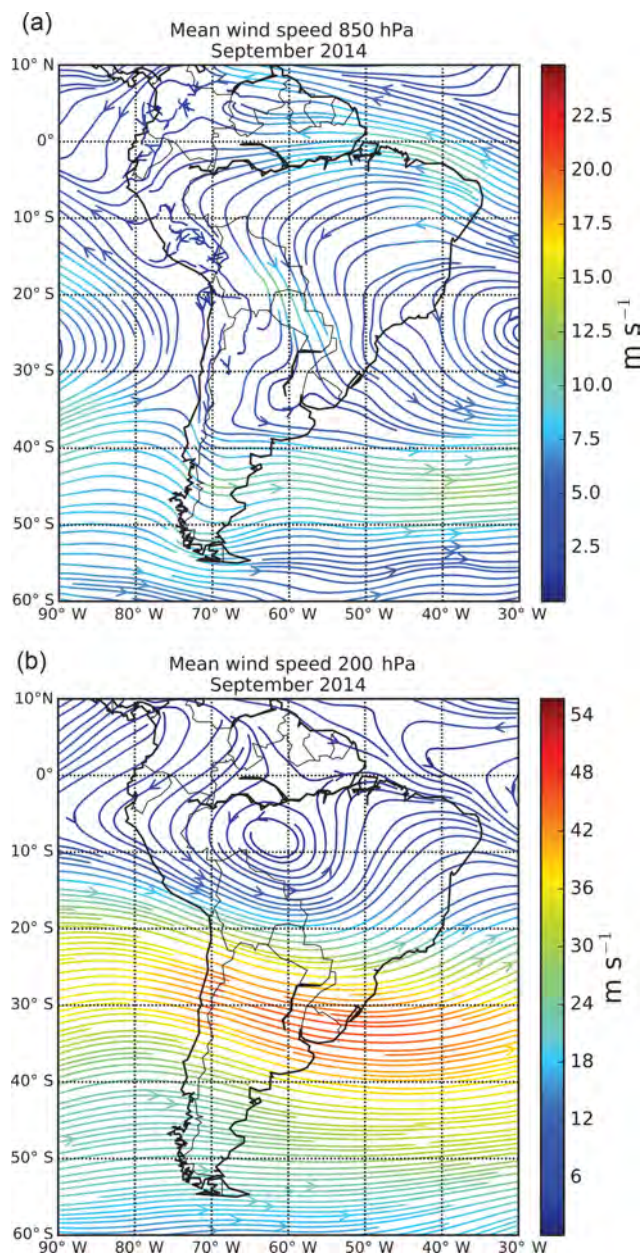


Figure 4. Mean wind speeds during September 2014 at (a) 850 hPa and (b) 200 hPa (data from NCEP/NCAR).

temperatures between 352 and 360 K (Fig. 5), i.e., the bottom of the tropical tropopause layer (TTL). The vertical profiles of temperature and potential temperature were remarkably consistent between the flights, showing a fairly stable stratification up to about 8 km and a slightly weaker gradient in potential temperature above this altitude. Relative humidity shows a broad minimum in the region between 6 and 10 km. For comparison, the data from radiosonde soundings at Manacapuru (a site southwest of Manaus) are provided in the Supplement (Fig. S4).

Based on the soundings, the mean height of the thermal tropopause during the campaign was 16.9 ± 0.6 km (unless mentioned otherwise, we use the notation “arithmetic average \pm SD (standard deviation)” to indicate mean and variance in this paper), corresponding to a potential temperature of about 380 K. During September 2014, the mean CAPE was 1536 J kg^{-1} and the mean CINE value was 37 J kg^{-1} ; the precipitable water was 42 mm, the lifting condensation level 919 hPa, and the bulk shear 4.8 m s^{-1} (difference between the mean wind speed in the first 6 km and 500 m). These values give a clear idea about the typical cloud base expected, the high instability, the need of a forcing due to the CINE, the high shear, and the amount of integrated water vapor.

In this paper, we use the following terminology to describe the different layers of the tropical atmosphere: the region from the surface to the convective cloud base (typically about 1.2 to 1.7 km during midday) is the PBL, above which is the convective cloud layer (CCL), which typically reached altitudes of about 4–5 km during our campaign. The region between the CCL and the TTL is the FT, which we subdivide into the middle troposphere (MT) between about 5 and 9 km and the UT above about 9 km.

3.2.2 Air mass origins and history

For an overview of air mass movement in the UT over the central Amazon during the campaign, we obtained trajectory frequency statistics for air masses arriving at altitudes between 7 and 14 km over the central Amazon Basin. The frequency analysis indicates that air mass movement in the upper troposphere was generally relatively slow and tended to follow anticyclonic patterns (Fig. 6), consistent with the 200 hPa streamlines shown in Fig. 4b. The frequency diagram for the 72 h trajectories initialized at 12 km altitude (Fig. 6a) shows that most air masses had remained over the basin for the preceding 3 days (only about 1 % of the endpoints fall outside of the basin) and therefore had a high probability of encountering deep convection outflow. The 10 and 14 km statistics show essentially the same patterns (Figs. S5 and S6), as do the individual trajectories calculated from the aircraft positions along the flight tracks (not shown).

The 120 h trajectory statistics (Fig. 6b) and the examination of the individual trajectories along the flight tracks indicate that the air sampled in the UT had followed a number of different general flow patterns before being sampled by HALO: (1) flow from the Pacific with an anticyclonic loop of variable extent over the basin, ranging from almost zonal west-to-east flow (type A in Table 1) to a huge loop going as far south as Argentina and as far east as the Atlantic, and then returning to the basin (type B, the southernmost trajectories in Fig. 6b); (2) flow from the Atlantic, often almost zonal (type C); (3) internal circulation within the basin, usually along anticyclonic loops but sometimes erratic (type D); and (4) flow from the Caribbean, often following an anticyclonic pattern (type E, the northernmost trajectory).

ries in Fig. 6b). These flow patterns are also evident in the streamlines shown in Fig. 4. Inflow from the Pacific is evident south of 10° S, which can merge with the dominant anticyclone centered at about 8° S, 62° W, whereas inflow from the Atlantic and Caribbean is important mostly north of the Equator. The flow pattern types of the UT air masses that were enriched in aerosol particles are given in Table 1.

3.2.3 Atmospheric chemical environment

The atmospheric chemical environment over the Amazon Basin shows a pronounced seasonal variation (Talbot et al., 1988, 1990; Andreae et al., 1990b, 2002, 2012, 2015; Artaxo et al., 2002, 2013; Martin et al., 2010). During the rainy season, regional biomass burning is at a minimum and biological sources dominate trace gas and aerosol emissions in the basin, resulting in often near-pristine conditions. The most significant pollution input during this season is long-range transport from north and west Africa, which brings in a mixture of mineral dust and emissions from biomass and fossil-fuel burning (Talbot et al., 1990; Q. Wang et al., 2016). In contrast, ACRIDICON-CHUVA took place during the dry season, when the Amazon Basin is impacted by a mixture of pollution from regional and remote sources (Andreae et al., 1988; Talbot et al., 1988; Artaxo et al., 2013; Pöhlker et al., 2017). Deforestation and pasture maintenance burning occurs throughout the basin, with the highest intensity along the southern periphery, the so-called “arc of deforestation”. This creates a steep gradient of pollutant concentrations from the relatively moist and less densely developed northern and western basins to the drier and highly deforested and developed southern basin (Andreae et al., 2012).

Long-range transport from Africa affects pollution levels over the Amazon, in addition to regional sources. In the northern part of the basin, part of the 10-day back trajectories arriving at the aircraft positions in the lower troposphere come from west Africa, where biomass burning and fossil-fuel emissions are prevalent, while other trajectories follow the northeastern coast of Brazil, which is densely populated. As one moves south, the influence of long-range transport from southern Africa becomes more prevalent. This was clearly observed during flight AC19, much of which took place over the Atlantic Ocean east of the Brazilian coast. On this flight, an extended, 300 m thick layer of pollution at 4 km altitude was identified over the Atlantic with elevated rBC concentrations up to $2 \mu\text{g m}^{-3}$ (see Sect. 3.4.4). The back trajectories from the Amazon south of the Equator very frequently end in the central and eastern tropical Atlantic (see Fig. 3 in Andreae et al., 2015), where high levels of ozone, aerosols, and other pollutants from biomass burning have been documented by in situ and satellite observations, starting in the 1980s (Watson et al., 1990; Fishman et al., 1991, 1996; Andreae et al., 1994; Browell et al., 1996).

3.3 Vertical distribution of aerosol particle number concentrations over the Amazon Basin

Figure 7a shows a statistical summary of all CN number concentrations (N_{CN}) observed during the campaign. Data affected by local pollution and cloud artifacts have been removed as discussed in Sect. 2.2. (Additional information about the flight segments on which elevated N_{CN} were encountered is provided in Table 1, and campaign average concentrations for the particle concentrations in the different size classes and altitude regions are given in Table 2.) In the PBL, which typically reached heights of 1.4 to 1.8 km during the afternoon, mean N_{CN} ranged from $\sim 750 \text{ cm}^{-3}$ on the least polluted flights to $\sim 4500 \text{ cm}^{-3}$ in the most polluted regions over the southern part of the basin. Above the PBL, CN concentrations typically remained relatively high within the CCL up to about 3–4 km and then declined with altitude. N_{CN} reached a minimum of $\sim 700 \text{ cm}^{-3}$ at about 4–5 km altitude everywhere over the basin. This aerosol minimum coincides with the minimum in cloud cover that has been observed at and above the freezing level, which has been suggested to be associated with rain development by the Wegener–Bergeron–Findeisen process at this level (Collow et al., 2016).

Above this level, we found a general increase in particle concentrations, such that above 8 km, N_{CN} were typically in the range of 2000 to $19\,000 \text{ cm}^{-3}$ (i.e., the range of quartiles above 8 km in Fig. 7a). On average, N_{CN} in the UT were almost 5 times as high as in the LT. The 8 km altitude level corresponds approximately to the 340 K potential temperature level, above which elevated CN concentrations had also been found in previous studies (Borrmann et al., 2010; Weigel et al., 2011).

While the statistical plot in Fig. 7a shows a general particle enrichment in the UT, individual vertical profiles show more complex structures (Fig. 7b). The highest N_{CN} , sometimes reaching up to $65\,000 \text{ cm}^{-3}$, were encountered in thin layers often only a few hundreds of meters thick. A typical example for such a layer is seen in the descent profile (segment A2) from flight AC09 (Fig. 4b), with peak CN concentrations of about $35\,000 \text{ cm}^{-3}$. Other profiles, e.g., the descent profile from flight AC07 (segment G), show enhancements over a layer about 3 km thick, with N_{CN} of $10\,000$ – $20\,000 \text{ cm}^{-3}$.

The CN enrichments in the UT consist predominantly of ultrafine particles in the size range below 90 nm. In contrast to N_{CN} , the enhancement of accumulation-mode particles (N_{acc} , defined here as the particles in the size range 90 to 600 nm) in the UT is much less pronounced. The concentration of accumulation-mode particles in the LT typically ranged from ~ 500 to $\sim 3000 \text{ cm}^{-3}$, depending on the level of pollution (Fig. 8a). Like the vertical profile of N_{CN} , the profile of N_{acc} also shows a decrease above the PBL to a minimum around 4–5 km, followed by an increase towards the upper troposphere. Over the more polluted regions in the southern basin, N_{acc} in the UT was often considerably lower

Table 1. Properties of the flight legs on which elevated aerosol concentrations were measured during ACRIDICON-CHUVA.

Flight Leg	Start (UTC)	End (UTC)	Altitude range (m)	N_{CN} max. (cm^{-3})	N_{CN} mean (cm^{-3})	$N_{CCN0.5}$ mean (cm^{-3})	N_{Acc} mean (cm^{-3})	Ultrafine fraction	Trajectory type	Min T_b [min, max] ^a ($^{\circ}C$)	Time since last DC [min, max] ^b (h)	Time in DC [min, max] ^c (h)	Sampling environment
AC07 A1	1622	1626	8300–9200	17200	9360	657	696	0.93	A	[–76, –65]	[0, 0]	[21, 27]	in and near outflows
AC07 AA1	1626	1627	9140	36 100	19230	775	588	0.97	A	–	–	[19, 26]	in and near outflows
AC07 A2	1627	1633	8100–9100	38 400	24250	471	499	0.98	A	[–77, –76]	[0, 0]		clear air
AC07 AA2	1633	1637	6700–8200	26 700	6450	708	565	0.91	A	–	–		clear air
AC07 B	1714	1717	7000–8400	15 900	7140	214	270	0.96	A	[–75, –68]	[0, 0]	[13, 28]	clear air
AC07 C	1923	1929	9000	22 600	16480	272	389	0.98	A	[–78, –74]	[0, 0]	[27, 40]	clear air
AC07 D1	2024	2027	8500–10 500	23 200	14270	–	146	0.99	A	[–74, –68]	[0, 0]	[29, 40]	clear air near outflow
AC07 D2	2028	2112	11 000	28 200	15 160	–	76	0.99	A	[–76, –68]	[0, 0]	[12, 28]	outflow, mixed with cirrus
AC07 E	2126	2129	13 100	33 500	15 140	–	–	–	A	[–72, –67]	[0, 0]	[21, 28]	pristine ice cirrus
AC07 F	2130	2147	13 200	25 300	12030	13	–	–	A	[–72, –69]	[0, 5]	[24, 32]	clear air
AC07 G	2205	2211	13 000–10 000	20 500	15470	284	–	–	A	[–76, –51]	[0, 0]	[24, 31]	cirrus
AC07 GG	2210	2212	10 200–9500	19 500	16 840	–	869	0.95	A				cirrus
AC08	No useful high-altitude CN data; CCN moderately elevated at about 10 and 13 km, about 1200/cc												
AC09 A1	1453	1455	11 400	24 100	10370	901	572	0.94	B	[–74, –71]	[16, 16]	[22, 41]	clear air
AC09 A2	1455	1458	11 900	27 600	12970	1103	808	0.94	B	[–76, –72]	[16, 17]	[34, 41]	clear air
AC09 A3	1501	1503	11 000	35 100	14470	629	697	0.95	B	[–72, –70]	[17, 17]	[38, 40]	clear air
AC09 B1	1815	1820	11 000	19 100	10540	1393	954	0.91	B	[–76, –74]	[14, 14]	[49, 54]	around Cb anvil
AC09 B2	1821	1827	11 300–11 600	28 300	15370	1414	1012	0.93	B	[–78, –73]	[14, 14]	[47, 57]	around Cb anvil
AC09 C	1830	1838	11 600	31 700	9130	1490	1127	0.88	B	[–79, –76]	[1, 19]	[45, 56]	clear air
AC09 D	1838	1923	11 300–11 900	13 000	5690	1012	869	0.85	B, C	[–80, –74]	[1, 1]	[34, 57]	outflow region
AC09 E	1929	1957	11 300	24 200	12790	891	856	0.93	B, C	[–76, –70]	[2, 21]	[24, 48]	outflow region
AC10 A	1709	1714	6700–8600	27 400	13040	355	389	0.94	C	[–66, –54]	[6, 7]	[19, 32]	clear air
AC10 B	1721	1728	9200	32 500	12480	850	861	0.91	D	[–78, –72]	[4, 10]	[34, 56]	clear air
AC10 C	1800	1808	9200	26 000	13 100	1020	937	0.91	B	[–79, –71]	[7, 10]	[33, 56]	clear air
AC10 D	1811	1815	9200–10 100	33 000	20180	1130	684	0.95	B	[–84, –72]	[5, 5]	[23, 51]	clear air
AC10 E	1817	1833	10 800–13 600	33 400	22210	712	289	0.98	E		[0, 12]	[42, 76]	thin cirrus
AC10 F	1835	1906	13 800	34 700	16540	464	–	–	E	[–80, –68]	[0, 0]	[33, 54]	cirrus layer
AC10 G	1912	1919	10 600–7500	24 200	10220	1230	1160	0.83	B	[–80, –58]	[0, 14]	[11, 60]	clear air
AC11 A	1603	1605	8700–9700	47 400	26280	572	323	0.98	E	[–54, –32]	[3, 44]	[1, 18]	clear air
AC11 B	1613	1630	11 800	4700	3850	1390	763	0.80	E, D	[–76, –58]	[0, 6]	[14, 41]	clear air
AC11 C	1633	1642	11 800–10 800	31 700	6080	1436	937	0.78	D	[–80, –77]	[0, 0]	[30, 46]	around anvil
AC11 D	1831	1850	5200–6700	25 000	14380	–	187	0.98	C	[–79, –79]	[0, 0]	[18, 19]	outflow region
AC11 E	1907	1930	9900–12 200	36 100	29280	–	330	0.99	D	[–85, –74]	[0, 0]	[26, 82]	outflow region
AC11 F1	1940	1942	12 200	54 900	22060	–	674	0.95	E, D	[–84, –84]	[0, 0]	[55, 55]	outflow region
AC11 F2	1942	1951	12 200	32 800	20720	–	549	0.97	E, D	[–84, –84]	[0, 0]	[55, 55]	outflow region
AC11 G	2005	2030	13 700–14 200	2830	10990	–	–	–	D	[–84, –84]	[0, 0]	[55, 55]	outflow region
AC11 H	2042	2057	12 200–10 400	47 900	20240	–	663	0.96	A	[–84, –84]	[0, 0]	[55, 55]	outflow region
AC12 A	1512	1518	9800–11 300	19 300	8040	1130	341	0.95	E	[–79, –74]	[0, 0]	[23, 37]	clear
AC12 B	1524	1527	11 300	24 700	9290	1120	358	0.95	A	[–83, –71]	[0, 0]	[26, 66]	thin outflow
AC12 C	1537	1541	7300–5600	26200	7760	356	186	0.95	B	[–78, –57]	[1, 1]	[7, 16]	clear
AC12 D	1922	1925	8000–9700	17 400	11 980	650	132	0.99	B	[–71, –71]	[17, 20]	[6, 12]	clear
AC12 E	1928	1933	10 800–12 200	25 300	15 740	423	75	0.99	B	[–70, –57]	[20, 24]	[8, 18]	clear
AC12 F1	1936	1950	12 200–13 100	7020	5940	2010	698	0.88	B, D	[–80, –67]	[0, 38]	[12, 40]	clear
AC12 F2	1952	2015	13 100	7300	5950	1190	594	0.90	B, D	[–82, –74]	[0, 21]	[28, 77]	aged outflow
AC12 G	2017	2020	13 200–12 800	19 600	10930	661	422	0.96	E	[–79, –75]	[0, 0]	[26, 49]	outflow
AC12 H	2023	2027	11 300–9600	23 900	16930	849	372	0.98	C	[–80, –77]	[0, 0]	[37, 59]	mostly clear air

Table 1. Continued.

Flight	Leg	Start (UTC)	End (UTC)	Altitude range (m)	N_{CN} max. (cm ⁻³)	N_{CN} mean (cm ⁻³)	$N_{CCN0.5}$ mean (cm ⁻³)	N_{acc} mean (cm ⁻³)	Ultrafine fraction	Trajectory type	Min T_b [min, max] ^a (°C)	Time since last DC [min, max] ^b (h)	Time in DC [min, max] ^c (h)	Sampling environment
AC13	A	1520	1533	11 000–11 900	43 500	13 830	1054	–	–	C	[-78, -75]	[0, 12]	[27, 43]	mostly cirrus and old outflow
AC13	B	1550	1607	11 900–6900	36 300	11 890	1012	476	0.95	A	[-83, -50]	[1, 8]	[11, 47]	mostly cirrus and old outflow
AC13	C	1901	1908	9500	25 700	17 870	687	–	–	A	[-72, -66]	[0, 0]	[13, 24]	clear air around anvils
AC13	D1	1909	1912	10 700	26 200	18 600	910	–	–	A	[-70, -66]	[0, 0]	[15, 19]	“
AC13	D2	1916	1919	10 700	28 200	19 170	1017	–	–	A	[-73, -69]	[0, 0]	[24, 25]	“
AC13	D3	1921	1926	10 700	29 500	19 010	919	–	–	A	[-69, -68]	[0, 0]	[15, 26]	“
AC13	D4	1930	1933	10 700	21 600	10 900	727	–	–	A	[-68, -67]	[0, 0]	[14, 17]	“
AC13	E	1939	1942	11 900	22 500	15 100	770	–	–	A	[-57, -47]	[10, 10]	[5, 8]	“
AC13	F	2036	2043	12 200	18 600	7840	912	–	–	A	[-78, -76]	[0, 0]	[34, 43]	clear air, some cirrus
AC14								No useful high-altitude data						
AC15	A	1415	1419	10 500–11 700	58 500	38 170	687	453	0.98	D	[-81, -78]	[0, 9]	[63, 68]	air around a huge Cb anvil
AC15	B	1419	1424	11 800–12 900	67 900	46 970	701	405	0.98	D	[-81, -81]	[0, 0]	[59, 66]	mostly cirrus and old outflow
AC15	C	1431	1432	13 200	49 500	20 900	1070	747	0.94	D	[-84, -84]	[0, 0]	[55, 55]	“
AC15	D	1436	1437	13 200	38 300	15 300	1009	633	0.92	D	[-84, -77]	[0, 0]	[50, 56]	“
AC15	E	1448	1449	12 500	44 500	29 220	603	718	0.97	D	[-81, -79]	[0, 0]	[54, 59]	“
AC15	F	1452	1455	12 500	60 500	45 100	672	514	0.97	D	[-79, -75]	[0, 0]	[52, 56]	“
AC15	G	1456	1500	12 500–11 900	59 200	38 070	748	574	0.98	D	[-82, -72]	[0, 0]	[53, 62]	“
AC15	H	1502	1505	11 900–11 600	49 800	16 440	1114	750	0.94	D	[-76, -73]	[0, 0]	[62, 69]	“
AC15	I	1518	1519	11 300	46 800	22 000	1848	931	0.93	D	[-79, -73]	[0, 0]	[65, 71]	“
AC15	J	1526	1528	10 700	21 700	8980	1292	817	0.86	D	[-76, -75]	[0, 0]	[59, 65]	“
AC16	A	1554	1600	10 700–12 200	40 300	21 210	606	223	0.98	B	[-75, -68]	[0, 0]	[9, 18]	clear air
AC16	B	1749	1757	10 000–10 300	28 200	11 350	926	282	0.97	B	[-68, -57]	[0, 0]	[8, 10]	air around a large Cb anvil
AC16	C	1803	1815	10 300–10 700	27 200	15 180	749	208	0.98	B	[-75, -60]	[0, 0]	[9, 12]	air around a large Cb anvil
AC16	D	1818	1820	10 700–11 300	23 100	11 540	789	356	0.97	B	[-75, -67]	[0, 0]	[10, 17]	air around a large Cb anvil
AC16	E	1824	1826	12 000	26 700	14 070	488	354	0.97	B	[-73, -75]	[0, 0]	[17, 19]	air around a large Cb anvil
AC16	F	1857	1911	12 600–11 900	19 500	11 210	598	521	0.94	B	[-73, -66]	[0, 0]	[22, 28]	air around a large Cb anvil
AC16	G	1925	1935	11 900	22 700	12 880	703	492	0.95	B	[-73, -70]	[0, 0]	[22, 30]	air around a large Cb anvil
AC16	H	1950	2000	11 900–9600	27 100	12 670	806	444	0.96	B	[-75, -65]	[0, 0]	[13, 29]	air around a large Cb anvil
AC17								No high-altitude data						
AC18	A1	1454	1456	8300–8600	20 700	10 698	–	219	0.98	B	[-60, -10]	[14, 17]	[2, 5]	clear air
AC18	A2	1520	1522	12 900–8400	22 500	14 538	479	400	0.97	C	[-58, -38]	[14, 18]	[1, 5]	clear air
AC18	B	1753	1801	7100	10 040	6255	400	312	0.95	C	[-30, -0]	[0, 0]	[1, 2]	clear air around anvils
AC18	C	1833	1834	7100–7400	14 200	10 713	404	280	0.97	C	[-52, -28]	[22, 22]	[1, 1]	clear air around anvils
AC18	D	1913	2005	11 300–12 000	4000	2367	916	640	0.73	A, D	[-75, -37]	[0, 16]	[3, 46]	clear air around anvils
AC18	E1	2017	2034	13 000–13 700	81 700	4841	1481	892	0.82	A, D	[-84, -68]	[0, 44]	[21, 45]	clear air
AC18	E2	2040	2043	13 700–13 200	44 700	13 679	469	283	0.98	D	[-77, -71]	[0, 0]	[28, 42]	clear air downwind of large Cb
AC18	F	2053	2057	9500–8100	15 800	8778	444	318	0.96	C, D	[-88, -32]	[1, 20]	[11, 11]	clear air
AC19	A1	1518	1519	7300–7700	30 600	28 480	451	339	0.99	B	[-82, -65]	[14, 43]	[7, 14]	clear air
AC19	A2	1536	1601	12 600	3600	2910	679	268	0.91	E	[-72, -58]	[43, 94]	[6, 19]	clear air, high alt leg
AC19	E1	2009	2010	8500–8900	14 700	11 470	642	271	0.98	B	[-75, -59]	[16, 92]	[8, 16]	clear air
AC19	E2	2023	2100	13 800	3900	2690	1024	498	0.81	A	[-76, -29]	[0, 105]	[1, 22]	clear air
AC19	E3	2106	2119	13 800	10 200	2770	1073	950	0.65	B	[-73, -57]	[0, 1]	[6, 25]	outflow
AC19	E4	2127	2128	7500–6600	66 000	16 210	440	616	0.96	D	[-60, -59]	[3, 22]	[4, 7]	clear air
AC20	A	1654	1658	11 700–12 500	30 300	21 540	881	616	0.97	A, D	[-77, -53]	[1, 1]	[7, 28]	NPF at top of smoke layer
AC20	B	1901	1905	12 300	21 300	9340	614	381	0.95	A, D	[-78, -70]	[0, 0]	[14, 42]	NPF at top of smoke layer

^a Minimum and maximum temperatures at top of most recent deep convection in grid boxes through which the trajectories for the flight leg had passed. ^b Trajectories were calculated for each minute of the leg, and for each trajectory the time between sampling and the most recent encounter with DC was determined. Given are the shortest and the longest of these time intervals. ^c Minimum and maximum lengths of time that the trajectories from each leg had spent in grid boxes with DC.

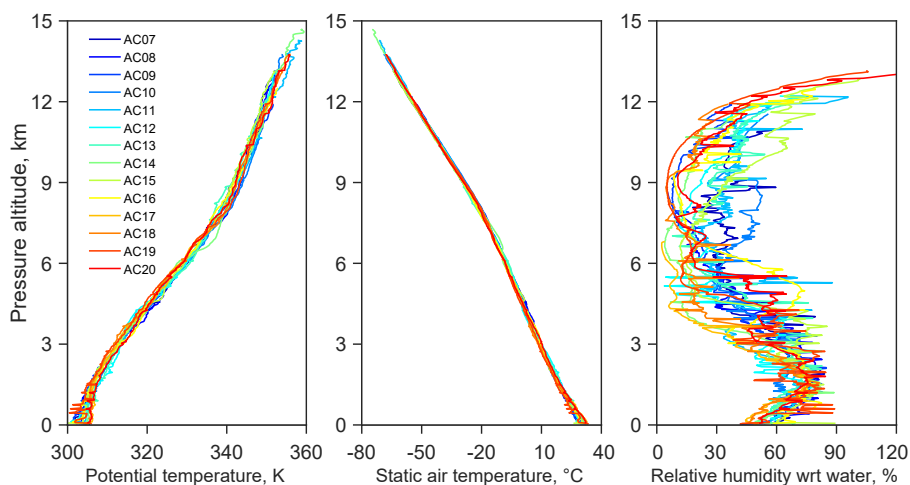


Figure 5. Vertical profiles of potential temperature, static air temperature, and relative humidity measured on HALO during the ACRIDICON-CHUVA flights over the Amazon Basin.

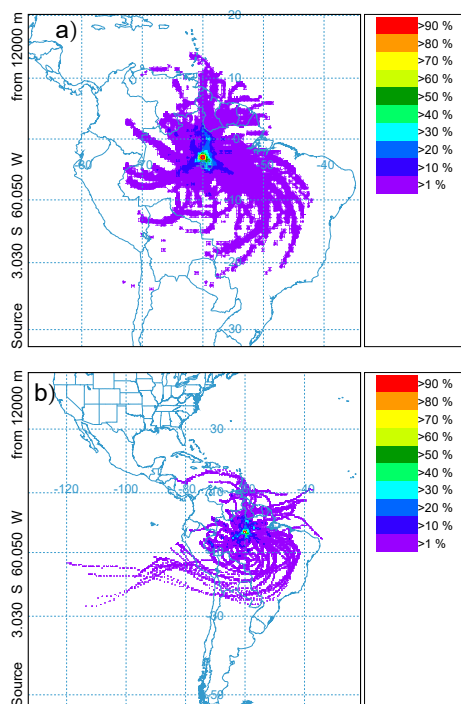


Figure 6. Trajectory statistics based on (a) 72 h and (b) 120 h back trajectory calculations for September 2014, initialized at Manaus at an elevation of 12 km.

than in the LT. On average, N_{acc} in the UT was only about half the concentration measured in the LT.

Figure 8b illustrates the different behavior of CN and accumulation-mode particle number concentrations at the

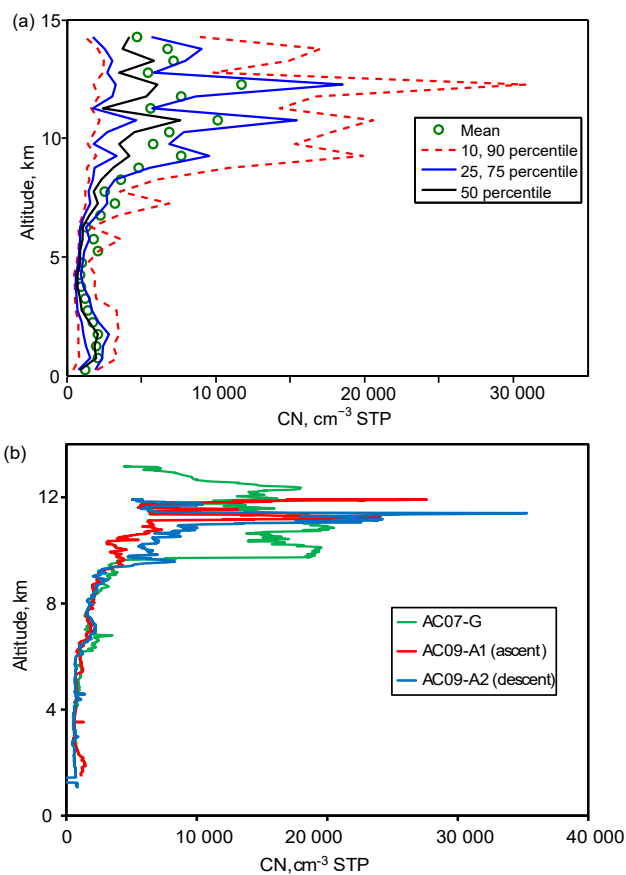


Figure 7. Vertical profiles of CN concentrations, N_{CN} : (a) overall statistics from all flights, (b) examples from individual profiles on flight AC07 (segment G) and AC09 (segments A1 and A2).

example of a sounding in the central Amazon Basin from flight AC19. In the LT, N_{CN} and N_{acc} have similar values

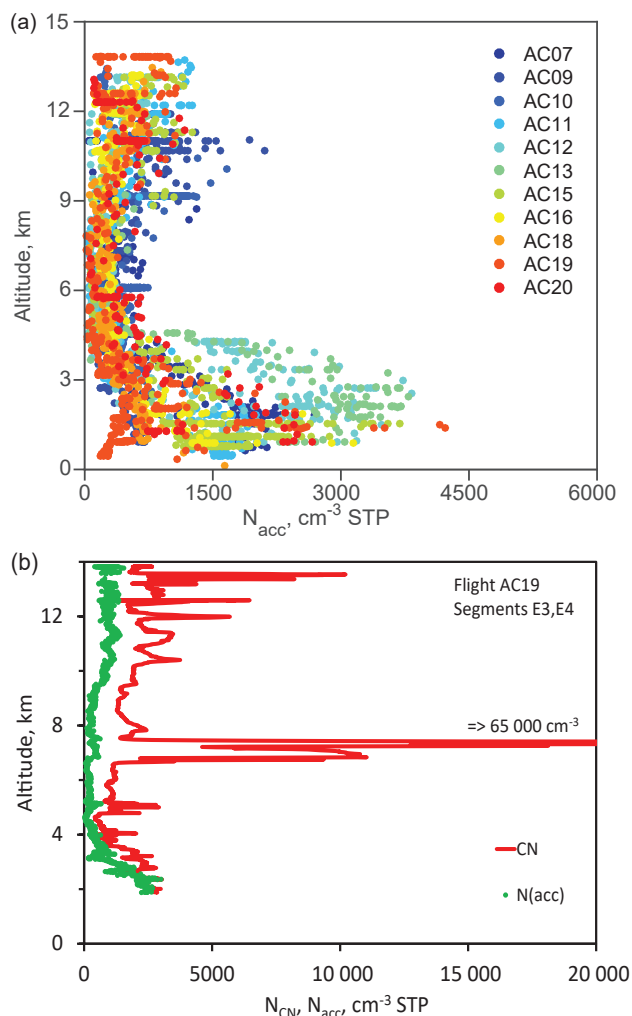


Figure 8. Vertical profiles of accumulation-mode particle concentrations, N_{acc} ; (a) 1 min averaged data from all flights, (b) N_{acc} profile from flight AC19 together with the profile of N_{CN} from the same flight (1 s data).

and decline to a minimum at about 4.7 km. Above this altitude, N_{CN} shows several sharp concentration peaks, with one at about 7.4 km reaching concentrations around 65 000 cm^{-3} . These peaks are only weakly, if at all, reflected in N_{acc} , which shows a broad enhancement in the UT to values around 1000 cm^{-3} . Consequently, we find two types of aerosol enrichments in the UT: at one extreme, thin layers with extremely high N_{CN} values but no significant increase in particles larger than 90 nm; at the other, broad overall particle enrichments with modest values of both N_{CN} and N_{acc} .

3.4 Differences between UT and LT aerosols

The high concentrations of particles in the UT over the Amazon Basin beg the question of their origin. Three different mechanisms can be considered: vertical transport of particles from the PBL by deep convection, horizontal long-range

transport from remote source regions, and in situ new particle formation in the outflow from deep convection. To assess these possibilities, we discuss in the following sections the chemical and physical properties of the UT aerosols and contrast them with the LT aerosol. In Sect. 3.4, we will compare the physical and chemical properties of the aerosols in the LT and UT to examine the role that vertical transport may have played as a source for the UT aerosol enrichments. Long-range transport and new particle formation in the UT will be discussed in Sect. 3.5.

A first argument against vertical transport as the dominant source mechanism for the large particle concentrations in the UT comes simply from the observed CN concentrations. Since we are using concentrations normalized to standard temperature and pressure, N_{CN} should not change with vertical transport alone, and the values measured in the UT should not exceed those measured in the PBL. The fact that CN concentrations in the UT across the entire Amazon Basin are higher than the PBL values we measured anywhere in the basin, often by very large factors, rules out vertical transport of particles from the Amazon PBL as the dominant source of UT particles.

3.4.1 Particle size

The particles in the UT have a very different size distribution from those in the LT, which confirms that they could not have originated from upward transport of PBL aerosols by deep convection. Unfortunately, a detailed analysis of the size distribution of the particles in the UT is hampered by the significant losses of small particles in our inlet system. As discussed in Sect. 2.2, the particle losses increase with altitude such that in the UT most of the particles below about 20 nm are lost in the inlet system before reaching the CPC. Because of a longer inlet tubing connection and lower sample flow, the losses were even more significant for the DMPS, and as a result of this and other operational limitations, valid particle size distributions are only available from the LT.

The DMPS measurements in the LT showed that the aerosol size distribution was dominated by an accumulation mode centered at about 190 nm, flanked by an Aitken mode with a maximum at about 80 nm (Fig. 9), in good agreement with the size distributions measured previously at ground level in the Amazon (Zhou et al., 2002; Rissler et al., 2006; Andreae et al., 2015; Pöhlker et al., 2016) and those obtained over the Amazon on the G1 aircraft during the GoAmazon 2014 campaign (Martin et al., 2016; J. Wang et al., 2016). For comparison, we show size spectra from GoAmazon 2014 from J. Wang et al. (2016), the only published size spectra from the FT over central Amazonia. Unfortunately, these data reach only up to 5.8 km, the ceiling altitude of the G1 aircraft. In the PBL, the spectra were similar to our measurements from the LT. With increasing altitude, total particle concentrations increased and the size spectrum became dominated by an Aitken mode at about 50 nm (J. Wang et al.,

Table 2. Composition of UT aerosols based on AMS and SP2 measurements (means and standard deviations).

Flight	Time (UTC)	N_{GN} (cm^{-3})	$N_{CCN0.5}$ (cm^{-3})	N_{acc} (cm^{-3})	OA ($\mu g m^{-3}$)	NO_3 ($\mu g m^{-3}$)	SO_4 ($\mu g m^{-3}$)	NH_4 ($\mu g m^{-3}$)	rBC ($\mu g m^{-3}$)	OA / SO_4	NO_3 / SO_4	Ultrafine fraction	CO (ppb)
AC07													
< 4 km	–	1620 ± 680	1070 ± 410	1363 ± 651	1.81 ± 0.96	0.088 ± 0.039	0.30 ± 0.10	0.20 ± 0.17	0.40 ± 0.21	6.1 ± 4.4	0.30 ± 0.22	0.19 ± 0.16	–
> 7 km	–	9300 ± 7420	300 ± 210	278 ± 232	0.61 ± 0.50	0.072 ± 0.051	0.071 ± 0.060	< 0.05	0.003 ± 0.007	8.5 ± 10.2	1.0 ± 1.1	0.92 ± 0.008	–
AA1	16:24–16:29	19 200	650	588	1.55 ± 0.27	0.14 ± 0.03	< 0.005	–	0.002	> 300	> 28	0.97	–
AA2	16:33–16:37	6450	710	565	1.26 ± 0.22	0.12 ± 0.02	0.020 ± 0.021	–	0.002	63	6.0	0.89	–
GG	22:09–22:11	16800	–	921	2.40 ± 1.09	0.20 ± 0.08	< 0.005	–	0.002	> 480	> 40	–	–
AC09													
< 5 km	–	920 ± 490	290 ± 95	395 ± 189	0.28 ± 0.22	0.013 ± 0.020	0.15 ± 0.07	0.03 ± 0.07	0.085 ± 0.095	1.8 ± 1.7	0.08 ± 0.14	0.51 ± 0.26	–
> 9 km	–	8020 ± 5180	1090 ± 430	861 ± 338	1.80 ± 0.52	0.22 ± 0.08	0.14 ± 0.06	< 0.05	0.001 ± 0.003	13.3 ± 6.7	1.6 ± 0.9	0.86 ± 0.07	–
AA	14:48–15:08	2280	1050	754	1.55 ± 0.53	0.21 ± 0.09	0.083 ± 0.044	< 0.05	0.001	18.6	2.5	0.54	–
BB	18:18–19:23	8060	1200	922	1.88 ± 0.47	0.23 ± 0.07	0.15 ± 0.04	< 0.05	0.001	12.6	1.5	0.85	–
EE	19:28–19:58	12 000	950	892	1.96 ± 0.47	0.23 ± 0.07	0.13 ± 0.03	< 0.05	0.001	15.4	1.8	0.92	–
A1 + A2	14:53–14:58	12 100	1040	724	1.69 ± 0.38	0.23 ± 0.06	0.08 ± 0.04	< 0.05	< 0.001	21.8	3.1	0.91	–
AC18													
< 5 km	–	740 ± 220	350 ± 100	473 ± 212	1.11 ± 1.17	0.060 ± 0.056	0.55 ± 0.27	0.19 ± 0.10	0.15 ± 0.15	2.8 ± 1.4	0.11 ± 0.08	0.51 ± 0.26	–
> 10 km	–	2950 ± 2640	920 ± 310	560 ± 145	2.07 ± 0.63	0.24 ± 0.10	0.23 ± 0.06	< 0.05	0.002 ± 0.005	9.1 ± 3.9	1.1 ± 0.5	0.86 ± 0.07	–
AA	15:06–15:16	(1740)	870	545	1.64 ± 0.20	0.20 ± 0.02	0.19 ± 0.05	< 0.05	0.001	8.5	1.0	1.50	–
DD	19:21–20:05	2360	910	639	2.04 ± 0.23	0.22 ± 0.04	0.22 ± 0.06	< 0.05	0.002	9.3	1.0	0.61	–
A1	14:54–14:56	87 000	–	203	0.43 ± 0.17	0.06 ± 0.03	0.18 ± 0.08	< 0.05	0.002	2.4	0.31	–	–
A2	15:20–15:22	17 400	500	433	0.68 ± 0.39	0.06 ± 0.05	0.14 ± 0.04	< 0.05	0.002	5.0	0.43	0.97	–
E2	20:40–20:43	15 900	360	–	1.21 ± 0.56	0.13 ± 0.09	0.22 ± 0.08	< 0.05	–	5.5	0.61	0.98	–
F	20:54–20:56	11 600	460	361	1.02 ± 0.26	0.09 ± 0.04	0.24 ± 0.07	< 0.05	0.002	4.3	0.40	0.96	–
All flights													
PBL	0–4 km	1650 ± 1030	880 ± 630	1260 ± 910	2.77 ± 2.48	0.114 ± 0.140	0.50 ± 0.31	0.43 ± 0.59	0.25 ± 0.21	5.6 ± 6.6	0.23 ± 0.43	0.28 ± 0.19	157 ± 64
MT	5–8 km	2130 ± 3070	410 ± 150	280 ± 170	0.51 ± 0.40	0.035 ± 0.039	0.17 ± 0.30	0.06 ± 0.10	0.005 ± 0.011	3.0 ± 3.6	0.21 ± 0.38	0.79 ± 0.15	96 ± 22
UT	9–15 km	7700 ± 7970	840 ± 440	568 ± 313	1.59 ± 0.91	0.190 ± 0.117	0.115 ± 0.084	0.04 ± 0.09	0.002 ± 0.006	13.8 ± 4.6	1.7 ± 1.2	0.86 ± 0.11	116 ± 39

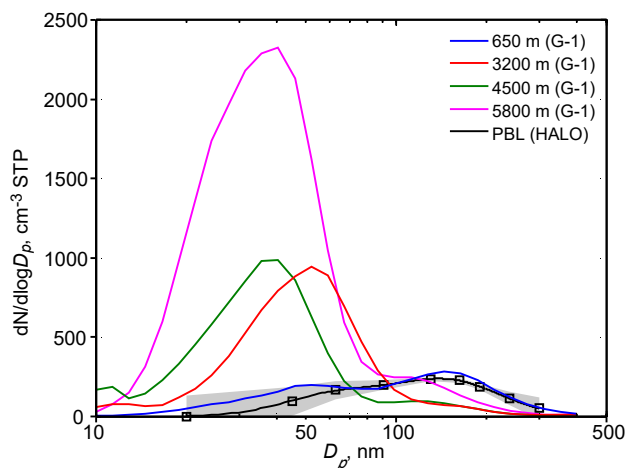


Figure 9. Size spectra: the black line shows the mean boundary layer DMPS size spectrum from a segment in the PBL on flight AC13 (16:55 to 17:18 UTC). The square black symbols represent the mean; the grey shaded area the standard deviation of the measurements. The line is a logarithmic fit with modal diameters of 74 and 175 nm. The colored lines represent size distributions from 0.65 to 5.8 km from a G1 flight during GoAmazon (J. Wang et al., 2016).

2016). A previous study over the northern Amazon in Suriname had also found a decrease in the modal diameter of the Aitken mode from ~ 70 nm in the LT to ~ 30 nm in the UT above 10 km (Krejci et al., 2003). Assuming that similar size distributions prevailed in the UT during ACRIDICON-CHUVA, and given the fact that inlet losses limited our measurements to particle diameters > 20 – 30 nm, it seems justified to conclude that our N_{CN} concentrations in the UT are actually lower limits and that the true concentrations might have been significantly higher.

In the absence of full size spectra, we use the ultrafine fraction (UFF, defined as the fraction of particles with diameters between 90 nm – the lower cutoff of the UHSAS – and ~ 20 nm – the lower cutoff of the CPC), i.e., $UFF = (N_{CN} - N_{acc})/N_{CN}$ as a metric for the contribution of the Aitken and nucleation modes to the total observed particle concentration. The summary profile plot (Fig. 10a) shows the dramatic difference between the UFF in the LT and UT: in the LT, the mean UFF is about 0.2 ± 0.1 , showing the dominance of the accumulation mode. The share of ultrafine particles increases throughout the middle troposphere, and in the UT they account for the vast majority of particles, with UFF values around 0.7 in regions where both N_{acc} and N_{CN} are moderately enriched, and values approaching 1.0 in the layers with very high N_{CN} . This shows up even more clearly in individual profiles, e.g., the soundings from flight AC18 shown in Fig. 10b. The highly enriched layers are represented by UFF peaks in the range of 0.7 to 1.0, whereas the background UT enrichment exhibits UFF values of 0.5 to 0.8. The highest UFF values were measured in the very young

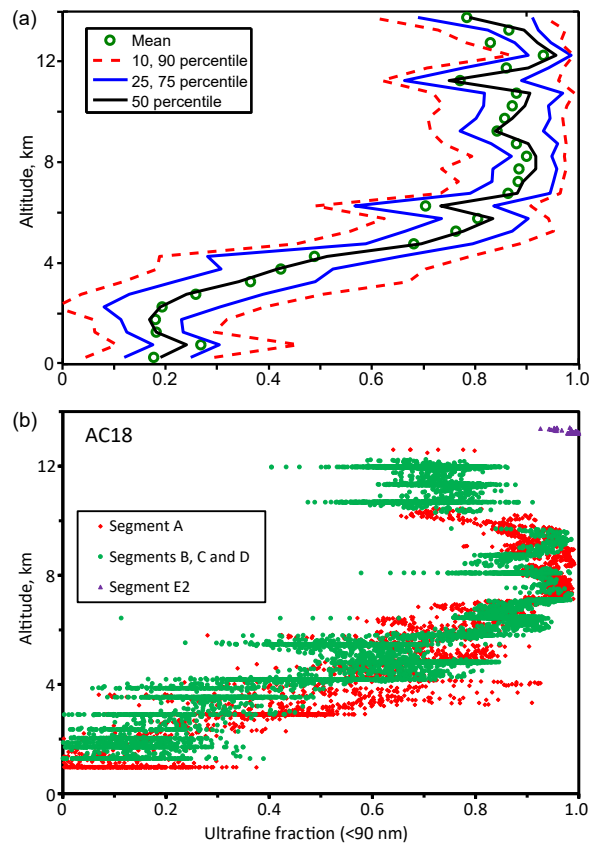


Figure 10. Vertical profiles of the ultrafine fraction (UFF); (a) overall statistics from all flights, (b) examples from individual profiles on flight AC18.

aerosol layer in segment E2 at 13.5 km (Fig. 10b), which had an estimated particle age of about 1–5 h (more on this layer in Sect. 3.5.2).

3.4.2 Cloud nucleating properties

The cloud nucleating ability of aerosol particles depends both on their size and their chemical composition. Here, we focus on CCN concentrations at 0.52 % supersaturation ($N_{CCN0.5}$), which are dominated by the particles in the accumulation-mode size range but also include a fraction of the Aitken mode. A full discussion of the CCN measurements during ACRIDICON-CHUVA will be presented elsewhere.

Figure 11a shows the vertical distribution of CCN for the entire campaign, indicating strong variability in the LT, a minimum at about 5 km, and elevated concentrations in the UT. The $N_{CCN0.5}$ variability in the LT is related to the variable levels of regional pollution, mostly from biomass burning, which were much higher in the southern part of the basin than in the north. In contrast, there was no systematic difference between the CCN concentrations in the UT above polluted and relatively clean regions. Therefore, depending on

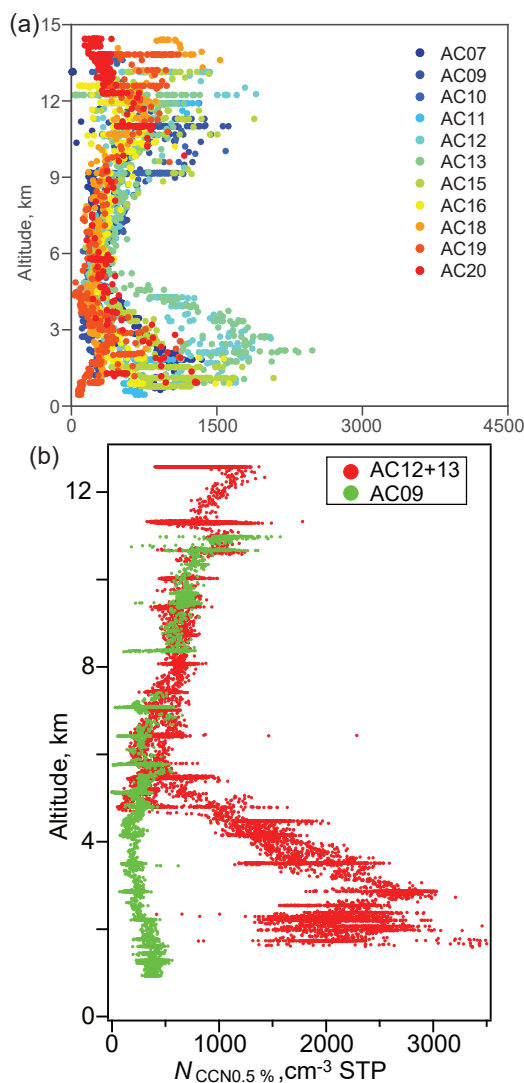


Figure 11. Vertical profiles of CCN concentrations at 0.52 % supersaturation; (a) overall statistics from all flights (1 min averages), (b) examples from individual profiles on flights AC09 (green) and AC12 + 13 (red). Flights AC12 and AC13 were conducted over the same region on successive days.

the level of pollution in the lower troposphere, the $N_{CCN0.5}$ in the UT during our campaign were higher or lower than those in the LT. This is illustrated in the example of the $N_{CCN0.5}$ profiles from a clean region (AC09) and from one polluted by biomass burning emissions (AC12 + 13), respectively (Fig. 11b). While there was a large difference in the CCN concentrations in the LT, the values in the UT were very similar between these flights, indicating that the CCN enrichments in the UT are independent of the pollution levels in the LT.

The $N_{CCN0.5}$ in the UT were consistently greater than the corresponding accumulation particle number concentrations, N_{acc} , resulting in a median $N_{CCN0.5}/N_{acc}$ ratio of 1.66

(quartile range: 1.32–2.32, $N = 53\,382$) above 8 km. This implies that some of the particles smaller than 90 nm are also able to nucleate cloud droplets at $S = 0.52\%$. Because size-selective CCN measurements were not performed during ACRIDICON–CHUVA, it was not possible to derive the actual critical diameters and hygroscopicity factors (κ ; Petters and Kreidenweis, 2007) for the CCN on this campaign. However, a consistency check can be made using the measured chemical composition. As will be discussed in detail in Sect. 3.4.4, the UT particles consist predominantly of organic material, with minor amounts of nitrate and very small fractions of sulfate. The hygroscopicity of particles consisting completely of organic matter can vary greatly, with κ between 0 and about 0.3 (Engelhart et al., 2008, 2011; Jimenez et al., 2009). Our AMS measurements (see Sect. 3.4.4) showed that the UT secondary organic aerosol (SOA) contains a substantial fraction of organics derived from the oxidation of isoprene (IEPOX-SOA) (Schulz et al., 2018), which has relatively high hygroscopicity ($\kappa \geq 0.12$) (Engelhart et al., 2011; Thalman et al., 2017). Assuming a conservative value of $\kappa_{org} \cong 0.1$, which had been found previously for the Amazon PBL (Gunthe et al., 2009; Pöhlker et al., 2016), pure SOA particles would have to have diameters of ≥ 80 nm to act as CCN at 0.52 % supersaturation, whereas for pure ammonium sulfate particles ($\kappa \cong 0.6$), the critical diameter would be about 45 nm (Petters and Kreidenweis, 2007). At a typical organic mass fraction of 0.8 for the UT aerosol (see Sect. 3.4.4), an effective κ of about 0.2, corresponding to a critical diameter of ~ 65 nm, is likely. Given the expected steep increase in particle concentration between the N_{acc} cut-off of 90 nm and the estimated critical diameter of 65 nm, a $N_{CCN0.5}/N_{acc}$ ratio of the observed magnitude appears thus quite reasonable.

The vertical distribution of the CCN fraction, i.e., the ratio $N_{CCN0.5}/N_{CN}$, shows a pronounced decrease with altitude (Fig. 12a), reflecting the smaller particle size in the UT. It also exhibits a strong inverse relation to the total particle concentration, N_{CN} . This is illustrated in the example of flight AC18 (Fig. 12b), where data from the different flight segments are plotted. Segments A and F (yellow and orange) are from soundings in the somewhat more polluted central part of the Amazon Basin, whereas B and C (green) are from the cleaner westernmost part and show the lowest CCN concentrations and the highest CCN fractions. Both soundings have high-CN layers at altitudes between 7 and 13 km, with N_{CN} up to almost $23\,000\text{ cm}^{-3}$, and correspondingly low $N_{CCN0.5}/N_{CN}$. Segment E2 (red) is from a layer that was intercepted downwind of a massive convective complex, with a transport time of only 1–5 h between the anvil and the aircraft (see Sect. 3.5.2). This layer had N_{CN} values up to $45\,000\text{ cm}^{-3}$, CCN fractions down to 0.01, and $UFF \cong 0.98$, suggesting that these recently formed particles were too small to act as CCN. This layer was embedded in a region of moderately elevated CN (segment E1 at 13–14 km; lilac), which had much higher $N_{CCN0.5}/N_{CN}$ (0.2–

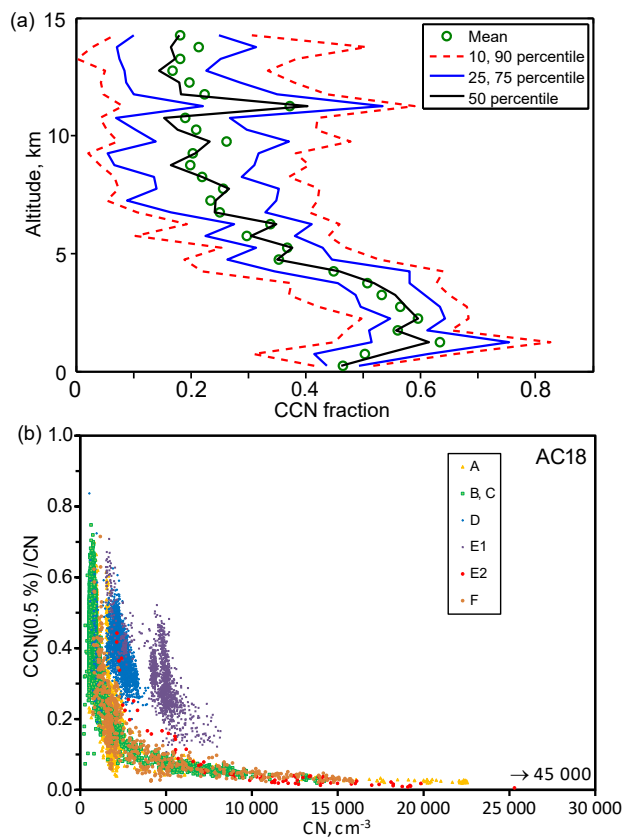


Figure 12. (a) CCN fraction ($N_{CCN0.5}/N_{CN}$) vs. altitude (all data). The peak at 11 km is caused by the inclusion of a large number of measurements from flight AC20 on a horizontal leg at 11 km, which was influenced by biomass burning (see Sect. 3.6). (b) CCN fraction vs. CN concentration for specific segments from flight AC18 (see text for discussion).

0.5) and lower UFF (0.6–0.8), indicating larger particle sizes and likely a more aged aerosol. Segment D (blue), at 11–12 km altitude, had similar properties to E1. These observations confirm the presence of the two distinct types of elevated aerosol populations in the UT, introduced in Sect. 3.3. At one extreme, there are aerosols with very high N_{CN} and ultrafine fractions and low CCN fractions (e.g., E2), presumably representing newly formed particles with sizes too small to act as CCN. At the other extreme, there are populations with modest N_{CN} , but low UFF and high CCN fractions, indicating a more aged aerosol with larger particles (e.g., E1 and D).

The existence of these two populations is confirmed in plots of $N_{CCN0.5}$ and $N_{CCN0.5}/N_{CN}$ against supersaturation. Examples are shown in Fig. 13a and b, with AC18-DD representing a segment dominated by larger and aged particles, AC07-F a region with high concentrations of small and younger particles, and AC09-AA a mixed case with short periods of very high N_{CN} over a background of moderately elevated particle concentrations. Even though the mean

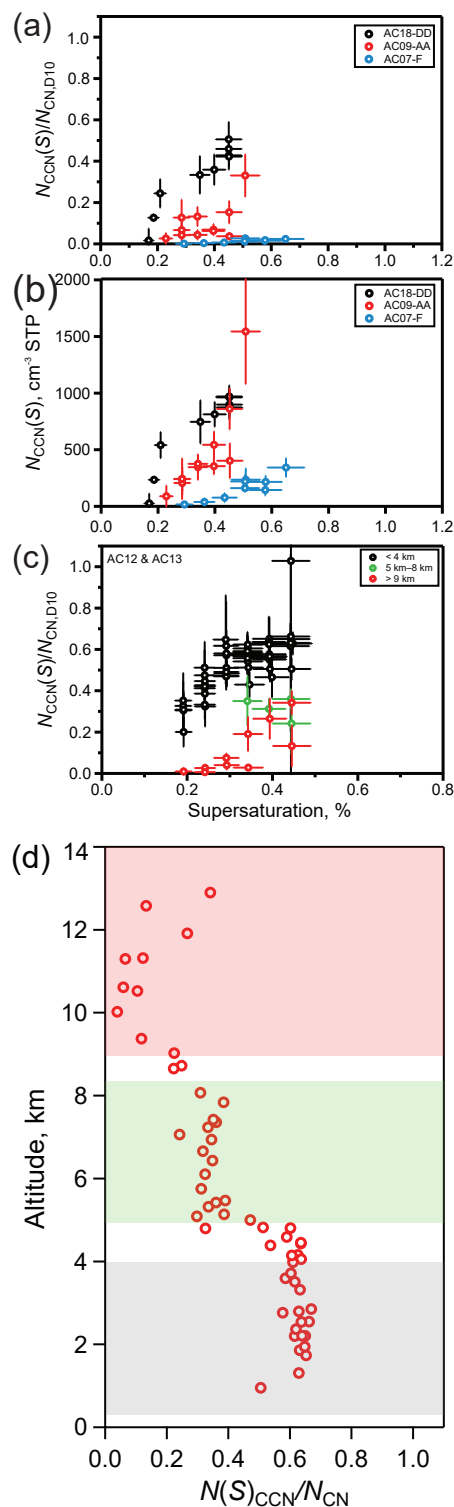


Figure 13. (a) CCN fractions ($N_{CCN0.5}/N_{CN}$) and (b) CCN concentrations ($N_{CCN0.5}$) vs. supersaturation from selected legs from flights AC07, AC09, and AC18; (c, d) data from flights AC12 and AC13 for the LT, MT, and UT.

CN concentration exceeds 8900 cm^{-3} in AC07-F, the mean $N_{\text{CCN}0.5}$ in the same region is only 13 cm^{-3} , and therefore the $N_{\text{CCN}0.5}/N_{\text{CN}}$ vs. S plot falls essentially on the baseline. In contrast, AC18-DD presents a fairly “classical” supersaturation spectrum, and AC09-AA is a mixed case with the measurements made during the N_{CN} peaks showing very low $N_{\text{CCN}0.5}/N_{\text{CN}}$.

In Fig. 13c and d, we compare the mean supersaturation spectra from the lower, middle, and upper troposphere obtained on flights AC12 and AC13, which were taken on successive days over the same region and where the LT was influenced by biomass burning pollution. In the LT, the CCN fraction is in the range observed at ground level at the Amazon Tall Tower Observatory (ATTO) site (Pöhlker et al., 2016) and in close agreement with measurements in the southern Amazon during the biomass burning season (Vestin et al., 2007). In the UT, we observed low CCN fractions representing the regions with high N_{CN} and UFF, mostly at altitudes of 10–11 km, and higher CCN fractions at and above 12 km, corresponding to a region with somewhat elevated CCN ($1000\text{--}1500\text{ cm}^{-3}$; see Fig. 11b, which shows the CCN concentrations from these flights). In the middle troposphere (5–8 km), we found intermediate CCN fractions, consistent with a mixture of LT and UT aerosols.

3.4.3 Volatility

On several flights (AC16, 18, 19, and 20), a second CPC was operated behind a thermodenuder at a temperature of $250\text{ }^{\circ}\text{C}$, in parallel to the regular CPC, providing the concentration of non-volatile particles, N_{nonvol} . The results of these measurements are shown in Fig. 14a in the form of the volatile fraction ($\text{VF} = (N_{\text{CN}} - N_{\text{nonvol}})/N_{\text{CN}}$) plotted against altitude. In the LT, most particles are non-volatile and the VF is typically between 0.1 and 0.2. This is consistent with the behavior described by Clarke and Kapustin (2010) and Thornberry et al. (2010), who found that aged combustion aerosols (from biomass or fossil-fuel burning) are non-volatile and mostly in the accumulation-mode size fraction. With increasing altitude, the VF increases, closely resembling the profile of the UFF. In the UT, the mean VF reaches about 0.8 and approaches 1.0 in the most highly enriched layers (e.g., segment E2). In previous campaigns, high volatile fractions had also been observed in the tropical UT and TTL, with the highest VF in the region between 340 and 360 K potential temperature, corresponding to about 9–15 km (Borrmann et al., 2010; Weigel et al., 2011).

More detail can be seen when looking at data from an individual flight. In Fig. 14b, we show the profiles from AC18, which we had already discussed in the context of CCN concentrations in the previous section. The profiles (segments A–C and F) show the overall increase in VF with height, with peak values at embedded high-CN layers. The freshest layer (E2), which had the highest UFF, also has the highest VF. In contrast, segments D and E1, represent-

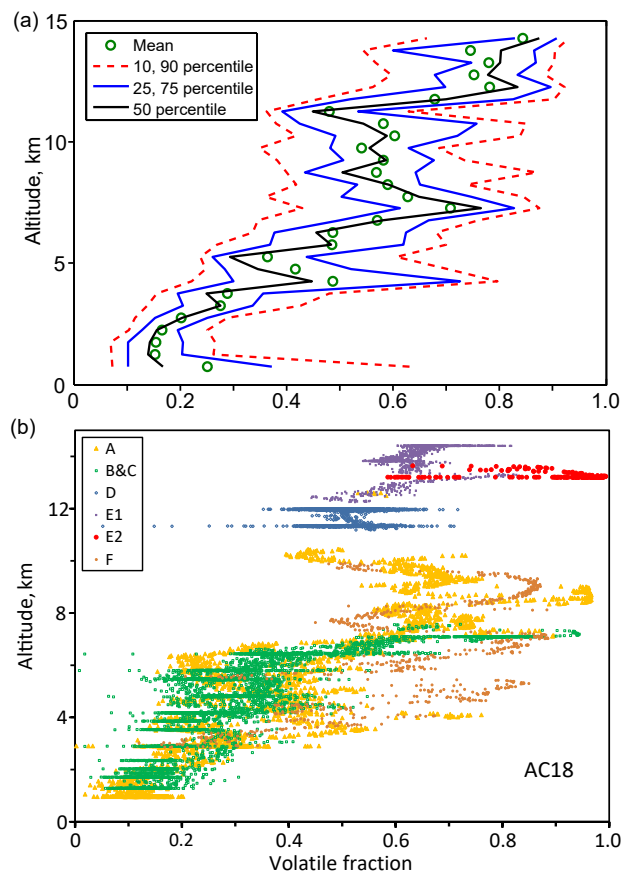


Figure 14. Volatile fraction. (a) Statistics from all flights; (b) individual segments from flight AC18 (see text for discussion).

ing larger UT regions with moderate CN enrichments, larger particles, and higher CCN fractions also have lower VFs, between 0.4 and 0.7. A contribution from aged combustion aerosols can be ruled out as source for the non-volatile particles in these layers, because the rBC concentrations are close to zero (see below). As we will show in the next section, it appears that these low-volatility particles represent a more aged organic aerosol.

3.4.4 Chemical composition

As discussed above, the LT aerosol over the Amazon during the dry season is dominated by the products of biomass burning, with increasing concentrations from north to south. This is clearly reflected in its chemical composition, which is dominated by carbonaceous matter (organic and elemental carbon) and only contains minor fractions of inorganic species, such as potassium, sulfate, and nitrate. Elemental or black carbon is a unique tracer of combustion emissions and was measured on HALO in the form of rBC.

The vertical profile of rBC shows a sharp separation between the LT and FT (Fig. 15). The average rBC concentration in the region below 5 km was

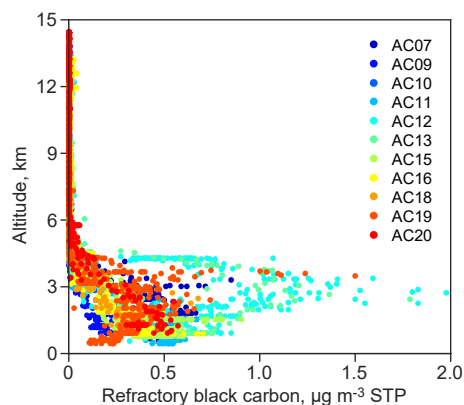


Figure 15. Refractory black carbon vs. altitude for all flights (30 s averages).

$0.25 \pm 0.21 \mu\text{g m}^{-3}$, whereas in the FT above 6 km it was $0.002 \pm 0.006 \mu\text{g m}^{-3}$ in terms of mass concentrations, and $99 \pm 92 \text{ cm}^{-3}$ vs. $1.5 \pm 2.5 \text{ cm}^{-3}$ in number concentrations of rBC particles. Interestingly, these concentrations over the Amazon Basin are only slightly higher than the values measured over the tropical western Atlantic during the Saharan Aerosol Long-range Transport and Aerosol-Cloud-Interaction Experiment (SALTRACE; Weinzierl et al., 2017), June–July 2013: about $0.2 \mu\text{g m}^{-3}$ in the LT and about $0.001 \mu\text{g m}^{-3}$ in the FT (Schwarz et al., 2017), which suggests that a significant fraction of the rBC is entering the basin by long-range transport from Africa. Transport of biomass smoke containing BC and other constituents from Africa to South America has been documented previously, e.g., from northern Africa during the wet season (Talbot et al., 1990; Q. Wang et al., 2016) and from southern Africa during the dry season (Andreae et al., 1994). A detailed study on the transport of southern African aerosols to the Amazon during ACRIDICON–CHUVA is in preparation and will be published elsewhere.

In 14 instances, elevated rBC concentrations were seen for short durations (usually less than 30 s) in the UT. Most of the time, they occurred during cloud penetrations in the course of vertical cloud microphysics profiling. In the case of the flights over the northern half of the Amazon Basin, they could likely be attributed to sampling of HALO's own exhaust, based on the flight track and the presence of associated NO enhancements in the absence of strong enhancements of CO and other aerosol species (CCN, N_{acc} , N_{CN}). On flights over the southern Amazon (AC07, AC12, AC13, and AC20), where the PBL was more polluted and active fires were present, there were a few instances when elevated rBC coincided with peaks in CO and accumulation-mode particles, which suggests upward transport of biomass smoke aerosols. In view of the scarcity of such events during our campaign and their modest rBC concentrations, it is clear that they do not represent a major source of combustion aerosol

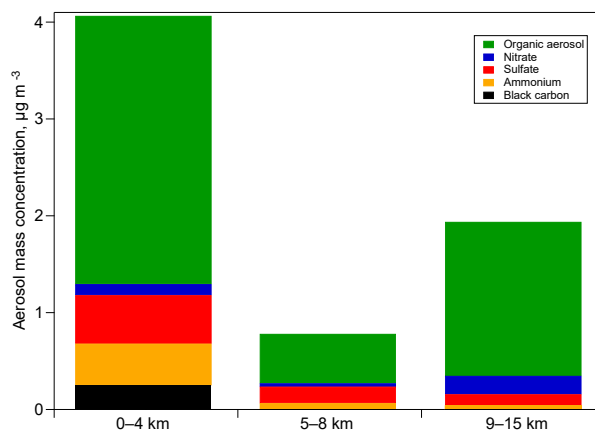


Figure 16. Aerosol chemical composition as determined by AMS and SP2 measurements in the lower, middle, and upper troposphere over Amazonia.

for the UT during our campaign. No elevated rBC concentrations were observed during the extensive outflow sampling legs on any of the flights. A detailed discussion of the rBC measurements during the campaign will be presented in a companion paper (Holanda et al., 2018).

The drop in rBC concentration by 2 orders of magnitude between the LT and FT implies that rBC, and by extension other aerosols (which are likely even more prone to being removed by nucleation scavenging), are efficiently removed during deep convection, and consequently that there is little transport of LT aerosols into the FT. This provides further evidence that enrichments in N_{CN} and N_{acc} in the FT cannot be explained by vertical transport of particles from the PBL.

The AMS measurements also show pronounced differences in the composition of the LT and UT aerosols (Fig. 16). In Table 2, we present a detailed analysis of the results from three flights, AC07 from a polluted region in the southern Amazon, and AC09 and AC18 from relatively clean regions in the northern and northwestern parts of the basin, respectively. Organic aerosol (OA) is the dominant aerosol species in all three regions at all altitudes, as expected in an area where biomass burning and SOA production are the dominant sources.

In the LT, (ammonium) sulfates (SO_4) are together with rBC the next-most important species after OA. Here, we see a clear difference between the BB-dominated region in the south (with high OA, ammonium (NH_4), and rBC, and relatively low SO_4) vs. the northern basin, where SO_4 , likely from long-range transport, plays a more important role. The OA / rBC ratio in the LT is in the range of 3–11, consistent with values from BB aerosols. The biomass burning marker, f_{60} (Schneider et al., 2006; Alfara et al., 2007), is present in all the measurements from the LT but always mixed with oxidized secondary organics. It should also be noted that the f_{60} marker is not an inert tracer but decays with time, and a

typical observed background level of the f_{60} tracer is 0.3 % of OA (Cubison et al., 2011).

In the UT, SO_4 shows lower concentrations than in the LT, with the most pronounced difference on flights AC07 and AC18. The latter flights also show a large difference in the OA / SO_4 ratio, which is around 10 in the UT and around 2 in the LT. Because of the high BB component in flight AC07, this ratio is also relatively high in the LT on this flight. The most pronounced differences between UT and LT are seen in the nitrogen species. Ammonium is usually present in the LT, sometimes at considerable levels (e.g., on AC07), but always below the detection limit in the UT. In contrast, nitrate (NO_3) is a minor species in the LT, whereas in the UT it is comparable to or greater than SO_4 , so that the NO_3 / SO_4 ratio is about an order of magnitude higher in the UT than in the LT. High concentrations of organics, especially oxidized organics, and nitrate had been seen previously in the UT by Froyd et al. (2009).

The nature of the nitrate signal in the UT cannot be definitely identified from our data. The absence of NH_4 and the ratio of the peaks associated with ammonium nitrate make it unlikely that the NO_3 signal represents ammonium nitrate (Fry et al., 2009; Bruns et al., 2010). It may be, at least to a large part, indicative of organonitrates, which have been shown to account for 15–40 % of SOA mass in laboratory experiments (Berkemeier et al., 2016) and whose formation is enhanced at low temperatures (Lee et al., 2014).

A closer look at the aerosol-enriched layers in the UT from these flights reinforces these conclusions (Table 2). In these layers, the OA / SO_4 and NO_3 / SO_4 ratios can reach very high values, especially in the SO_4 -poor UT of flight AC07. On flights AC09 and AC18, we encountered extended periods when N_{acc} and $N_{\text{CCN}0.5}$ were elevated, while N_{CN} did not show extremely high values (AC09-AA, AC18-AA, and AC18-DD). The AMS data from these segments were generally similar to the UT averages, suggesting that they are representative of the ambient UT aerosols. The layers with very high N_{CN} on these flights (AC09-BB, AC09-EE, AC09-A1 + A2, and AC18-A1, AC18-A2, AC18-E2, AC18-F) also did not show significant differences from the UT means on these flights, likely because the numerous but very small CN in these layers did not contain enough mass to influence the AMS measurements in a detectable way.

We attempted to examine this hypothesis further by investigating the size dependence of the AMS signals, but because of the small aerosol mass concentrations in the UT, size information from the AMS data required extended integration periods, which precluded obtaining size data from the relatively short segments with very high N_{CN} . The most robust size data were from the segments where relative high N_{acc} concentrations prevailed over extended periods of time, e.g., segment DD (Table 2) on flight AC18. Here, the OA showed a broad mode between 80 and 250 nm, with a modal diameter at 150 nm. This confirms that the AMS compositional data are dominated by the accumulation mode, while the particles

that make up most of the UF fraction in the UT do not have enough mass to provide a clear AMS signal. An exception may be some segments on AC09 (BB and EE), where OA and NO_3 data suggest a mass mode between 60 and 120 nm. Here, the UFF is quite high (0.85 and 0.92, compared to segment DD on flight AC18, where it was 0.61) suggesting a smaller and therefore younger aerosol population.

More detailed information on the origin of the organics in the UT aerosol can be obtained from specific markers. In the UT, the BB marker f_{60} is typically not detectable, which, in combination with the fact that the ratio OA / rBC is of the order of 1000, precludes a significant contribution of aerosols from biomass burning or other primary combustion aerosols to the OA in the UT. In contrast, the marker f_{82} , which is indicative of IEPOX-SOA formed by the photooxidation of isoprene (Robinson et al., 2011; Hu et al., 2015), is found in the aerosol-enriched layers in the UT, suggesting oxidation of isoprene and other BVOCs as the source of the OA. The f_{82} marker is not correlated with sulfate, which suggests that sulfate may not have been participating in the formation of the IEPOX-SOA. Furthermore, in all cases with high f_{82} , the aerosol is not neutralized by NH_4^+ . These issues will be discussed in detail in a forthcoming paper by Schulz et al. (2018).

The plot f_{43} vs. f_{44} is frequently used to represent the aging of organic aerosols (Ng et al., 2011). In Fig. 17, we show the median locations of the LT and UT aerosol in this plot, which indicates that both are fairly well aged and oxidized, with the UT data plotting towards slightly less oxidized and younger values. This may reflect an overall younger aerosol or the admixture of recent material either by condensation on the accumulation-mode particles or in the form of an external mixture of larger aged particles with small younger ones. The individual segments from flight AC18, which had the lowest OA / SO_4 and NO_3 / SO_4 ratios, also plot in this region, showing that they are dominated by a relatively well-aged aerosol. In contrast, segments AC09-AA, AC07-AA1, AC07-AA2, and AC07-GG, which have the highest OA / SO_4 and NO_3 / SO_4 ratios and much higher N_{CN} , plot much further to the lower right, indicating a less oxidized, fresher aerosol. On this flight, the concentrations of accumulation-mode aerosols in the UT were relatively low, so that freshly formed aerosol could be more evident because of a lower background of aged aerosol.

In summary, the chemical composition data show that, while both LT and UT aerosols are dominated by aged organics, their sources must be different because the UT aerosol is essentially devoid of the combustion tracers, rBC and f_{60} , whereas the OA / rBC ratios in the LT are consistent with combustion aerosols. Nitrate is strongly elevated in the UT and may consist to a large extent of organonitrates. NH_4 is a significant component in the LT, whereas it is below the detection limit in the UT. Size-selective chemical analysis is difficult because of the low aerosol mass concentrations, but the available data suggest that the AMS measurements

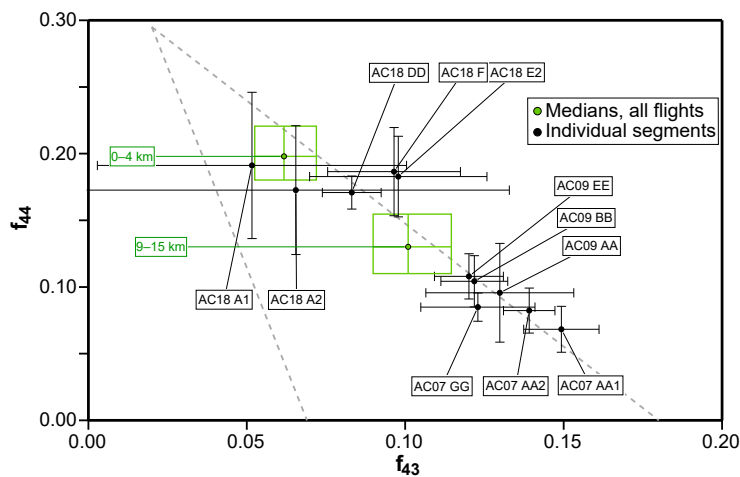


Figure 17. Plot of the AMS factors f_{44} vs. f_{43} , indicating the median values for the LT and UT and values for some UT flight segments with elevated aerosol concentrations. With increasing degree of oxidation, the measurements move to the upper left of the triangle.

are dominated by the accumulation mode, and the strong N_{CN} enhancements are not distinctly seen in the AMS data. Chemical marker analysis shows the general absence of BB tracers in the UT, while the marker f_{82} indicates production of IEPOX-SOA from isoprene. Most of the UT organics are aged and oxidized, but in some of the CN-enriched layers, younger and less oxidized OA was evidenced by much lower f_{44}/f_{43} ratios. A detailed discussion of the AMS measurements during ACRIDICON-CHUVA will be presented in Schulz et al. (2018).

3.5 The roles of long-range transport and deep convection

In the preceding sections, we have documented the differences between the aerosols in the LT and the UT, which rule out the possibility that convective transport of PBL aerosols can be an important source for the UT aerosols. This opens the question about the other potential sources of these particles: are they the result of long-range transport from remote sources or do they originate in the UT over the Amazon Basin? In the latter case, are they directly released in the outflow from the convective clouds or are they produced by subsequent nucleation and growth in the UT?

For the larger particles in the accumulation mode, represented by elevated N_{acc} and $N_{CCN0.5}$ in the UT, long-range transport cannot be excluded, because such particles can have long lifetimes in the upper troposphere (Williams et al., 2002). While the absence of detectable rBC still rules out an origin from pollution aerosols lofted from the LT, they may have formed days or weeks ago by gas-to-particle formation mechanisms anywhere in the free troposphere. In contrast, the high concentrations of small UF particles that we observed with high frequency in the UT cannot come from distant sources, as they persist only for hours to a few days

before growing to larger sizes while decreasing in concentration due to coagulation and dilution processes (Williams et al., 2002; Krejci et al., 2003; Ekman et al., 2006).

3.5.1 Aerosols in cloud tops, anvils, and outflows

First, we consider the possibility of these particles having been produced already inside the clouds and released by outflow into the UT. In earlier studies, NPF had been shown to occur in ice clouds in the tropical/subtropical UT, especially in conditions where the available surface area of ice particles was relatively low (e.g., Lee et al., 2004; Frey et al., 2011). To look for this phenomenon, we examined the particle concentrations during passages through the upper levels of deep convective clouds and in the anvils directly attached to active cumulonimbus clouds (Cbs). Our measurements during these passages consistently show lower CN and CCN concentrations than in the surrounding UT air, as exemplified in Fig. 18a by data from flight AC18. During this flight segment, we performed multiple penetrations of the tops of growing Cbs at altitudes between 10.7 and 12.0 km and temperatures in the range of 225 to 236 K. During each cloud passage (indicated in Fig. 18a by elevated ice particle concentrations), the aerosol concentrations decreased sharply to values of N_{CN} around 800 cm^{-3} and $N_{CCN0.5}$ around 250 cm^{-3} during the longer cloud passages. (Here, we use $N_{CCN0.5}$ as proxy for the accumulation-mode particles, since the N_{acc} measurements in clouds were perturbed by shattering at the probe tip, whereas the N_{CN} and $N_{CCN0.5}$ measurements showed no artifacts in ice clouds.) In the case of N_{CN} , the values in the cloud tops are about the same as the PBL concentrations measured in the same region, while for $N_{CCN0.5}$ they are significantly lower than the PBL values of around 400 cm^{-3} .

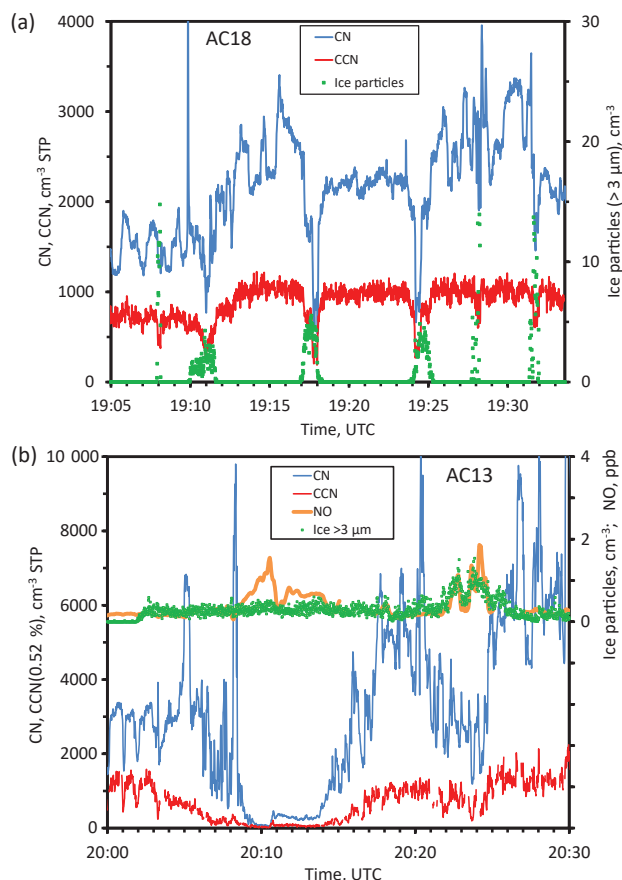


Figure 18. Measurements during passages through cumulonimbus cloud tops and outflow anvils: (a) several cloud top penetrations at 10.7 to 12 km altitude on flight AC18 showing reduced N_{CN} and $N_{\text{CCN}0.5}$ inside the cloud top; (b) outflow from a large active cumulonimbus, showing strong aerosol depletion and NO production by lightning.

The same behavior was found for all cloud penetrations in the UT during the campaign. In particular, extensive cloud top and outflow sampling on AC09, AC15, and AC16 showed $N_{\text{CCN}0.5}$ values down to 160–250 cm^{-3} and N_{CN} values down to 600–1000 cm^{-3} . The lowest particle concentrations were seen in a large outflow sampled on AC13 (20:08–20:30 UTC), when both N_{CN} and $N_{\text{CCN}0.5}$ reached values below 50 cm^{-3} (Fig. 18b). In this air mass, NO and NO_y were strongly elevated, indicating recent NO production by lightning in the large Cbs from which this outflow originated.

Given that the air sampled during the cloud passages had already mixed in by lateral entrainment some of the surrounding air with much higher particle concentrations (Bertram et al., 2007; Yang et al., 2015), these low particle concentrations in the cloud tops and outflows are clear evidence that in-cloud processes were a sink and not a source of particles in the size class measurable with our instrumentation. A rough estimate of the scavenging efficiency of the convective process can be gained by using CO as a con-

servative tracer. For example, on flight AC18, the PBL concentrations of CO and N_{CN} averaged ~ 120 ppb and 780 cm^{-3} , and the UT during the cloud penetrations around 19:00 UTC had CO ~ 95 ppb and $N_{\text{CN}} \sim 1500$ cm^{-3} . In the cloud, CO rose to 108 ppb and N_{CN} dropped to 750 cm^{-3} . Following the approach of Bertram et al. (2007), we can estimate that the fraction of PBL air in the center of the cloud was about 0.52, and that without scavenging, $N_{\text{CCN}0.5}$ would be about 1130 cm^{-3} . From these values, a scavenging loss of 90 % or more of CCN-size particles can be estimated, in good agreement with previous studies (e.g., Andreae et al., 2001; Yang et al., 2015) and consistent with the absence of detectable rBC.

Flight AC20 was the only exception to this behavior. Here, CN were strongly enhanced during cloud passages and even CCN were slightly elevated in some passages. The cloud that was sampled on this flight appears to have been a pyrocumulus that had been ingesting fresh biomass smoke, as suggested by the strongly elevated CO during the cloud passages. This flight will be discussed as a separate case study below (Sect. 3.6.).

While these results show that the high particle concentrations we observed in the UT were not directly released from the cloud tops, they do not rule out the possibility that new particle formation had already started in the clouds or anvils. This is because the newly formed particles observed in the earlier studies were almost exclusively in the size range below 20 nm (Lee et al., 2004; Frey et al., 2011). Since our measurements are limited to particle sizes > 20 nm, we would not have been able to detect such freshly nucleated particles, and therefore the earliest phases of particle nucleation and NPF over Amazonia will have to be addressed in future studies. Our data do show, however, that release of particles by hydrometeor evaporation following deep convection is not a net source of particles to the UT over Amazonia, in contrast to what was observed over the Indian Ocean region by Engström et al. (2008). Because the N_{CN} and $N_{\text{CCN}0.5}$ concentrations in the ambient air in the UT are actually higher than in the air detrained by the Cb clouds, the detrainment leads at least initially to a reduction in UT particle concentrations in the size class > 20 nm. Only through subsequent NPF can this be reversed and deep convection then become a net source of UT aerosols.

3.5.2 Relationship between aerosol enhancements and air mass history

Connections between the presence of aerosol enhancements and the outflow from convective systems had been observed in some previous studies (de Reus et al., 2001; Twohy et al., 2002; Benson et al., 2008; Weigelt et al., 2009). We examined the connection between deep convection (DC) and the presence of high CN concentrations by a combination of back trajectory calculations and the analysis of cloud top temperatures from GOES-13 weather satellite images, simi-

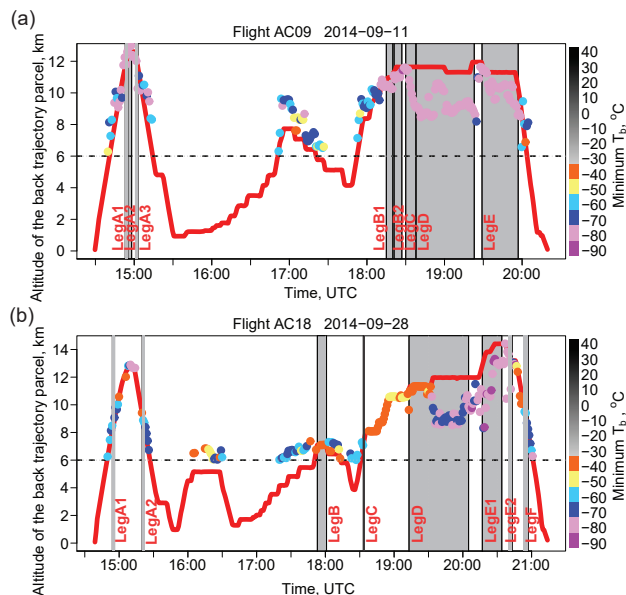


Figure 19. Air mass contacts with deep convection. The colors indicate the cloud top temperature of the convective system with which the trajectory had the most recent contact. The aircraft altitude at which the air mass was sampled is indicated by the red line. The colored dots are plotted at the altitude at which the air mass crossed the grid cell with the convective system. The dots are only plotted if this altitude is greater than 6 km and if it encountered a DC region (i.e., $T_b < -30^\circ\text{C}$). The shaded areas correspond to the flight segments with elevated CN concentrations. **(a)** Flight AC09, **(b)** flight AC18.

lar to the approach used in some previous studies (de Reus et al., 2001; Froyd et al., 2009; Weigelt et al., 2009). We analyzed back trajectories initialized at the aircraft locations where we had observed elevated aerosol concentrations, as listed in Table 1. Then we checked for each hour along the back trajectories whether the air mass had crossed a region with DC (cloud top temperatures below -30°C). The results show that in all cases, the aerosol-enriched air masses had encountered deep convection within the last 120 h.

In Fig. 19, we present the results from two flights (AC09 and AC18) as examples. We find that for all flight segments that showed high aerosol concentrations in the UT (dark shading), the air masses had made contact with DC with cloud tops typically reaching about -80°C . Of course, given the abundance of convection over Amazonia, it is to be expected that most air masses would have interacted with convection within 120 h (such as the example shown in Fig. S2). For comparison, over the northeastern United States during summertime, Bertram et al. (2007) had found that more than 50 % of UT air had encountered DC within the previous 2 days.

The cumulative plot of the time since the most recent DC contact (Fig. 20a) shows that on all flights (except AC19, the flight over the Atlantic) almost all aerosol-enhanced air masses had seen DC within the last 30–40 h. The cloud tops

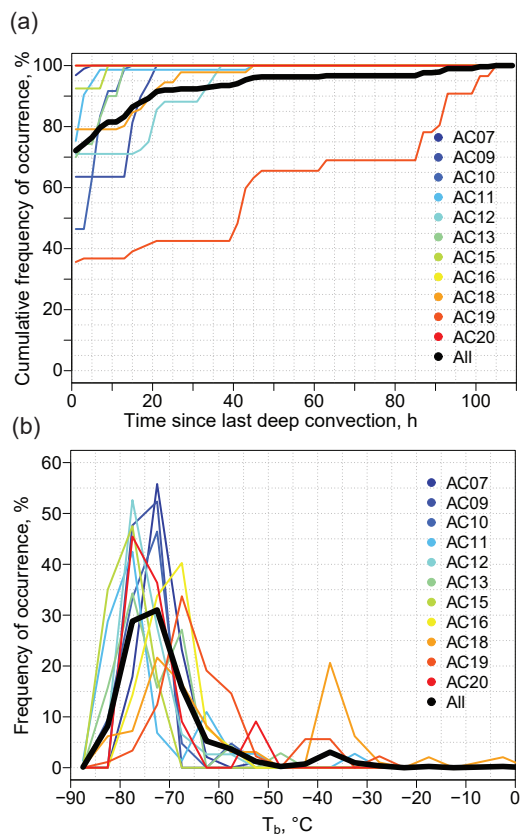


Figure 20. **(a)** Number of hours since last contact with deep convection for flight segments with elevated aerosol concentrations (cumulative frequency, all flights); **(b)** frequency distribution of minimum GOES brightness temperature (T_b) for selected flights legs (within 5-day backward trajectories).

during these encounters typically reached -70 to -80°C (Fig. 20b). In many cases, the air mass history analysis shows multiple contacts with deep convection within the preceding 72 h. It must be noted, however, that the physical interaction between a UT air mass and a specific deep convective event is not represented in the trajectory model. Because the model does not “see” the individual convective event that brings up an outflow, it cannot trace a parcel back into this outflow and back down to the boundary layer. On the other hand, an air parcel trajectory that passed through the vicinity of the outflow and may have ingested some of the outflowing air, will keep moving backward along the mean flow in the UT and may then encounter another outflow. Obviously, however, the uncertainty in the trajectory position increases with time going backwards and is probably enhanced by passage near a region of active convection.

In some cases, the air masses could be tracked back to regions where the cold cloud encountered by the tracked air mass looked more like cirrus than identifiable deep convective outflow. The same favorable conditions for nucleation (low temperature, low pre-existing aerosol surface) as

in the outflow regions prevail also in native cirrus, and Lee et al. (2004) had reported NPF in cirrus without immediate connection to DC. This might also have occurred in our campaign, but it is usually difficult to distinguish cirrus and very aged outflow.

To test whether there was a difference in the air mass histories between segments with high and low N_{CN} , we searched our data for suitable segments with low N_{CN} . However, because of the high variability of the CN concentrations in the UT, the times when N_{CN} was below 3000 cm^{-3} were in almost all cases very short and would not lend themselves to a meaningful analysis of air mass history. To illustrate this variability, we show a full time series plot of the measurements from flight AC09 in the Supplement (Fig. S7).

We were only able to find a total of six segments, where N_{CN} was consistently below 3000 cm^{-3} , and which were not identifiably part of an outflow. These are listed in Table S1 in the Supplement. The segments from flights AC16 and AC18 were well away from clouds, whereas those from AC19 and AC20 were in the vicinity of Cbs but not clearly in an outflow. The segment L from AC19 is low in CN, but actually has a relatively high $N_{\text{CCN}0.5}$, and may not really be significantly different from the aged enriched segment E2, which was sampled immediately after it. Consequently, we do not have a data set that would allow a representative analysis of the history of air masses with low particle concentrations. Notably, however, the air mass trajectory types in these segments do not contain type D, i.e., recirculation within the Amazon Basin. The air in the segments from AC20, which had the lowest particle concentrations, had come in straight from the Pacific within the last 48 h but may also contain some outflow air.

Information about the time required for particle production and the evolution of the aerosol populations in the UT can be derived from a close examination of the trajectories for individual flight segments. Flight AC18 provides some illustrative examples. The trajectories of the first particle plumes encountered (A1 and A2, Table 1) had passed close to areas of intense deep convection (-30 to -60 °C) about 17–21 h before sampling. Because it is likely that the aerosol precursor substances are formed by photochemical reactions, we also looked at the amount of time that the air mass was exposed to sunlight (Lee et al., 2003). Since the convective encounters occurred between 16:00 and 00:00 LT and the measurements were taken at about 11:00 LT, the air mass had only about 5–7 h of Sun exposure. Assuming that the formation of the particles required photochemical processes, this implies that about 5–7 h were sufficient to produce particle concentrations above $20\,000 \text{ cm}^{-3}$ with sizes $> 20 \text{ nm}$. The enrichment in this case occurred only in the particles size range $< 90 \text{ nm}$, with a UFF of about 0.98, while N_{acc} remained at the same levels as in the surrounding background FT. Segment F, near the end of the flight, was sampling a similar region as A1, with a similar air mass trajectory. Since this segment was taken near the end of the day, the air mass had experienced

about 11 h of sunlight. There is somewhat of a shift towards larger particles, but this might also be coincidental.

The air in segments B and C had traveled along similar trajectories as A1 and A2, but unfortunately there are no GOES images available for the time when they crossed the convective region encountered by A1 and A2, and so no conclusions can be drawn for these segments. Segments D and E1 represent air masses that had made multiple and extended convection encounters over the central and western Amazon during the past 3 days. Here, we find only weak enhancements in N_{CN} , but significantly elevated $N_{\text{CCN}0.5}$ and N_{acc} , with a UFF of 0.73 and 0.82, respectively, suggesting that coagulation and growth had taken place over this time period.

Some of the highest N_{CN} (up to about $45\,000 \text{ cm}^{-3}$) and UFF (0.98) were found in segment E2 of flight AC18, which was sampling the air just a few hours downwind of a massive convective system that reached well above our flight altitude of almost 14 km. The air sampled here had traveled for about 1 h after leaving the convective complex before being encountered by HALO and had been interacting with this complex for up to 5 h, all of them in daylight. As in A1, A2, and F, there was no detectable enhancement in aerosol mass, as represented by N_{acc} and $N_{\text{CCN}0.5}$. In contrast to this very fresh aerosol with high number concentrations, the strongest enhancement in aerosol mass was seen in the early part of segment E1, which did not show a strong increase in number concentration. The air during this segment had made its last contact with a convective system about 65–72 h before sampling.

Another illustrative case is flight AC09 over a clean region in the northern Amazon. Segments A1–A3 sampled clear air that had DC contact about 16 and 60 h ago, and the UFF around 0.94 indicated a moderately aged aerosol. Segments B1 and B2 were taken in air immediately surrounding a Cb anvil, with previous DC contacts at about 14, 80, and 120 h before. Here, the relatively low UFF of ~ 0.92 signaled no influence from the freshly outflowing air. Segments C–E were in air close to a Cb, within its anvil, and in a large anvil/outflow, respectively. Otherwise, they had a DC contact history similar to B. Here also, the UFF remains fairly low, and there is no evidence of new particle production directly in the anvil/outflow.

To summarize, our observations indicate that, while there is no evidence of immediate production of detectable particles (i.e., $> 20 \text{ nm}$) in the actual anvil or outflow, a small number of daylight hours are sufficient to produce very large concentrations of particles with sizes larger than about 20 nm in the FT. This is consistent with the observations made in the outflow of a convective complex off Darwin, Australia, where maximum Aitken concentrations were reported after about 3 h since the outflow (Waddicor et al., 2012). During NPF events in the FT on the Jungfrauoch, high concentrations of particles $> 20 \text{ nm}$ were observed about 4–6 h after sunrise (Bianchi et al., 2016). In the FT over other regions, growth may be considerably slower; for example, the

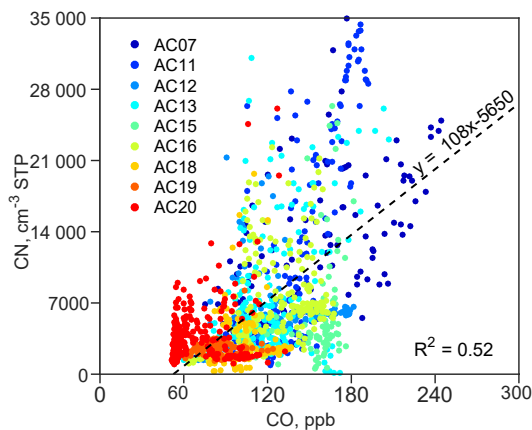


Figure 21. CN vs. CO concentrations in the upper troposphere above 8 km (15 s averages).

measurements over oceanic regions by Weigelt et al. (2009) showed that it took about 12 h for particles > 12 nm to reach their maximum concentrations.

Considerably longer times (a few days) are required, however, before increases are detectable in the size class > 90 nm. The development of significant amounts of particles in the accumulation mode appears to take 2 days or more, in agreement with the observations of Froyd et al. (2009), who had found enhanced aerosol organic mass concentrations over the Caribbean in UT air originating from Amazonia after 2–4 days in the atmosphere. Since many, if not most, of our trajectories remain over Amazonia for this amount of time, there is enough time available in the UT over the Amazon Basin to produce CCN-sized aerosols within the region, which can subsequently be transported downward to the LT or be exported to other regions.

3.5.3 Aerosol enhancements and chemical tracers

The relationship between new particle production and the input of boundary layer air is also reflected in a correlation between N_{CN} and CO. When taking all data above 8 km, this correlation is highly significant given the large number of data points ($N = 68\,360$) but not very close ($r^2 = 0.52$) because of the large variability of CO concentrations in the PBL and UT background between flights (Fig. 21). Closer relationships are obtained when looking at individual flights and especially at individual profiles within flights.

Weigel et al. (2011) had seen a strong correlation between CO and nucleation-mode particles over west Africa and interpreted it as indication of anthropogenic inputs. In contrast, over Amazonia, we have not seen any evidence that UT aerosol production shows any relationship to boundary layer pollution, and we interpret the correlation between N_{CN} and CO simply as reflecting the input by the cloud outflow of air from the PBL, which generally has higher CO concentrations than the UT.

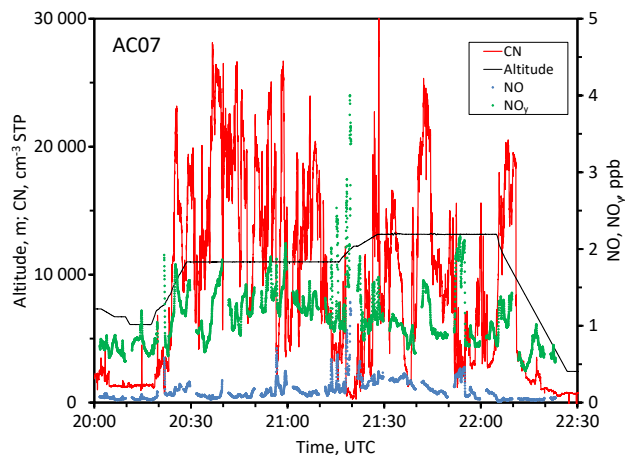


Figure 22. CN, NO, and NO_y concentrations in a flight segment in the upper troposphere on flight AC07.

An opposite relationship is generally seen between N_{CN} and O_3 , which tends to be lower in the particle-enriched layers. We also see this as an indication of injection of air from the PBL, which generally has lower O_3 concentrations than the UT. Because of the great variability in the O_3 concentrations in the UT, there is no general correlation between N_{CN} and O_3 for the entire mission ($r^2 = 0.02$). For individual flights, modest but statistically significant negative correlations can be found, e.g., an r^2 value of 0.13 ($N = 8509$) in the UT on flight AC09. The scatter plot in Fig. S08 shows that high O_3 concentrations were always associated with low N_{CN} , but that there were low- O_3 regions in the UT both with and without enhanced particle concentrations.

To look for a possible relationship between water vapor concentration and NPF, we examined several flights (AC07, AC09, AC13, and AC18) for relationships between RH and N_{CN} . We found a tendency for the layers with high N_{CN} to be associated with moister layers (RH > 50 %), but there were also many exceptions. This relationship may simply have to do with the fact that moisture was brought up with the convective clouds, or there may be a relationship with the actual particle formation process, but at this point we do not have the data needed to answer these questions.

The nitrogen oxides show a complex relationship with the particle enhancements in the UT, as illustrated in the example of a flight segment from AC07 (Fig. 22). The highest NO concentrations are found in the Cb anvils or freshest outflows, as identified by significant concentrations of ice particles (e.g., at 20:56, 21:19, and 21:54 UTC). In these regions, we typically observed particle minima, as discussed above. In these air masses, NO has been formed very recently by lightning, and the NO to NO_y ratios are usually still very high. Here, the particles are still depleted by convection scavenging and there has not been enough time for new particles to form, at least not in the size range detectable by our instrumentation. On the other hand, there is a strong positive

relationship between NO_y and N_{CN} , as seen in Fig. 22 during the entire period from 20:51 to 22:10 UTC. Regions with high concentrations of new particles generally show elevated NO_y , typically in the range of 1 to 3 ppb, indicating that photochemical reactions had taken place that both produced new particles and converted NO to NO_y .

3.6 Flight AC20: a special case with NPF from biomass smoke

On flight AC20, HALO performed detailed sampling of the anvil and outflow of a large Cb over northern Rondônia, a state with a high incidence of deforestation and pasture burning. Numerous outflow penetrations around this Cb were made, and the ice particles sampled here could be clearly identified as freshly produced in the Cb top. The CN concentrations in the UT away from the outflow were unimpressive, typically in the range of 2000 to 10 000 cm^{-3} . However, in sharp contrast to the other flights, where the air in the outflow always had been depleted in aerosol particles, on this flight, the outflow often showed much higher CN concentrations, between 10 000 and 20 000 cm^{-3} (Fig. 23a). The concentrations of CCN and non-volatile CN in the outflow were either the same as in the surrounding air or slightly higher, also contrasting with the observations on the other flights, where they had been depleted. Since the N_{CN} in the outflow were also much higher than in the PBL ($\sim 2000 \text{ cm}^{-3}$), entrainment of PBL air cannot explain the CN enrichment.

The mixing ratios of CO, NO, and NO_y were also elevated in the outflow (Fig. 23b), which in the case of CO and NO_y might be explained by inputs from the PBL, where CO and NO_y levels were around 120–200 ppb and 2–3 ppb, respectively. The NO values in the PBL, on the other hand, were only about 0.13 ppb, similar to the UT background values, requiring an additional NO source for the outflow.

The explanation for this unusual behavior may be found in the layer between 11.5 and 12.5 km that was penetrated during both ascent and descent (Fig. 23c). In this layer, N_{CN} reached 30 000 cm^{-3} , CO was elevated to ~ 140 ppb, N_{acc} to 850 cm^{-3} , and NO_y to ~ 1.6 ppb. The data also suggest a slight enrichment in rBC, but this is close to the limit of detection. These values suggest that this is a detrainment layer polluted with biomass smoke, as we have often seen on previous campaigns over the burning regions in southern Amazonia (Andreae et al., 2004). An urban origin of this pollution is unlikely, since the only town in the region, Porto Velho, lies about 50–100 km downwind of the sampling area.

For a comparison with biomass smoke, we computed the enhancement ratios, $\Delta N_{\text{acc}}/\Delta \text{CO}$ and $\Delta \text{CCN}_{0.5}/\Delta \text{CO}$, as the slopes of the bivariate regression between these variables for the time period between 16:53 and 16:58 UTC. The enhancement ratios in this layer differ clearly from fresh biomass smoke. The $\Delta N_{\text{acc}}/\Delta \text{CO}$ ratio is $\sim 6\text{--}12 \text{ cm}^{-3} \text{ ppb}^{-1}$ and the $\Delta \text{CCN}_{0.5}/\Delta \text{CO}$ ratio about $2.5 \text{ cm}^{-3} \text{ ppb}^{-1}$, much lower than the typical ratios in fresh

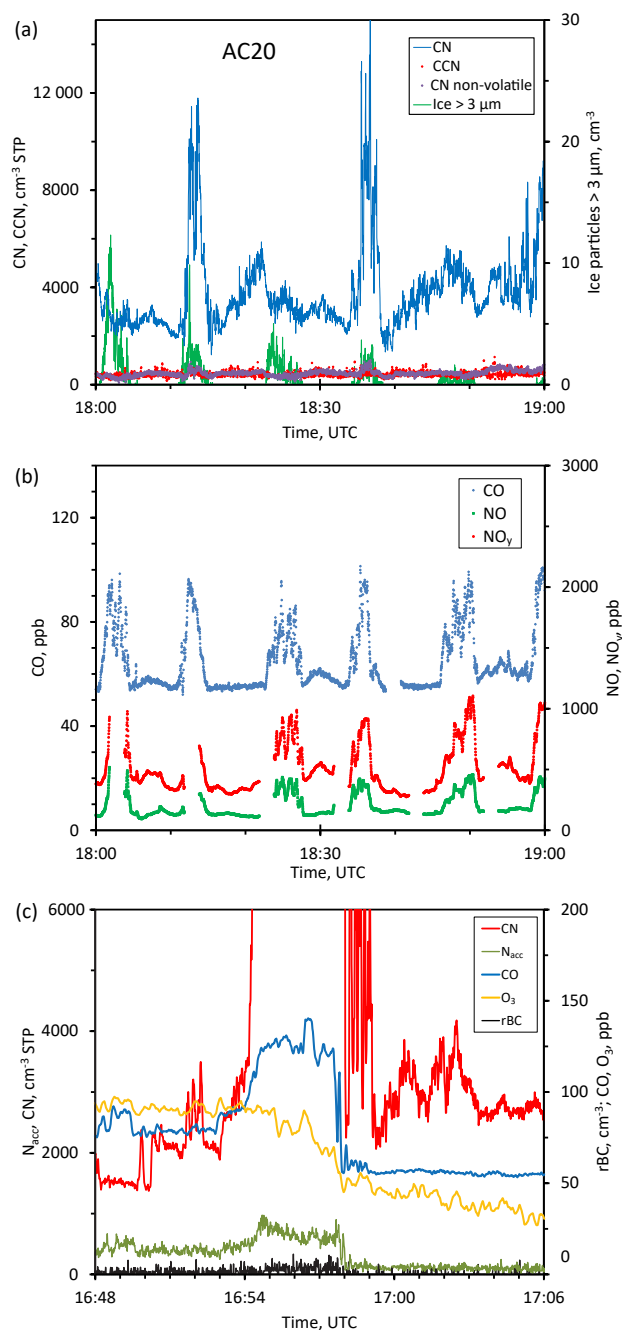


Figure 23. (a) Measurements of $N_{\text{CCN}_{0.5}}$, N_{CN} , N_{nonvol} , and ice particles during cloud top penetrations on flight AC20 at altitudes between 12.3 and 13.5 km. (b) Concentrations of CO, NO, and NO_y on the same flight segments. (c) Measurements of N_{acc} , N_{CN} , rBC, CO, and O_3 during the climb from 11.0 to 13.5 km.

smoke, which are about $20\text{--}40 \text{ cm}^{-3} \text{ ppb}^{-1}$ (Janhäll et al., 2010), indicating removal of CCN-sized particles during the convective transport. In contrast, the ratio $\Delta \text{CN}/\Delta \text{CO}$ was about $350 \text{ cm}^{-3} \text{ ppb}^{-1}$, almost an order of magnitude above the values typical of fresh smoke. These results suggest

that biomass smoke was brought to the UT either from the strongly smoke-polluted PBL in this region or actually by a pyro-Cb over an active fire, and that the concentration of the larger primary smoke particles was strongly reduced by scavenging, which allowed new particle formation in this smoke layer. The enrichments seen in the outflow penetrations at altitudes above the 12 km layer may be the result of entrainment of air from this layer or of rapid particle formation in situ. Further evidence for the upward transport of pyrogenic emissions was found in measurements on a horizontal leg at 11 km, which had only modest CN concentrations (around 1700 cm^{-3}), but elevated CCN, NO_y , CO, and aerosol nitrate and organics, with values similar to the biomass-burning-polluted boundary layer below. While we have these kinds of observations from only one flight, which took place over the most polluted region sampled during this campaign, they are suggestive of the potential of rapid particle formation and growth in smoke detrainment layers, an issue that merits further study in future campaigns.

3.7 Conceptual model and role in aerosol life cycle

The discussion in the preceding sections can be summarized in a conceptual model of the aerosol life cycle over the Amazon Basin (Fig. 24). Cloud updrafts in deep convection bring air from the PBL into the middle and upper troposphere, where it is released in the convective outflow (Krejci et al., 2003). During this process, most pre-existing aerosols are removed by precipitation scavenging, especially the larger particles that account for most of the condensation sink (Ekman et al., 2006). Most likely, organic compounds with low and very low volatilities are also removed by deposition on hydrometeors, which provide a considerable amount of surface area inside the clouds (Murphy et al., 2015).

On the other hand, the rapid transport of PBL air to the UT inside deep convective clouds facilitates lofting of the more volatile reactive BVOCs from the Amazon boundary layer (Colomb et al., 2006; Apel et al., 2012). Here, the initially O_3 - and NO_x -poor boundary layer air is supplied with O_3 by mixing with UT air and addition of NO from lightning, creating a highly reactive chemical environment. This mixture is exposed to an extremely high actinic flux due to the high altitude and multiple scattering by ice particles. Because of the low air mass at UT altitudes, the actinic flux is already very high shortly after sunrise. In this environment, rapid photooxidation of BVOCs and formation of ELVOCs/HOMs is to be expected. In laboratory studies, ELVOCs/HOMs have been shown to be rapidly produced at fairly high yields both by ozonolysis of terpenes and by reactions with OH radicals (Ehn et al., 2014; Jokinen et al., 2015; Berndt et al., 2016; Dunne et al., 2016).

The outflow regions in the UT present an ideal environment for particle nucleation, as had already been suggested in some earlier studies (Twohy et al., 2002; Lee et al., 2004; Kulmala et al., 2006; Weigelt et al., 2009). The temperatures

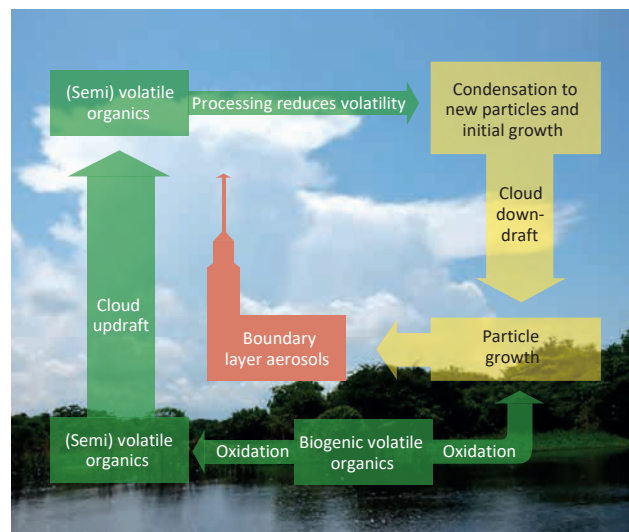


Figure 24. Conceptual model of the aerosol life cycle over the Amazon Basin.

are some 60–80 K lower than in the PBL, which decreases the equilibrium vapor pressure of gaseous species (Murphy et al., 2015) and increases the nucleation rate. Based on classical nucleation theory and molecular dynamics calculations, Yu et al. (2017) have estimated an increase in nucleation rate by 1 order of magnitude per 10 K. Nucleation rate measurements in the CERN CLOUD chamber indicate a similar temperature dependence (Dunne et al., 2016). Note, however, that these temperature dependencies are based on measurements for inorganic NPF, and that while the trends for organics are expected to be similar, the magnitude of the increase in nucleation rates for organics may be quite different. Because the pre-existing aerosol has been depleted during the passage through convective clouds before being released into the UT from the cloud outflow, the low particle surface area in the UT presents only a small condensation sink and thus very little competition to nucleation (Twohy et al., 2002; Lee et al., 2003, 2004; Young et al., 2007; Benson et al., 2008).

In the absence of measurements of the relevant gaseous sulfur species and the composition of the nucleating clusters, we cannot make firm conclusions about the actual nucleation mechanism. Over marine regions and polluted continental regions, the particles observed in outflows and in the UT were mostly identified as sulfates (Clarke et al., 1999; Twohy et al., 2002; Kojima et al., 2004; Waddicor et al., 2012), and consequently H_2SO_4 has been proposed as the nucleating species. However, since in some cases this identification was based only on the volatility of the particles and not on chemical measurements, they could have also consisted of organics or mixtures of organics and H_2SO_4 . Over the Amazon, nucleation by H_2SO_4 cannot be excluded based on our observations, especially if there was already some SO_2 or H_2SO_4 present in the UT before the injection of the organic-rich

PBL air. However, since the Amazonian BL contains very little SO₂, the sulfur species would have had to come from outside the region, and thus they would have had the opportunity to be oxidized to H₂SO₄ and nucleate into particles well before entering Amazonia during their several days of travel in the UT. It is therefore likely that the particles in the Amazon UT are formed by homogeneous nucleation of organics, as has been suggested by several authors (Kulmala et al., 2006; Ekman et al., 2008; Murphy et al., 2015). Nucleation by formation of clusters containing both H₂SO₄ and oxidized organic molecules is of course also a possibility that we cannot exclude (Metzger et al., 2010; Riccobono et al., 2014). However, recent studies have shown that HOM compounds can nucleate to form particles even in the absence of H₂SO₄, especially in the UT (Bianchi et al., 2016; Kirkby et al., 2016), and nucleation of HOMs without involvement of H₂SO₄ has been suggested to be the dominant mode of new particle formation in large parts of the pre-industrial atmosphere by the modeling study of Gordon et al. (2016). The importance of ions produced from cosmic radiation in this nucleation process is still controversial (Lee et al., 2003; Yu et al., 2008; Bianchi et al., 2016; Kirkby et al., 2016).

Regardless of the actual nucleating species, H₂SO₄ or HOMs/ELVOCs, the growth of the particles observed in our campaign must have been dominated by organics, as shown by the composition of the aerosol measured by the AMS. The dominance of organics in the growth of aerosols in pristine environments has also been suggested on the basis of measurements and modeling studies, both for the lower troposphere (Laaksonen et al., 2008; Riipinen et al., 2011, 2012; Öström et al., 2017) and the UT (Ekman et al., 2008; Murphy et al., 2015). In particular, isoprene-derived SOA has been suggested to be important in the growth of sub-CCN-size particles to CCN (Ekman et al., 2008; Jokinen et al., 2015), which would be consistent with the prevalence of isoprene in the Amazonian PBL and our observations of IEPOX-SOA in the UT aerosol. As the particles grow, the decrease of the Kelvin (curvature) effect with increasing size of the growing particles implies that subsequently relatively more volatile organics can condense (Tröstl et al., 2016), in agreement with the observed high volatile fraction we observed in the upper tropospheric CN.

While in general the volatile fraction of the particles in the UT was very high, there were also regions with a significant fraction of particles that did not evaporate at 250 °C (see Sect. 3.4.3). These were dominated by relatively aged organics, which, based on the absence on detectable rBC, must also be of secondary origin. Such thermally refractory organics may explain the presence of non-volatile particles in the tropical upper troposphere – lower stratosphere (UTLS), which had been observed in previous campaigns especially in the region above 360 K (Borrmann et al., 2010).

Once particles have nucleated in the UT and grown into the Aitken-mode and in some cases even into the accumulation-mode size ranges, they can be transported downward towards

the lower troposphere both by general subsidence under the prevailing high pressure system over Amazonia and by downdrafts associated with deep convective activity. Large-scale entrainment of UT and MT air into the boundary layer has been suggested as the major source of new particles in marine regions (Raes, 1995; Katoshevski et al., 1999; Clarke et al., 2013). Over Amazonia with its high degree of convective activity, downdrafts are likely to play a more important role. Downward transport of UT air by downdrafts associated with deep convective activity has been shown to inject air with lower moisture content, lower equivalent potential temperature, and elevated O₃ into the PBL (Zipser, 1977; Betts et al., 2002; Sahu and Lal, 2006; Grant et al., 2008; Hu et al., 2010; Gerken et al., 2016). It would follow that the same mechanism also brings down aerosol-rich air from the UT into the PBL. Indeed, in a recent aircraft study over the central Amazon, this mechanism was shown to be an important source of atmospheric aerosols, predominantly in the Aitken mode, to the Amazonian PBL (J. Wang et al., 2016). Here, they can continue to grow into the accumulation mode by condensation of BVOC-derived organics and become available as CCN, closing the aerosol cycle over Amazonia.

This mechanism provides an explanation for the origin of secondary aerosol particles in the clean Amazon PBL, where the occurrence of “classical” nucleation events, characterized by the rapid appearance of large numbers of particles < 10 nm and subsequent growth into an Aitken mode (e.g., Kulmala and Kerminen, 2008), has never been reported, in spite of several years of observations by several teams (Martin et al., 2010; Rizzo et al., 2013; Andreae et al., 2015). This has been attributed to the low emissions of gaseous sulfur species in the basin (Andreae and Andreae, 1988; Andreae et al., 1990a), which result in H₂SO₄ vapor concentrations that are too low to induce nucleation (Martin et al., 2010). Nucleation of particles from organic vapors alone is not favored in the Amazonian PBL because of high temperatures and humidity as well as the competition by the condensation sink on pre-existing particles, which results in organic coatings on almost all primary and secondary particles in the Amazonian PBL (Pöschl et al., 2010; Pöhlker et al., 2012).

4 Summary and conclusions

As part of the ACRIDICON–CHUVA 2014 aircraft campaign, we investigated the characteristics and sources of aerosols in the upper troposphere over the Amazon Basin. We observed regions with high number concentrations of aerosol particles (tens of thousands per cm³ STP) in the UT on all flights that reached above 8 km. The aerosol enhancements were commonly in the form of distinct layers with thicknesses of a few hundred to a few thousand meters. Such layer structures are a common feature of the free troposphere and

have been related to detrainment from deep convection and large-scale subsidence (Newell et al., 1999).

In other regions, upward transport of aerosols from the PBL had been suggested to be an important source of UT aerosols, based on the abundance of low-volatility particles (Clarke and Kapustin, 2010), Transmission Electron Microscope (TEM) analysis of individual particles (Kojima et al., 2004), or modeling of cloud processes (Yin et al., 2005). Over Amazonia, however, our study showed that the UT aerosol was fundamentally different from the aerosol in the LT, indicating that upward transport of PBL aerosols, especially combustion aerosols from BB, is not an important source of aerosols to the Amazonian UT.

The number concentrations of particles in the UT were often several orders of magnitude higher than in the LT, and their size distribution was dominated by the Aitken rather than the accumulation mode. In contrast to the LT, the particles in the UT were predominantly volatile at 250 °C and had much higher organics and nitrate contents. The extremely low concentrations of rBC in the MT and UT show that the aerosols above the LT are not combustion derived and indicate that the low-volatility fraction must be representing secondary organics of extremely low volatility (ELVOCs/HOMs). Regarding the size class large enough to act as CCN (i.e., larger than 60–80 nm), we can conclude based on the absence of rBC and the lack of BB indicators in the AMS measurements that the enhanced CCN in the UT are not related to upward transport of combustion products, in contrast to most previous studies (e.g., Krejci et al., 2003; Engström et al., 2008; Clarke et al., 2013).

By analyzing the history of the particle-enriched air masses and comparing the transport paths to GOES infrared imagery, we could show in all cases that these air masses had been in contact with deep convective outflow. Measurements inside the cloud tops and the outflow anvils close to the clouds showed that the pre-existing aerosols in the ascending air had been almost completely scavenged by in-cloud processes, making the clouds initially a net aerosol sink. The near-complete scavenging is consistent with the hypothesized large water vapor supersaturation in pristine tropical deep convective clouds, which can nucleate particles that are much smaller than the commonly defined CCN (Khain et al., 2012).

Based on our measurements, we propose that BVOCs in the cloud outflow are rapidly oxidized to HOMs/ELVOCs, which because of the low temperatures and low condensation sink can form new particles, possibly together with H₂SO₄, and grow to sizes ≥ 20 nm within a few hours, making deep convective clouds an indirect aerosol source. This had also been concluded based on a large statistical sampling of UT air in the Northern Hemisphere by the CARIBIC aircraft measurement program (Weigelt et al., 2009). The importance of NPF in the UT for the budget of CN and CCN had been proposed previously on the basis of modeling studies (Yu et al., 2008; Merikanto et al., 2009; Carslaw et al., 2017), and

is evident in the global enhancement of CN in the UT, especially in tropical regions, seen in compilations of data from numerous aircraft campaigns (Yu et al., 2008; Reddington et al., 2017). In this way, aerosol production by BVOC oxidation in the UT can provide the “missing source” of FT organic aerosol, which had been deduced from a mismatch between models and observations (Heald et al., 2005). We emphasize that little is known about the reaction kinetics of BVOCs and the nucleation kinetics of particles at the low temperatures and pressures found in the UT. The observation of large-scale NPF in this part of the atmosphere makes laboratory investigations of these processes under UT conditions an important priority.

The high aerosol concentrations in the UT provide a reservoir of particles that are available for downward transport into the PBL both by large-scale downward motion and by convective downdrafts. In a recent study, we have shown that transport of aerosols by downdrafts from the free troposphere is an important, if not the dominant, source of particles to the LT over the Amazon (J. Wang et al., 2016). The particles that are produced by this mechanism in the UT over the Amazon (and probably other tropical continents as well) can be transported globally due to their long lifetime in the UT (Williams et al., 2002; Clarke et al., 2013) and affect the microstructure of low-level clouds after they eventually descend into the PBL, possibly at very large distances from the source areas of their precursors.

Our study and the results of some previous studies (Lee et al., 2003; Froyd et al., 2009) suggest that UT aerosol production is especially important in the tropics because of the high rate of BVOC production and the abundance of deep convection, but its relevance may also extend to temperate and boreal regions. Our measurements both in the Amazon and at a remote site in central Siberia, distant from SO₂ emission sources and thus experiencing very low H₂SO₄ concentrations, show that “classical” nucleation events are very rare to absent at such sites and may not provide a strong source of new particles (Heintzenberg et al., 2011; Andreae et al., 2015; Wiedensohler et al., 2017). Consequently, the UT may be an important, possibly even the dominant, source of tropospheric aerosol particles in regions that are not strongly affected by anthropogenic or natural primary aerosols. This would assign clouds a central role in the aerosol life cycle, controlling both the source and sink of aerosol particles, at least in regions of low anthropogenic pollution. Furthermore, the relevance of UT aerosol production may not be limited to the troposphere, because the UT and the TTL are also important reservoirs for the transport of particles into the lower stratosphere (Fueglistaler et al., 2009; Borrmann et al., 2010; Randel and Jensen, 2013). Organic aerosols in the lower stratosphere have been shown to have significant radiative effects (Yu et al., 2016).

The conceptual model proposed here implies a profound difference between the present-day polluted atmosphere and the pristine pre-industrial situation, especially over the con-

tinents. In the pristine atmosphere, the vertical gradient of particle number concentrations may have been from high values in the UT to low values in the PBL, as we have found in Amazonia. In polluted continental regions, on the other hand, nucleation and NPF occur predominantly in the lower troposphere, where they add to primary emitted particles (Spracklen et al., 2006), and which thus has become the dominant source region of atmospheric aerosols in today's atmosphere over much of the world. Average N_{CN} measured at ground level at polluted continental sites worldwide range between 3400 and 19 000 cm^{-3} in the compilation by Andreae (2009). In the UT, on the other hand, the median particle concentrations ($> 12 \text{ nm}$) measured in the CARIBIC program over polluted continents are $\sim 3500 \text{ cm}^{-3}$ over North America, $\sim 2500 \text{ cm}^{-3}$ over Europe, and $\sim 3000 \text{ cm}^{-3}$ over India (Ekman et al., 2012). Of course, there are elevated values in the UT at particular places and times over polluted continents, such as those reported by Twohy et al. (2002), but they appear to be more the exception than the rule. This vertical structure is quite close to being the exact opposite of the distribution measured over Amazonia during ACRIDICON-CHUVA, where the averages ($\pm \text{SD}$) were $7700 \pm 7970 \text{ cm}^{-3}$ in the UT and $1650 \pm 980 \text{ cm}^{-3}$ in the LT. Consequently, in the Anthropocene, the aerosol concentration profile has been turned upside down, at least in many polluted regions, since now the highest concentrations are found in the PBL.

This has important consequences for the Earth's climate system. The aerosol concentrations in the PBL influence cloud microphysical properties and radiative energy fluxes, which affect the characteristics of convection and thereby influence cloud radiative forcing, atmospheric stability, precipitation, and atmospheric dynamics at all scales (Jiang et al., 2008; Koren et al., 2008, 2010; Rosenfeld et al., 2008, 2014; Fan et al., 2012; Gonçalves et al., 2015; Stolz et al., 2015; Dagan et al., 2016; Braga et al., 2017). By their radiative and microphysical effects on convection dynamics, aerosols are also able to increase upper tropospheric humidity, which plays an important role in the Earth's radiation budget (Sherwood, 2002; Kottayil and Satheesan, 2015; Riuttanen et al., 2016) and may also affect the potential for aerosol nucleation in the UT, thus providing an additional feedback.

Data availability. The full data set from the ACRIDICON-CHUVA campaign is archived and publicly accessible from the HALO database maintained by the German Aerospace Center (DLR) at <https://halo-db.pa.op.dlr.de/mission/5>.

The Supplement related to this article is available online at <https://doi.org/10.5194/acp-18-921-2018-supplement>.

Competing interests. The authors declare that they have no conflict of interest.

Special issue statement. This article is part of the special issue "The ACRIDICON-CHUVA campaign to study deep convective clouds and precipitation over Amazonia using the new German HALO research aircraft (ACP/AMT inter-journal SI)". It does not belong to a conference.

Acknowledgements. We thank the entire ACRIDICON-CHUVA team for the great cooperation that made this study possible. Our thanks go especially to the HALO pilots, Steffen Gemsa, Michael Grossrubatscher, and Stefan Grillenbeck, who always worked hard to put the aircraft in the right place for our measurements, even under sometimes difficult conditions. We appreciate the support of the colleagues from enviroscope GmbH for their valuable help in certifying and installing the numerous instruments for HALO and thank the HALO team of the DLR for their cooperation. We acknowledge the generous support of the ACRIDICON-CHUVA campaign by the Max Planck Society, the German Aerospace Center (DLR), FAPESP (São Paulo Research Foundation), and the German Science Foundation (Deutsche Forschungsgemeinschaft, DFG) within the DFG Priority Program (SPP 1294) "Atmospheric and Earth System Research with the Research Aircraft HALO (High Altitude and Long Range Research Aircraft)" by contract nos. VO1504/4-1, SCHN1138/1-2, MI 583/4-1, JU 3059/1-1, WE 1900/22-1, WE 1900/24-1, and WE 1900/36-1. This study was also supported by EU Project HAIC under FP7-AAT-2012-3.5.1-1 and by the German Federal Ministry of Education and Research (BMBF, grant no. 01LG1205E). Christine Voigt acknowledges financing by the Helmholtz Association under contract no. W2/W3-60. Micael A. Cecchini was funded by FAPESP grant nos. 2014/08615-7 and 2014/21189-7. The participation of Daniel Rosenfeld was supported by project BACCHUS, European Commission FP7-603445. Bernadett Weinzierl, Maximilian Dollner, Daniel Sauer, and Adrian Walser received funding from the Helmholtz Association under grant VH-NG-606 (Helmholtz-Hochschul-Nachwuchsforschergruppe AerCARE) and from the European Research Council under the European Community's Horizon 2020 research and innovation framework program/ERC grant agreement 640458 (A-LIFE). Antonio Spanu was funded through the Marie Curie Initial Training Network VERTIGO (grant agreement no. 607905).

The article processing charges for this open-access publication were covered by the Max Planck Society.

Edited by: Anja Schmidt

Reviewed by: Hamish Gordon and two anonymous referees

References

- Abdelmonem, A., Järvinen, E., Duft, D., Hirst, E., Vogt, S., Leisner, T., and Schnaiter, M.: PHIPS–HALO: the airborne Particle Habit Imaging and Polar Scattering probe – Part 1: Design and operation: *Atmos. Meas. Tech.*, 9, 3131–3144, <https://doi.org/10.5194/amt-9-3131-2016>, 2016.
- Alfarra, M. R., Prevot, A. S. H., Szidat, S., Sandradewi, J., Weimer, S., Lanz, V. A., Schreiber, D., Mohr, M., and Baltensperger, U.: Identification of the mass spectral signature of organic aerosols from wood burning emissions, *Environ. Sci. Technol.*, 41, 5770–5777, <https://doi.org/10.1021/es062289b>, 2007.
- Andreae, M. O.: Correlation between cloud condensation nuclei concentration and aerosol optical thickness in remote and polluted regions, *Atmos. Chem. Phys.*, 9, 543–556, <https://doi.org/10.5194/acp-9-543-2009>, 2009.
- Andreae, M. O. and Andreae, T. W.: The cycle of biogenic sulfur compounds over the Amazon Basin. I. Dry season, *J. Geophys. Res.*, 93, 1487–1497, 1988.
- Andreae, M. O., Browell, E. V., Garstang, M., Gregory, G. L., Harriss, R. C., Hill, G. F., Jacob, D. J., Pereira, M. C., Sachse, G. W., Setzer, A. W., Dias, P. L. S., Talbot, R. W., Torres, A. L., and Wofsy, S. C.: Biomass-burning emissions and associated haze layers over Amazonia, *J. Geophys. Res.*, 93, 1509–1527, 1988.
- Andreae, M. O., Berresheim, H., Bingemer, H., Jacob, D. J., Lewis, B. L., Li, S.-M., and Talbot, R. W.: The atmospheric sulfur cycle over the Amazon Basin, 2. Wet Season, *J. Geophys. Res.*, 95, 16813–16824, 1990a.
- Andreae, M. O., Talbot, R. W., Berresheim, H., and Beecher, K. M.: Precipitation chemistry in central Amazonia, *J. Geophys. Res.*, 95, 16987–16999, 1990b.
- Andreae, M. O., Anderson, B. E., Blake, D. R., Bradshaw, J. D., Collins, J. E., Gregory, G. L., Sachse, G. W., and Shipham, M. C.: Influence of plumes from biomass burning on atmospheric chemistry over the equatorial Atlantic during CITE-3, *J. Geophys. Res.*, 99, 12793–12808, 1994.
- Andreae, M. O., Artaxo, P., Fischer, H., Freitas, S. R., Gregoire, J. M., Hansel, A., Hoor, P., Kormann, R., Krejci, R., Lange, L., Lelieveld, J., Lindinger, W., Longo, K., Peters, W., Reus, M. d., Scheeren, B., Silva Dias, M. A. F., Ström, J., van Velthoven, P. F. J., and Williams, J.: Transport of biomass burning smoke to the upper troposphere by deep convection in the equatorial region, *Geophys. Res. Lett.*, 28, 951–954, 2001.
- Andreae, M. O., Artaxo, P., Brandão, C., Carswell, F. E., Ciccioli, P., da Costa, A. L., Culf, A. D., Esteves, J. L., Gash, J. H. C., Grace, J., Kabat, P., Lelieveld, J., Malhi, Y., Manzi, A. O., Meixner, F. X., Nobre, A. D., Nobre, C., Ruivo, M. D. L. P., Silva-Dias, M. A., Stefani, P., Valentini, R., von Jouanne, J., and Waterloo, M. J.: Biogeochemical cycling of carbon, water, energy, trace gases and aerosols in Amazonia: The LBA-EUSTACH experiments, *J. Geophys. Res.*, 107, 8066, <https://doi.org/10.1029/2001JD000524>, 2002.
- Andreae, M. O., Rosenfeld, D., Artaxo, P., Costa, A. A., Frank, G. P., Longo, K. M., and Silva-Dias, M. A. F.: Smoking rain clouds over the Amazon, *Science*, 303, 1337–1342, 2004.
- Andreae, M. O., Artaxo, P., Beck, V., Bela, M., Freitas, S., Gerbig, C., Longo, K., Munger, J. W., Wiedemann, K. T., and Wofsy, S. C.: Carbon monoxide and related trace gases and aerosols over the Amazon Basin during the wet and dry seasons, *Atmos. Chem. Phys.*, 12, 6041–6065, <https://doi.org/10.5194/acp-12-6041-2012>, 2012.
- Andreae, M. O., Acevedo, O. C., Araújo, A., Artaxo, P., Barbosa, C. G. G., Barbosa, H. M. J., Brito, J., Carbone, S., Chi, X., Cintra, B. B. L., da Silva, N. F., Dias, N. L., Dias-Júnior, C. Q., Ditas, F., Ditz, R., Godoi, A. F. L., Godoi, R. H. M., Heimann, M., Hoffmann, T., Kesselmeier, J., Könemann, T., Krüger, M. L., Lavric, J. V., Manzi, A. O., Lopes, A. P., Martins, D. L., Mikhailov, E. F., Moran-Zuloaga, D., Nelson, B. W., Nölscher, A. C., Santos Nogueira, D., Piedade, M. T. F., Pöhlker, C., Pöschl, U., Quesada, C. A., Rizzo, L. V., Ro, C. U., Ruckteschler, N., Sá, L. D. A., de Oliveira Sá, M., Sales, C. B., dos Santos, R. M. N., Saturno, J., Schöngart, J., Sörgel, M., de Souza, C. M., de Souza, R. A. F., Su, H., Targhetta, N., Tóta, J., Trebs, I., Trumbore, S., van Eijck, A., Walter, D., Wang, Z., Weber, B., Williams, J., Winderlich, J., Wittmann, F., Wolff, S., and Yáñez-Serrano, A. M.: The Amazon Tall Tower Observatory (ATTO): overview of pilot measurements on ecosystem ecology, meteorology, trace gases, and aerosols, *Atmos. Chem. Phys.*, 15, 10723–10776, <https://doi.org/10.5194/acp-15-10723-2015>, 2015.
- Apel, E. C., Olson, J. R., Crawford, J. H., Hornbrook, R. S., Hills, A. J., Cantrell, C. A., Emmons, L. K., Knapp, D. J., Hall, S., Mauldin, R. L., Weinheimer, A. J., Fried, A., Blake, D. R., Crouse, J. D., St Clair, J. M., Wennberg, P. O., Diskin, G. S., Fuelberg, H. E., Wisthaler, A., Mikoviny, T., Brune, W., and Riemer, D. D.: Impact of the deep convection of isoprene and other reactive trace species on radicals and ozone in the upper troposphere, *Atmos. Chem. Phys.*, 12, 1135–1150, <https://doi.org/10.5194/acp-12-1135-2012>, 2012.
- Artaxo, P., Martins, J. V., Yamasoe, M. A., Procópio, A. S., Pauliquevis, T. M., Andreae, M. O., Guyon, P., Gatti, L. V., and Leal, A. M. C.: Physical and chemical properties of aerosols in the wet and dry season in Rondonia, Amazonia, *J. Geophys. Res.*, 107, 8081, <https://doi.org/10.1029/2001JD000666>, 2002.
- Artaxo, P., Rizzo, L. V., Brito, J. F., Barbosa, H. M. J., Arana, A., Sena, E. T., Cirino, G. G., Bastos, W., Martin, S. T., and Andreae, M. O.: Atmospheric aerosols in Amazonia and land use change: from natural biogenic to biomass burning conditions, *Faraday Discuss.*, 165, 203–235, <https://doi.org/10.1039/C3FD00052D>, 2013.
- Benson, D. R., Li-Hao Young, Shan-Hu Lee, Campos, T. L., Rogers, D. C., and Jensen, J.: The effects of airmass history on new particle formation in the free troposphere: case studies, *Atmos. Chem. Phys.*, 8, 3015–3024, <https://doi.org/10.5194/acp-8-3015-2008>, 2008.
- Berkemeier, T., Ammann, M., Mentel, T. F., Poschl, U., and Shiraiwa, M.: Organic nitrate contribution to new particle formation and growth in secondary organic aerosols from alpha-pinene ozonolysis, *Environ. Sci. Technol.*, 50, 6334–6342, <https://doi.org/10.1021/acs.est.6b00961>, 2016.
- Berndt, T., Richters, S., Jokinen, T., Hyttinen, N., Kurten, T., Otkjaer, R. V., Kjaergaard, H. G., Stratmann, F., Herrmann, H., Sipilä, M., Kulmala, M., and Ehn, M.: Hydroxyl radical-induced formation of highly oxidized organic compounds, *Nat. Commun.*, 7, 13677, <https://doi.org/10.1038/ncomms13677>, 2016.
- Bertram, T. H., Perring, A. E., Wooldridge, P. J., Crouse, J. D., Kwan, A. J., Wennberg, P. O., Scheuer, E., Dibb, J., Avery, M., Sachse, G., Vay, S. A., Crawford, J. H., McNaughton, C. S., Clarke, A., Pickering, K. E., Fuelberg, H., Huey, G., Blake, D.

- R., Singh, H. B., Hall, S. R., Shetter, R. E., Fried, A., Heikes, B. G., and Cohen, R. C.: Direct measurements of the convective recycling of the upper troposphere, *Science*, 315, 816–820, 2007.
- Betts, A. K., Gatti, L. V., Cordova, A. M., Dias, M. A. F. S., and Fuentes, J. D.: Transport of ozone to the surface by convective downdrafts at night, *J. Geophys. Res.*, 107, 8046, <https://doi.org/10.1029/2000JD000158>, 2002.
- Bianchi, F., Tröstl, J., Junninen, H., Frege, C., Henne, S., Hoyle, C. R., Molteni, U., Herrmann, E., Adamov, A., Bukowiecki, N., Chen, X., Duplissy, J., Gysel, M., Hutterli, M., Kangasluoma, J., Kontkanen, J., Kürten, A., Manninen, H. E., Münch, S., Peräkylä, O., Petäjä, T., Rondo, L., Williamson, C., Weingartner, E., Curtius, J., Worsnop, D. R., Kulmala, M., Dommen, J., and Baltensperger, U.: New particle formation in the free troposphere: A question of chemistry and timing, *Science*, 352, 1109–1112, <https://doi.org/10.1126/science.aad5456>, 2016.
- Borrmann, S., Kunkel, D., Weigel, R., Minikin, A., Deshler, T., Wilson, J. C., Curtius, J., Volk, C. M., Homan, C. D., Ulanovsky, A., Ravegnani, F., Viciani, S., Shur, G. N., Belyaev, G. V., Law, K. S., and Cairo, F.: Aerosols in the tropical and subtropical UT/LS: in-situ measurements of submicron particle abundance and volatility, *Atmos. Chem. Phys.*, 10, 5573–5592, <https://doi.org/10.5194/acp-10-5573-2010>, 2010.
- Braga, R. C., Rosenfeld, D., Weigel, R., Jurkat, T., Andreae, M. O., Wendisch, M., Pöschl, U., Voigt, C., Mahnke, C., Borrmann, S., Albrecht, R. I., Molleker, S., Vila, D. A., Machado, L. A. T., and Grulich, L.: Aerosol concentrations determine the height of warm rain and ice initiation in convective clouds over the Amazon basin, *Atmos. Chem. Phys. Discuss.*, in review, <https://doi.org/10.5194/acp-2016-1155>, 2017.
- Brock, C. A., Hamill, P., Wilson, J. C., Jonsson, H. H., and Chan, K. R.: Particle formation in the upper tropical troposphere – a source of nuclei for the stratospheric aerosol: *Science*, 270, 1650–1653, <https://doi.org/10.1126/science.270.5242.1650>, 1995.
- Brock, C. A., Cozic, J., Bahreini, R., Froyd, K. D., Middlebrook, A. M., McComiskey, A., Brioude, J., Cooper, O. R., Stohl, A., Aikin, K. C., de Gouw, J. A., Fahey, D. W., Ferrare, R. A., Gao, R. S., Gore, W., Holloway, J. S., Hubler, G., Jefferson, A., Lack, D. A., Lance, S., Moore, R. H., Murphy, D. M., Nenes, A., Novelli, P. C., Nowak, J. B., Ogren, J. A., Peischl, J., Pierce, R. B., Pilewskie, P., Quinn, P. K., Ryerson, T. B., Schmidt, K. S., Schwarz, J. P., Sodemann, H., Spackman, J. R., Stark, H., Thomson, D. S., Thornberry, T., Veres, P., Watts, L. A., Warneke, C., and Wollny, A. G.: Characteristics, sources, and transport of aerosols measured in spring 2008 during the aerosol, radiation, and cloud processes affecting Arctic Climate (ARCPAC) Project, *Atmos. Chem. Phys.*, 11, 2423–2453, <https://doi.org/10.5194/acp-11-2423-2011>, 2011.
- Browell, E. V., Fenn, M. A., Butler, C. F., Grant, W. B., Clayton, M. E., Fishman, J., Bachmeier, A. S., Anderson, B. E., Gregory, G. L., Fuelberg, H. E., Bradshaw, J. D., Sandholm, S. T., Blake, D. R., Heikes, B. G., Sachse, G. W., Singh, H. B., and Talbot, R. W.: Ozone and aerosol distributions and air mass characteristics over the South Atlantic basin during the burning season, *J. Geophys. Res.*, 101, 24043–24068, 1996.
- Bruns, E. A., Perraud, V., Zelenyuk, A., Ezell, M. J., Johnson, S. N., Yu, Y., Imre, D., Finlayson-Pitts, B. J., and Alexander, M. L.: Comparison of FTIR and particle mass spectrometry for the measurement of particulate organic nitrates, *Environ. Sci. Technol.*, 44, 1056–1061, <https://doi.org/10.1021/es9029864>, 2010.
- Cai, Y., Montague, D. C., Mooiweer-Bryan, W., and Deshler, T.: Performance characteristics of the ultra high sensitivity aerosol spectrometer for particles between 55 and 800 nm: Laboratory and field studies, *J. Aerosol Sci.*, 39, 759–769, <https://doi.org/10.1016/j.jaerosci.2008.04.007>, 2008.
- Carslaw, K. S., Lee, L. A., Reddington, C. L., Pringle, K. J., Rap, A., Forster, P. M., Mann, G. W., Spracklen, D. V., Woodhouse, M. T., Regayre, L. A., and Pierce, J. R.: Large contribution of natural aerosols to uncertainty in indirect forcing, *Nature*, 503, 67–71, <https://doi.org/10.1038/nature12674>, 2013.
- Carslaw, K. S., Gordon, H., Hamilton, D. S., Johnson, J. S., Regayre, L. A., Yoshioka, M., and Pringle, K. J.: Aerosols in the pre-industrial atmosphere, *Curr. Clim. Change Rep.*, 3, 1–15, <https://doi.org/10.1007/s40641-017-0061-2>, 2017.
- Cecchini, M. A., Machado, L. A. T., Andreae, M. O., Martin, S. T., Albrecht, R. I., Artaxo, P., Barbosa, H. M. J., Borrmann, S., Fütterer, D., Jurkat, T., Mahnke, C., Minikin, A., Molleker, S., Pöhlker, M. L., Pöschl, U., Rosenfeld, D., Voigt, C., Weinzierl, B., and Wendisch, M.: Sensitivities of Amazonian clouds to aerosols and updraft speed, *Atmos. Chem. Phys.*, 17, 10037–10050, <https://doi.org/10.5194/acp-17-10037-2017>, 2017.
- Chubb, T., Huang, Y., Jensen, J., Campos, T., Siems, S., and Manton, M.: Observations of high droplet number concentrations in Southern Ocean boundary layer clouds, *Atmos. Chem. Phys.*, 16, 971–987, <https://doi.org/10.5194/acp-16-971-2016>, 2016.
- Clarke, A. and Kapustin, V.: Hemispheric aerosol vertical profiles: Anthropogenic impacts on optical depth and cloud nuclei, *Science*, 329, 1488–1492, 2010.
- Clarke, A. D.: Atmospheric nuclei in the remote free troposphere, *J. Atmos. Chem.*, 14, 479–488, <https://doi.org/10.1007/bf00115252>, 1992.
- Clarke, A. D.: Atmospheric nuclei in the Pacific midtroposphere – their nature, concentration, and evolution, *J. Geophys. Res.*, 98, 20633–20647, <https://doi.org/10.1029/93jd00797>, 1993.
- Clarke, A. D. and Kapustin, V. N.: A Pacific aerosol survey. Part I: A decade of data on particle production, transport, evolution, and mixing in the troposphere, *J. Atmos. Sci.*, 59, 363–382, 2002.
- Clarke, A. D., Varner, J. L., Eisele, F., Mauldin, R. L., Tanner, D., and Litchy, M.: Particle production in the remote marine atmosphere: Cloud outflow and subsidence during ACE 1, *J. Geophys. Res.*, 103, 16397–16409, <https://doi.org/10.1029/97jd02987>, 1998.
- Clarke, A. D., Eisele, F., Kapustin, V. N., Moore, K., Tanner, D., Mauldin, L., Litchy, M., Lienert, B., Carroll, M. A., and Albrecht, G.: Nucleation in the equatorial free troposphere: Favorable environments during PEM-Tropics, *J. Geophys. Res.*, 104, 5735–5744, <https://doi.org/10.1029/98JD02303>, 1999.
- Clarke, A. D., Freitag, S., Simpson, R. M. C., Hudson, J. G., Howell, S. G., Brekhovskikh, V. L., Campos, T., Kapustin, V. N., and Zhou, J.: Free troposphere as a major source of CCN for the Equatorial Pacific boundary layer: long-range transport and teleconnections, *Atmos. Chem. Phys.*, 13, 7511–7529, <https://doi.org/10.5194/acp-13-7511-2013>, 2013.
- Collow, A. B. M., Miller, M. A., and Trabachino, L. C.: Cloudiness over the Amazon rainforest: Meteorology and thermodynamics, *J. Geophys. Res.*, 121, 7990–8005, <https://doi.org/10.1002/2016JD024848>, 2016.

- Colomb, A., Williams, J., Crowley, J., Gros, V., Hofmann, R., Salisbury, G., Klupfel, T., Kormann, R., Stickler, A., Forster, C., and Lelieveld, J.: Airborne measurements of trace organic species in the upper troposphere over Europe: the impact of deep convection, *Environ. Chem.*, 3, 244–259, <https://doi.org/10.1071/en06020>, 2006.
- Cubison, M. J., Ortega, A. M., Hayes, P. L., Farmer, D. K., Day, D., Lechner, M. J., Brune, W. H., Apel, E., Diskin, G. S., Fisher, J. A., Fuelberg, H. E., Hecobian, A., Knapp, D. J., Mikoviny, T., Riemer, D., Sachse, G. W., Sessions, W., Weber, R. J., Weinheimer, A. J., Wisthaler, A., and Jimenez, J. L.: Effects of aging on organic aerosol from open biomass burning smoke in aircraft and laboratory studies, *Atmos. Chem. Phys.*, 11, 12049–12064, <https://doi.org/10.5194/acp-11-12049-2011>.
- Dagan, G., Koren, I., Altaratz, O., and Heiblum, R. H.: Aerosol effect on the evolution of the thermodynamic properties of warm convective cloud fields, *Scient. Rep.*, 6, 38769, <https://doi.org/10.1038/srep38769>, 2016.
- de Reus, M., Krejci, R., Williams, J., Fischer, H., Scheele, R., and Strom, J.: Vertical and horizontal distributions of the aerosol number concentration and size distribution over the northern Indian Ocean, *J. Geophys. Res.*, 106, 28629–28641, 2001.
- Drewnick, F., Hings, S. S., DeCarlo, P., Jayne, J. T., Gonin, M., Fuhrer, K., Weimer, S., Jimenez, J. L., Demerjian, K. L., Borrmann, S., and Worsnop, D. R.: A new time-of-flight aerosol mass spectrometer (TOF-AMS) – Instrument description and first field deployment, *Aerosol Sci. Tech.*, 39, 637–658, 2005.
- Dunne, E. M., Gordon, H., Kürten, A., Almeida, J., Duplissy, J., Williamson, C., Ortega, I. K., Pringle, K. J., Adamov, A., Baltensperger, U., Barmet, P., Benduhn, F., Bianchi, F., Breitenlechner, M., Clarke, A., Curtius, J., Dommen, J., Donahue, N. M., Ehrhart, S., Flagan, R. C., Franchin, A., Guida, R., Hakala, J., Hansel, A., Heinritzi, M., Jokinen, T., Kangasluoma, J., Kirkby, J., Kulmala, M., Kupc, A., Lawler, M. J., Lehtipalo, K., Makhmutov, V., Mann, G., Mathot, S., Merikanto, J., Miettinen, P., Nenes, A., Onnela, A., Rap, A., Reddington, C. L. S., Riccobono, F., Richards, N. A. D., Rissanen, M. P., Rondo, L., Sarnela, N., Schobesberger, S., Sengupta, K., Simon, M., Sipilä, M., Smith, J. N., Stozkhov, Y., Tomé, A., Tröstl, J., Wagner, P. E., Wimmer, D., Winkler, P. M., Worsnop, D. R., and Carslaw, K. S.: Global atmospheric particle formation from CERN CLOUD measurements, *Science*, 354, 1119–1124, <https://doi.org/10.1126/science.aaf2649>, 2016.
- Ehn, M., Thornton, J. A., Kleist, E., Sipila, M., Junninen, H., Pullinen, I., Springer, M., Rubach, F., Tillmann, R., Lee, B., Lopez-Hilfiker, F., Andres, S., Acir, I. H., Rissanen, M., Jokinen, T., Schobesberger, S., Kangasluoma, J., Kontkanen, J., Nieminen, T., Kurten, T., Nielsen, L. B., Jorgensen, S., Kjaergaard, H. G., Canagaratna, M., Dal Maso, M., Berndt, T., Petaja, T., Wahner, A., Kerminen, V. M., Kulmala, M., Worsnop, D. R., Wildt, J., and Mentel, T. F.: A large source of low-volatility secondary organic aerosol, *Nature*, 506, 476–479, <https://doi.org/10.1038/nature13032>, 2014.
- Ekman, A. M. L., Wang, C., Strom, J., and Krejci, R.: Explicit simulation of aerosol physics in a cloud-resolving model: Aerosol transport and processing in the free troposphere, *J. Atmos. Sci.*, 63, 682–696, 2006.
- Ekman, A. M. L., Krejci, R., Engström, A., Ström, J., de Reus, M., Williams, J., and Andreae, M. O.: Do organics contribute to small particle formation in the Amazonian upper troposphere?, *Geophys. Res. Lett.*, 35, L17810, <https://doi.org/10.1029/2008GL034970>, 2008.
- Ekman, A. M. L., Hermann, M., Gross, P., Heintzenberg, J., Kim, D., and Wang, C.: Sub-micrometer aerosol particles in the upper troposphere/lowermost stratosphere as measured by CARIBIC and modeled using the MIT-CAM3 global climate model, *J. Geophys. Res.*, 117, D11202, <https://doi.org/10.1029/2011jd016777>, 2012.
- Engelhart, G. J., Asa-Awuku, A., Nenes, A., and Pandis, S. N.: CCN activity and droplet growth kinetics of fresh and aged monoterpene secondary organic aerosol, *Atmos. Chem. Phys.*, 8, 3937–3949, <https://doi.org/10.5194/acp-8-3937-2008>, 2008.
- Engelhart, G. J., Moore, R. H., Nenes, A., and Pandis, S. N.: Cloud condensation nuclei activity of isoprene secondary organic aerosol, *J. Geophys. Res.*, 116, D02207, <https://doi.org/10.1029/2010jd014706>, 2011.
- Engström, A., Ekman, A. M. L., Krejci, R., Strom, J., de Reus, M., and Wang, C.: Observational and modelling evidence of tropical deep convective clouds as a source of mid-tropospheric accumulation mode aerosols, *Geophys. Res. Lett.*, 35, L23813, <https://doi.org/10.1029/2008gl035817>, 2008.
- Fan, J. W., Rosenfeld, D., Ding, Y. N., Leung, L. R., and Li, Z. Q.: Potential aerosol indirect effects on atmospheric circulation and radiative forcing through deep convection, *Geophys. Res. Lett.*, 39, L09806, <https://doi.org/10.1029/2012gl051851>, 2012.
- Fishman, J., Fakhruzzaman, K., Cros, B., and Nganga, D.: Identification of widespread pollution in the southern hemisphere deduced from satellite analyses, *Science*, 252, 1693–1696, 1991.
- Fishman, J., Brackett, V. G., Browell, E. V., and Grant, W. B.: Tropospheric ozone derived from TOMS/SBUV measurements during TRACE-A, *J. Geophys. Res.*, 101, 24069–24082, 1996.
- Frey, W., Borrmann, S., Kunkel, D., Weigel, R., de Reus, M., Schlager, H., Roiger, A., Voigt, C., Hoor, P., Curtius, J., Kraemer, M., Schiller, C., Volk, C. M., Homan, C. D., Fierli, F., Di Donfrancesco, G., Ulanovsky, A., Ravegnani, F., Sitnikov, N. M., Viciani, S., D'Amato, F., Shur, G. N., Belyaev, G. V., Law, K. S., and Cairo, F.: In situ measurements of tropical cloud properties in the West African Monsoon: upper tropospheric ice clouds, Mesoscale Convective System outflow, and subvisual cirrus, *Atmos. Chem. Phys.*, 11, 5569–5590, <https://doi.org/10.5194/acp-11-5569-2011>, 2011.
- Froyd, K. D., Murphy, D. M., Sanford, T. J., Thomson, D. S., Wilson, J. C., Pfister, L., and Lait, L.: Aerosol composition of the tropical upper troposphere, *Atmos. Chem. Phys.*, 9, 4363–4385, <https://doi.org/10.5194/acp-9-4363-2009>, 2009.
- Fry, J. L., Kiendler-Scharr, A., Rollins, A. W., Wooldridge, P. J., Brown, S. S., Fuchs, H., Dubé, W., Mensah, A., dal Maso, M., Tillmann, R., Dorn, H.-P., Brauers, T., and Cohen, R. C.: Organic nitrate and secondary organic aerosol yield from NO₃ oxidation of β -pinene evaluated using a gas-phase kinetics/aerosol partitioning model, *Atmos. Chem. Phys.*, 9, 1431–1449, <https://doi.org/10.5194/acp-9-1431-2009>, 2009.
- Fu, R., Zhu, B., and Dickinson, R. E.: How do atmosphere and land surface influence seasonal changes of convection in the tropical Amazon, *J. Climate*, 12, 1306–1321, 1999.
- Fueglistaler, S., Dessler, A. E., Dunkerton, T. J., Folkens, I., Fu, Q., and Mote, P. W.: Tropical tropopause layer, *Rev. Geophys.*, 47, RG1004, <https://doi.org/10.1029/2008rg000267>, 2009.

- Gerbig, C., Schmitgen, S., Kley, D., Volz-Thomas, A., Dewey, K., and Haaks, D.: An improved fast-response vacuum-UV resonance fluorescence CO instrument, *J. Geophys. Res.*, 104, 1699–1704, <https://doi.org/10.1029/1998jd100031>, 1999.
- Gerken, T., Wei, D., Chase, R. J., Fuentes, J. D., Schumacher, C., Machado, L. A. T., Andreoli, R. V., Chamecki, M., Ferreira de Souza, R. A., Freire, L. S., Jardine, A. B., Manzi, A. O., Nascimento dos Santos, R. M., von Randow, C., dos Santos Costa, P., Stoy, P. C., Tóta, J., and Trowbridge, A. M.: Downward transport of ozone rich air and implications for atmospheric chemistry in the Amazon rainforest, *Atmos. Environ.*, 124, 64–76, <https://doi.org/10.1016/j.atmosenv.2015.11.014>, 2016.
- Giangrande, S. E., Feng, Z., Jensen, M. P., Comstock, J. M., Johnson, K. L., Toto, T., Wang, M., Burleyson, C., Bharadwaj, N., Mei, F., Machado, L. A. T., Manzi, A. O., Xie, S., Tang, S., Silva Dias, M. A. F., de Souza, R. A. F., Schumacher, C., and Martin, S. T.: Cloud characteristics, thermodynamic controls and radiative impacts during the Observations and Modeling of the Green Ocean Amazon (GoAmazon2014/5) experiment, *Atmos. Chem. Phys.*, 17, 14519–14541, <https://doi.org/10.5194/acp-17-14519-2017>, 2017.
- Gonçalves, W. A., Machado, L. A. T., and Kirstetter, P. E.: Influence of biomass aerosol on precipitation over the Central Amazon: an observational study, *Atmos. Chem. Phys.*, 15, 6789–6800, <https://doi.org/10.5194/acp-15-6789-2015>, 2015.
- Gordon, H., Sengupta, K., Rap, A., Duplissy, J., Frege, C., Williamson, C., Heinritzi, M., Simon, M., Yan, C., Almeida, J., Tröstl, J., Nieminen, T., Ortega, I. K., Wagner, R., Dunne, E. M., Adamov, A., Amorim, A., Bernhammer, A.-K., Bianchi, F., Breitenlechner, M., Brilke, S., Chen, X., Craven, J. S., Dias, A., Ehrhart, S., Fischer, L., Flagan, R. C., Franchin, A., Fuchs, C., Guida, R., Hakala, J., Hoyle, C. R., Jokinen, T., Junninen, H., Kangasluoma, J., Kim, J., Kirkby, J., Krapf, M., Kürten, A., Laaksonen, A., Lehtipalo, K., Makhmutov, V., Mathot, S., Molteni, U., Monks, S. A., Onnela, A., Peräkylä, O., Piel, F., Petäjä, T., Praplan, A. P., Pringle, K. J., Richards, N. A. D., Rissanen, M. P., Rondo, L., Sarnela, N., Schobesberger, S., Scott, C. E., Seinfeld, J. H., Sharma, S., Sipilä, M., Steiner, G., Stozhkov, Y., Stratmann, F., Tomé, A., Virtanen, A., Vogel, A. L., Wagner, A. C., Wagner, P. E., Weingartner, E., Wimmer, D., Winkler, P. M., Ye, P., Zhang, X., Hansel, A., Dommen, J., Donahue, N. M., Worsnop, D. R., Baltensperger, U., Kulmala, M., Curtius, J., and Carslaw, K. S.: Reduced anthropogenic aerosol radiative forcing caused by biogenic new particle formation, *P. Natl. Acad. Sci. USA*, 113, 12053–12058, <https://doi.org/10.1073/pnas.1602360113>, 2016.
- Grant, D. D., Fuentes, J. D., DeLonge, M. S., Chan, S., Joseph, E., Kucera, P., Ndiaye, S. A., and Gaye, A. T.: Ozone transport by mesoscale convective storms in western Senegal, *Atmos. Environ.*, 42, 7104–7114, <https://doi.org/10.1016/j.atmosenv.2008.05.044>, 2008.
- Gunthe, S. S., King, S. M., Rose, D., Chen, Q., Roldin, P., Farmer, D. K., Jimenez, J. L., Artaxo, P., Andreae, M. O., Martin, S. T., and Pöschl, U.: Cloud condensation nuclei in pristine tropical rainforest air of Amazonia: size-resolved measurements and modeling of atmospheric aerosol composition and CCN activity, *Atmos. Chem. Phys.*, 9, 7551–7575, <https://doi.org/10.5194/acp-9-7551-2009>, 2009.
- Heald, C. L., Jacob, D. J., Park, R. J., Russell, L. M., Huebert, B. J., Seinfeld, J. H., Liao, H., and Weber, R. J.: A large organic aerosol source in the free troposphere missing from current models, *Geophys. Res. Lett.*, 32, L18809, <https://doi.org/10.1029/2005GL023831>, 2005.
- Heintzenberg, J., Birmili, W., Otto, R., Andreae, M. O., Mayer, J.-C., Chi, X., and Panov, A.: Aerosol particle number size distributions and particulate light absorption at the ZOTTO tall tower (Siberia), 2006–2009, *Atmos. Chem. Phys.*, 11, 8703–8719, <https://doi.org/10.5194/acp-11-8703-2011>, 2011.
- Holanda, B. A., Wang, Q., Saturno, J., Ditas, F., Ditas, J., Pöhlker, M., Klimach, T., Moran, D., Schulz, C., Ming, J., Cheng, Y., Su, H., Wendisch, M., Machado, L. A. T., Schneider, J., Pöhlker, C., Artaxo, P., Pöschl, U., and Andreae, M.: Transatlantic transport of pollution aerosol from Africa to the Amazon rain forest – Aircraft observations in the context of the ACRIDICON-CHUVA campaign, *Atmos. Chem. Phys. Discuss.*, in preparation, 2018.
- Hu, W. W., Campuzano-Jost, P., Palm, B. B., Day, D. A., Ortega, A. M., Hayes, P. L., Krechmer, J. E., Chen, Q., Kuwata, M., Liu, Y. J., de Sa, S. S., McKinney, K., Martin, S. T., Hu, M., Budisulistiorini, S. H., Riva, M., Surratt, J. D., St Clair, J. M., Isaacman-Van Wertz, G., Yee, L. D., Goldstein, A. H., Carbone, S., Brito, J., Artaxo, P., de Gouw, J. A., Koss, A., Wisthaler, A., Mikoviny, T., Karl, T., Kaser, L., Jud, W., Hansel, A., Docherty, K. S., Alexander, M. L., Robinson, N. H., Coe, H., Allan, J. D., Canagaratna, M. R., Paulot, F., and Jimenez, J. L.: Characterization of a real-time tracer for isoprene epoxydiols-derived secondary organic aerosol (IEPOX-SOA) from aerosol mass spectrometer measurements, *Atmos. Chem. Phys.*, 15, 11807–11833, <https://doi.org/10.5194/acp-15-11807-2015>, 2015.
- Hu, X. M., Fuentes, J. D., and Zhang, F. Q.: Downward transport and modification of tropospheric ozone through moist convection, *J. Atmos. Chem.*, 65, 13–35, <https://doi.org/10.1007/s10874-010-9179-5>, 2010.
- Huntrieser, H., Lichtenstern, M., Scheibe, M., Aufmhoff, H., Schlager, H., Pucik, T., Minikin, A., Weinzierl, B., Heimerl, K., Futterer, D., Rappengluck, B., Ackermann, L., Pickering, K. E., Cummings, K. A., Biggerstaff, M. I., Betten, D. P., Honomichl, S., and Barth, M. C.: On the origin of pronounced O₃ gradients in the thunderstorm outflow region during DC3, *J. Geophys. Res.*, 121, 6600–6637, <https://doi.org/10.1002/2015jd024279>, 2016.
- Janhäll, S., Andreae, M. O., and Pöschl, U.: Biomass burning aerosol emissions from vegetation fires: particle number and mass emission factors and size distributions, *Atmos. Chem. Phys.*, 10, 1427–1439, <https://doi.org/10.5194/acp-10-1427-2010>, 2010.
- Jiang, J. H., Su, H., Schoeberl, M. R., Massie, S. T., Colarco, P., Platnick, S., and Livesey, N. J.: Clean and polluted clouds: Relationships among pollution, ice clouds, and precipitation in South America, *Geophys. Res. Lett.*, 35, L14804, <https://doi.org/10.1029/2008GL034631>, 2008.
- Jimenez, J. L., Canagaratna, M. R., Donahue, N. M., Prevot, A. S. H., Zhang, Q., Kröll, J. H., DeCarlo, P. F., Allan, J. D., Coe, H., Ng, N. L., Aiken, A. C., Docherty, K. D., Ulbrich, I. M., Grieshop, A. P., Robinson, A. L., Duplissy, J., Smith, J. D., Wilson, K. R., Lanz, V. A., Hueglin, C., Sun, Y. L., Tian, J., Laaksonen, A., Raatikainen, T., Rautiainen, J., Vaattovaara, P., Ehn, M., Kulmala, M., Tomlinson, J. M., Collins, D. R., Cubison, M. J., Dunlea, E. J., Huffman, J. A., Onasch, T. B., Al-

- farra, M. R., Williams, P. I., Bower, K., Kondo, Y., Schneider, J., Drewnick, F., Borrmann, S., Weimer, S., Demerjian, K., Salcedo, D., Cottrell, L., Griffin, R., Takami, A., Miyoshi, T., Hatakeyama, S., Shimono, A., Sun, J. Y., Zhang, Y. M., Dzepina, K., Kimmel, J. R., Sueper, D., Jayne, J. T., Herndon, S. C., Trimborn, A. M., Williams, L. R., Wood, E. C., Kolb, C. E., Baltensperger, U., and Worsnop, D. R.: Evolution of organic aerosols in the atmosphere, *Science*, 326, 1525–1529, <https://doi.org/10.1126/science.1180353>, 2009.
- Jokinen, T., Berndt, T., Makkonen, R., Kerminen, V.-M., Junninen, H., Paasonen, P., Stratmann, F., Herrmann, H., Guenther, A. B., Worsnop, D. R., Kulmala, M., Ehn, M., and Sipilä, M.: Production of extremely low volatile organic compounds from biogenic emissions: Measured yields and atmospheric implications, *P. Natl. Acad. Sci. USA*, 112, 7123–7128, <https://doi.org/10.1073/pnas.1423977112>, 2015.
- Katoshevski, D., Nenes, A., and Seinfeld, J. H.: A study of processes that govern the maintenance of aerosols in the marine boundary layer, *J. Aerosol Sci.*, 30, 503–532, 1999.
- Khain, A. P., Phillips, V., Benmoshe, N., and Pokrovsky, A.: The role of small soluble aerosols in the microphysics of deep maritime clouds, *J. Atmos. Sci.*, 69, 2787–2807, <https://doi.org/10.1175/2011jas3649.1>, 2012.
- Kirkby, J., Duplissy, J., Sengupta, K., Frege, C., Gordon, H., Williamson, C., Heinritzi, M., Simon, M., Yan, C., Almeida, J., Tröstl, J., Nieminen, T., Ortega, I. K., Wagner, R., Adamov, A., Amorim, A., Bernhammer, A.-K., Bianchi, F., Breitenlechner, M., Brilke, S., Chen, X., Craven, J., Dias, A., Ehrhart, S., Flagan, R. C., Franchin, A., Fuchs, C., Guida, R., Hakala, J., Hoyle, C. R., Jokinen, T., Junninen, H., Kangasluoma, J., Kim, J., Krapf, M., Kürten, A., Laaksonen, A., Lehtipalo, K., Makhmutov, V., Mathot, S., Molteni, U., Onnela, A., Peräkylä, O., Piel, F., Petäjä, T., Praplan, A. P., Pringle, K., Rap, A., Richards, N. A. D., Riipinen, I., Rissanen, M. P., Rondo, L., Sarnela, N., Schobesberger, S., Scott, C. E., Seinfeld, J. H., Sipilä, M., Steiner, G., Stozhkov, Y., Stratmann, F., Tomé, A., Virtanen, A., Vogel, A. L., Wagner, A. C., Wagner, P. E., Weingartner, E., Wimmer, D., Winkler, P. M., Ye, P., Zhang, X., Hansel, A., Dommen, J., Donahue, N. M., Worsnop, D. R., Baltensperger, U., Kulmala, M., Carslaw, K. S., and Curtius, J.: Ion-induced nucleation of pure biogenic particles, *Nature*, 533, 521–526, <https://doi.org/10.1038/nature17953>, 2016.
- Kojima, T., Buseck, P. R., Wilson, J. C., Reeves, J. M., and Mahoney, M. J.: Aerosol particles from tropical convective systems: Cloud tops and cirrus anvils, *J. Geophys. Res.*, 109, D12201, <https://doi.org/doi:10.1029/2003JD004504>, 2004.
- Koren, I., Martins, J. V., Remer, L. A., and Afargan, H.: Smoke invigoration versus inhibition of clouds over the Amazon, *Science*, 321, 946–949, 2008.
- Koren, I., Remer, L. A., Altaratz, O., Martins, J. V., and Davidi, A.: Aerosol-induced changes of convective cloud anvils produce strong climate warming, *Atmos. Chem. Phys.*, 10, 5001–5010, <https://doi.org/10.5194/acp-10-5001-2010>, 2010.
- Kottayil, A. and Satheesan, K.: Enhancement in the upper tropospheric humidity associated with aerosol loading over tropical Pacific, *Atmos. Environ.*, 122, 148–153, <https://doi.org/10.1016/j.atmosenv.2015.09.043>, 2015.
- Krejci, R., Strom, J., de Reus, M., Hoor, P., Williams, J., Fischer, H., and Hansson, H. C.: Evolution of aerosol properties over the rain forest in Surinam, South America, observed from aircraft during the LBA-CLAIRE 98 experiment, *J. Geophys. Res.*, 108, 4561, <https://doi.org/10.1029/2001JD001375>, 2003.
- Krüger, M. L., Mertes, S., Klimach, T., Cheng, Y., Su, H., Schneider, J., Andreae, M. O., Pöschl, U., and Rose, D.: Assessment of cloud supersaturation by size-resolved aerosol particle and cloud condensation nuclei (CCN) measurements, *Atmos. Meas. Tech.*, 7, 2615–2629, <https://doi.org/10.5194/amt-7-2615-2014>, 2014.
- Kulmala, M. and Kerminen, V. M.: On the formation and growth of atmospheric nanoparticles, *Atmos. Res.*, 90, 132–150, <https://doi.org/10.1016/j.atmosres.2008.01.005>, 2008.
- Kulmala, M., Reissell, A., Sipilä, M., Bonn, B., Ruuskanen, T. M., Lehtinen, K. E. J., Kerminen, V.-M., and Strom, J.: Deep convective clouds as aerosol production engines: Role of insoluble organics, *J. Geophys. Res.*, 111, D17202, <https://doi.org/10.1029/2005jd006963>, 2006.
- Laaksonen, A., Kulmala, M., O'Dowd, C. D., Joutsensaari, J., Vaattovaara, P., Mikkonen, S., Lehtinen, K. E. J., Sogacheva, L., Dal Maso, M., Aalto, P., Petäjä, T., Sogachev, A., Yoon, Y. J., Lihavainen, H., Nilsson, D., Facchini, M. C., Cavalli, F., Fuzzi, S., Hoffmann, T., Arnold, F., Hanke, M., Sellegri, K., Umann, B., Junkermann, W., Coe, H., Allan, J. D., Alfarra, M. R., Worsnop, D. R., Riekkola, M.-L., Hyötyläinen, T., and Visanen, Y.: The role of VOC oxidation products in continental new particle formation, *Atmos. Chem. Phys.*, 8, 2657–2665, <https://doi.org/10.5194/acp-8-2657-2008>, 2008.
- Laborde, M., Crippa, M., Tritscher, T., Juranyi, Z., Decarlo, P. F., Temime-Roussel, B., Marchand, N., Eckhardt, S., Stohl, A., Baltensperger, U., Prevot, A. S. H., Weingartner, E., and Gysel, M.: Black carbon physical properties and mixing state in the European megacity Paris, *Atmos. Chem. Phys.*, 13, 5831–5856, <https://doi.org/10.5194/acp-13-5831-2013>, 2013.
- Lee, L., Wooldridge, P. J., Gilman, J. B., Warneke, C., de Gouw, J., and Cohen, R. C.: Low temperatures enhance organic nitrate formation: evidence from observations in the 2012 Uintah Basin Winter Ozone Study, *Atmos. Chem. Phys.*, 14, 12441–12454, <https://doi.org/10.5194/acp-14-12441-2014>, 2014.
- Lee, S. H., Reeves, J. M., Wilson, J. C., Hunton, D. E., Viggiano, A. A., Miller, T. M., Ballenthin, J. O., and Lait, L. R.: Particle formation by ion nucleation in the upper troposphere and lower stratosphere: *Science*, 301, 1886–1889, <https://doi.org/10.1126/science.1087236>, 2003.
- Lee, S. H., Wilson, J. C., Baumgardner, D., Herman, R. L., Weinstock, E. M., LaFleur, B. G., Kok, G., Anderson, B., Lawson, P., Baker, B., Strawa, A., Pittman, J. V., Reeves, J. M., and Bui, T. P.: New particle formation observed in the tropical/subtropical cirrus clouds, *J. Geophys. Res.*, 109, D20209, <https://doi.org/10.1029/2004jd005033>, 2004.
- Machado, L. A. T., Laurent, H., Dessay, N., and Miranda, I.: Seasonal and diurnal variability of convection over the Amazonia: A comparison of different vegetation types and large scale forcing, *Theor. Appl. Climatol.*, 78, 61–77, <https://doi.org/10.1007/s00704-004-0044-9>, 2004.
- Martin, S. T., Andreae, M. O., Artaxo, P., Baumgardner, D., Chen, Q., Goldstein, A. H., Guenther, A., Heald, C. L., Mayol-Bracero, O. L., McMurry, P. H., Pauliquevis, T., Pöschl, U., Prather, K. A., Roberts, G. C., Saleska, S. R., Dias, M. A. S., Spracklen, D., Swietlicki, E., and Trebs, I.: Sources and proper-

- ties of Amazonian aerosol particles, *Rev. Geophys.*, 48, RG2002, <https://doi.org/10.1029/2008RG000280>, 2010.
- Martin, S. T., Artaxo, P., Machado, L. A. T., Manzi, A. O., Souza, R. A. F., Schumacher, C., Wang, J., Andreae, M. O., Barbosa, H. M. J., Fan, J., Fisch, G., Goldstein, A. H., Guenther, A., Jimenez, J. L., Pöschl, U., Silva Dias, M. A., Smith, J. N., and Wendisch, M.: Introduction: Observations and modeling of the Green Ocean Amazon (GoAmazon2014/5), *Atmos. Chem. Phys.*, 16, 4785–4797, <https://doi.org/10.5194/acp-16-4785-2016>, 2016.
- Merikanto, J., Spracklen, D. V., Mann, G. W., Pickering, S. J., and Carslaw, K. S.: Impact of nucleation on global CCN, *Atmos. Chem. Phys.*, 9, 8601–8616, <https://doi.org/10.5194/acp-9-8601-2009>, 2009.
- Metzger, A., Verheggen, B., Dommen, J., Duplissy, J., Prevot, A. S. H., Weingartner, E., Riipinen, I., Kulmala, M., Spracklen, D. V., Carslaw, K. S., and Baltensperger, U.: Evidence for the role of organics in aerosol particle formation under atmospheric conditions, *P. Natl. Acad. Sci. USA*, 107, 6646–6651, <https://doi.org/10.1073/pnas.0911330107>, 2010.
- Mirme, S., Mirme, A., Minikin, A., Petzold, A., Hörrak, U., Kerminen, V.-M., and Kulmala, M.: Atmospheric sub-3 nm particles at high altitudes, *Atmos. Chem. Phys.*, 10, 437–451, <https://doi.org/10.5194/acp-10-437-2010>, 2010.
- Murphy, B. N., Julin, J., Riipinen, I., and Ekman, A. M. L.: Organic aerosol processing in tropical deep convective clouds: Development of a new model (CRM-ORG) and implications for sources of particle number, *J. Geophys. Res.*, 120, 10441–10464, <https://doi.org/10.1002/2015JD023551>, 2015.
- Newell, R. E., Thouret, V., Cho, J. Y. N., Stoller, P., Marengo, A., and Smit, H. G.: Ubiquity of quasi-horizontal layers in the troposphere, *Nature*, 398, 316–319, 1999.
- Ng, N. L., Canagaratna, M. R., Jimenez, J. L., Chhabra, P. S., Seinfeld, J. H., and Worsnop, D. R.: Changes in organic aerosol composition with aging inferred from aerosol mass spectra, *Atmos. Chem. Phys.*, 11, 6465–6474, <https://doi.org/10.5194/acp-11-6465-2011>, 2011.
- Öström, E., Putian, Z., Schurgers, G., Mishurov, M., Kivekäs, N., Lihavainen, H., Ehn, M., Rissanen, M. P., Kurtén, T., Boy, M., Swietlicki, E., and Roldin, P.: Modeling the role of highly oxidized multifunctional organic molecules for the growth of new particles over the boreal forest region, *Atmos. Chem. Phys.*, 17, 8887–8901, <https://doi.org/10.5194/acp-17-8887-2017>, 2017.
- Petters, M. D. and Kreidenweis, S. M.: A single parameter representation of hygroscopic growth and cloud condensation nucleus activity, *Atmos. Chem. Phys.*, 7, 1961–1971, <https://doi.org/10.5194/acp-7-1961-2007>, 2007.
- Petzold, A., Marsh, R., Johnson, M., Miller, M., Sevcenco, Y., Delhaye, D., Ibrahim, A., Williams, P., Bauer, H., Crayford, A., Bachalo, W. D., and Raper, D.: Evaluation of methods for measuring particulate matter emissions from gas turbines, *Environ. Sci. Technol.*, 45, 3562–3568, <https://doi.org/10.1021/es103969v>, 2011.
- Pöhlker, C., Wiedemann, K., Sinha, B., Shiraiwa, M., Gunthe, S., Smith, M., Su, H., Artaxo, P., Chen, Q., Cheng, Y., Elbert, W., Gilles, M. K., Kilcoyne, A. L. D., Moffet, R. C., Weigand, M., Martin, S. T., Pöschl, U., and Andreae, M. O.: Biogenic potassium salt particles as seeds for secondary organic aerosol in the Amazon, *Science*, 337, 1075–1078, 2012.
- Pöhlker, M. L., Pöhlker, C., Ditas, F., Klimach, T., Hrabě de Angelis, I., Araújo, A., Brito, J., Carbone, S., Cheng, Y., Chi, X., Ditz, R., Gunthe, S. S., Kesselmeier, J., Könemann, T., Lavrič, J. V., Martin, S. T., Mikhailov, E., Moran-Zuloaga, D., Rose, D., Saturno, J., Su, H., Thalman, R., Walter, D., Wang, J., Wolff, S., Barbosa, H. M. J., Artaxo, P., Andreae, M. O., and Pöschl, U.: Long-term observations of cloud condensation nuclei in the Amazon rain forest – Part 1: Aerosol size distribution, hygroscopicity, and new model parametrizations for CCN prediction, *Atmos. Chem. Phys.*, 16, 15709–15740, <https://doi.org/10.5194/acp-16-15709-2016>, 2016.
- Pöhlker, M. L., Ditas, F., Saturno, J., Klimach, T., Hrabě de Angelis, I., Araújo, A., Brito, J., Carbone, S., Cheng, Y., Chi, X., Ditz, R., Gunthe, S. S., Kandler, K., Kesselmeier, J., Könemann, T., Lavrič, J. V., Martin, S. T., Mikhailov, E., Moran-Zuloaga, D., Rizzo, L. V., Rose, D., Su, H., Thalman, R., Walter, D., Wang, J., Wolff, S., Barbosa, H. M. J., Artaxo, P., Andreae, M. O., Pöschl, U., and Pöhlker, C.: Long-term observations of cloud condensation nuclei in the Amazon rain forest – Part 2: Variability and characteristic differences under near-pristine, biomass burning, and long-range transport conditions, *Atmos. Chem. Phys. Discuss.*, <https://doi.org/10.5194/acp-2017-847>, in review, 2017.
- Pöschl, U., Martin, S. T., Sinha, B., Chen, Q., Gunthe, S. S., Huffman, J. A., Borrmann, S., Farmer, D. K., Garland, R. M., Helas, G., Jimenez, J. L., King, S. M., Manzi, A., Mikhailov, E., Pauliquevis, T., Petters, M. D., Prenni, A. J., Roldin, P., Rose, D., Schneider, J., Su, H., Zorn, S. R., Artaxo, P., and Andreae, M. O.: Rainforest aerosols as biogenic nuclei of clouds and precipitation in the Amazon: *Science*, 329, 1513–1516, 2010.
- Raes, F.: Entrainment of free tropospheric aerosols as a regulating mechanism for cloud condensation nuclei in the remote marine boundary layer, *J. Geophys. Res.*, 100, 2893–2903, 1995.
- Randel, W. J. and Jensen, E. J.: Physical processes in the tropical tropopause layer and their roles in a changing climate, *Nat. Geosci.*, 6, 169–176, <https://doi.org/10.1038/ngeo1733>, 2013.
- Reddington, C. L., Carslaw, K. S., Stier, P., Schutgens, N., Coe, H., Liu, D., Allan, J., Browse, J., Pringle, K. J., Lee, L. A., Yoshioka, M., Johnson, J. S., Regayre, L. A., Spracklen, D. V., Mann, G. W., Clarke, A., Hermann, M., Henning, S., Wex, H., Kristensen, T. B., Leaitch, W. R., Pöschl, U., Rose, D., Andreae, M. O., Schmale, J., Kondo, Y., Oshima, N., Schwarz, J. P., Nenes, A., Anderson, B., Roberts, G. C., Snider, J. R., Leck, C., Quinn, P. K., Chi, X., Ding, A., Jimenez, J. L., and Zhang, Q.: The Global Aerosol Synthesis and Science Project (GASSP) – Measurements and modelling to reduce uncertainty, *B. Am. Meteorol. Soc.*, 98, 1857–1877, <https://doi.org/10.1175/bams-d-15-00317.1>, 2017.
- Riccobono, F., Schobesberger, S., Scott, C. E., Dommen, J., Ortega, I. K., Rondo, L., Almeida, J., Amorim, A., Bianchi, F., Breitenlechner, M., David, A., Downard, A., Dunne, E. M., Duplissy, J., Ehrhart, S., Flagan, R. C., Franchin, A., Hansel, A., Junninen, H., Kajos, M., Keskinen, H., Kupc, A., Kürten, A., Kvashin, A. N., Laaksonen, A., Lehtipalo, K., Makhmutov, V., Mathot, S., Nieminen, T., Onnela, A., Petäjä, T., Praplan, A. P., Santos, F. D., Schallhart, S., Seinfeld, J. H., Sipilä, M., Spracklen, D. V., Stozhkov, Y., Stratmann, F., Tomé, A., Tsagkogeorgas, G., Vaattovaara, P., Viisanen, Y., Virtala, A., Wagner, P. E., Weingartner, E., Wex, H., Wimmer, D., Carslaw, K. S., Curtius, J., Donahue, N. M., Kirkby, J., Kulmala, M., Worsnop, D. R., and Bal-

- tensperger, U.: Oxidation products of biogenic emissions contribute to nucleation of atmospheric particles, *Science*, 344, 717–721, <https://doi.org/10.1126/science.1243527>, 2014.
- Riipinen, I., Pierce, J. R., Yli-Juuti, T., Nieminen, T., Hakkinen, S., Ehn, M., Junninen, H., Lehtipalo, K., Petaja, T., Slowik, J., Chang, R., Shantz, N. C., Abbatt, J., Leaitch, W. R., Kerminen, V. M., Worsnop, D. R., Pandis, S. N., Donahue, N. M., and Kulmala, M.: Organic condensation: a vital link connecting aerosol formation to cloud condensation nuclei (CCN) concentrations, *Atmos. Chem. Phys.*, 11, 3865–3878, <https://doi.org/10.5194/acp-11-3865-2011>, 2011.
- Riipinen, I., Yli-Juuti, T., Pierce, J. R., Petaja, T., Worsnop, D. R., Kulmala, M., and Donahue, N. M.: The contribution of organics to atmospheric nanoparticle growth, *Nat. Geosci.*, 5, 453–458, <https://doi.org/10.1038/ngeo1499>, 2012.
- Rissler, J., Vestin, A., Swietlicki, E., Fisch, G., Zhou, J., Artaxo, P., and Andreae, M. O.: Size distribution and hygroscopic properties of aerosol particles from dry-season biomass burning in Amazonia, *Atmos. Chem. Phys.*, 6, 471–491, <https://doi.org/10.5194/acp-6-471-2006>, 2006.
- Riuttanen, L., Bister, M., Kerminen, V. M., John, V. O., Sundstrom, A. M., Dal Maso, M., Raisanen, J., Sinclair, V. A., Makkonen, R., Xausa, F., de Leeuw, G., and Kulmala, M.: Observational evidence for aerosols increasing upper tropospheric humidity, *Atmos. Chem. Phys.*, 16, 14331–14342, <https://doi.org/10.5194/acp-16-14331-2016>, 2016.
- Rizzo, L. V., Artaxo, P., Müller, T., Wiedensohler, A., Paixão, M., Cirino, G. G., Arana, A., Swietlicki, E., Roldin, P., Fors, E. O., Wiedemann, K. T., Leal, L. S. M., and Kulmala, M.: Long term measurements of aerosol optical properties at a primary forest site in Amazonia, *Atmos. Chem. Phys.*, 13, 2391–2413, <https://doi.org/10.5194/acp-13-2391-2013>, 2013.
- Roberts, G. C. and Nenes, A.: A continuous-flow streamwise thermal-gradient CCN chamber for atmospheric measurements, *Aerosol Sci. Tech.*, 39, 206–221, 2005.
- Roberts, G. C., Andreae, M. O., Zhou, J., and Artaxo, P.: Cloud condensation nuclei in the Amazon Basin: “Marine” conditions over a continent?, *Geophys. Res. Lett.*, 28, 2807–2810, 2001.
- Robinson, N. H., Hamilton, J. F., Allan, J. D., Langford, B., Oram, D. E., Chen, Q., Docherty, K., Farmer, D. K., Jimenez, J. L., Ward, M. W., Hewitt, C. N., Barley, M. H., Jenkin, M. E., Rickard, A. R., Martin, S. T., McFiggans, G., and Coe, H.: Evidence for a significant proportion of Secondary Organic Aerosol from isoprene above a maritime tropical forest, *Atmos. Chem. Phys.*, 11, 1039–1050, <https://doi.org/10.5194/acp-11-1039-2011>, 2011.
- Rose, C., Sellegri, K., Moreno, I., Velarde, F., Ramonet, M., Weinhold, K., Krejci, R., Andrade, M., Wiedensohler, A., Ginot, P., and Laj, P.: CCN production by new particle formation in the free troposphere, *Atmos. Chem. Phys.*, 17, 1529–1541, <https://doi.org/10.5194/acp-17-1529-2017>, 2017.
- Rose, D., Gunthe, S. S., Mikhailov, E., Frank, G. P., Dusek, U., Andreae, M. O., and Pöschl, U.: Calibration and measurement uncertainties of a continuous-flow cloud condensation nuclei counter (DMT-CCNC): CCN activation of ammonium sulfate and sodium chloride aerosol particles in theory and experiment, *Atmos. Chem. Phys.*, 8, 1153–1179, <https://doi.org/10.5194/acp-8-1153-2008>, 2008.
- Rosenfeld, D., Lohmann, U., Raga, G. B., O’Dowd, C. D., Kulmala, M., Fuzzi, S., Reissell, A., and Andreae, M. O.: Flood or drought: How do aerosols affect precipitation?, *Science*, 321, 1309–1313, 2008.
- Rosenfeld, D., Andreae, M. O., Asmi, A., Chin, M., de Leeuw, G., Donovan, D. P., Kahn, R., Kinne, S., Kivekäs, N., Kulmala, M., Lau, W., Schmidt, K. S., Suni, T., Wagner, T., Wild, M., and Quaas, J.: Global observations of aerosol–cloud–precipitation–climate interactions, *Rev. Geophys.*, 52, 750–808, <https://doi.org/10.1002/2013RG000441>, 2014.
- Saha, S., Moorthi, S., Wu, X., Wang, J., Nadiga, S., Tripp, P., Behringer, D., Hou, Y.-T., Chuang, H.-y., Iredell, M., Ek, M., Meng, J., Yang, R., Mendez, M. P., v. d. Dool, H., Zhang, Q., Wang, W., Chen, M., and Becker, E.: NCEP Climate Forecast System Version 2 (CFSv2) 6-hourly Products, Research Data Archive at the National Center for Atmospheric Research, Computational and Information Systems Laboratory, <https://rda.ucar.edu/datasets/ds094.0/>, last access: 20 March 2017.
- Sahu, L. K. and Lal, S.: Changes in surface ozone levels due to convective downdrafts over the Bay of Bengal, *Geophys. Res. Lett.*, 33, L10807, <https://doi.org/10.1029/2006gl025994>, 2006.
- Schmale, J., Schneider, J., Jurkat, T., Voigt, C., Kalesse, H., Rautenhaus, M., Lichtenstern, M., Schlager, H., Ancellet, G., Arnold, F., Gerding, M., Mattis, I., Wendisch, M., and Borrmann, S.: Aerosol layers from the 2008 eruptions of Mount Okmok and Mount Kasatochi: In situ upper troposphere and lower stratosphere measurements of sulfate and organics over Europe, *J. Geophys. Res.*, 115, D00107, <https://doi.org/10.1029/2009jd013628>, 2010.
- Schneider, J., Weimer, S., Drewnick, F., Borrmann, S., Helas, G., Gwaze, P., Schmid, O., Andreae, M. O., and Kirchner, U.: Mass spectrometric analysis and aerodynamic properties of various types of combustion-derived aerosol particles, *Int. J. Mass Spectrom.*, 258, 37–49, 2006.
- Schulz, C., Schneider, J., Weinzierl, B., Sauer, D., Fütterer, D., Ziereis, H., and Borrmann, S.: Aircraft-based observations of IEPOX-derived isoprene SOA formation in the tropical upper troposphere in the Amazon region, *Atmos. Chem. Phys. Discuss.*, in preparation, 2018.
- Schwarz, J. P., Gao, R. S., Fahey, D. W., Thomson, D. S., Watts, L. A., Wilson, J. C., Reeves, J. M., Darbeheshti, M., Baumgardner, D. G., Kok, G. L., Chung, S. H., Schulz, M., Hendricks, J., Lauer, A., Karcher, B., Slowik, J. G., Rosenlof, K. H., Thompson, T. L., Langford, A. O., Loewenstein, M., and Aikin, K. C.: Single-particle measurements of midlatitude black carbon and light-scattering aerosols from the boundary layer to the lower stratosphere, *J. Geophys. Res.*, 111, D16207, <https://doi.org/10.1029/2006JD007076>, 2006.
- Schwarz, J. P., Weinzierl, B., Samset, B. H., Dollner, M., Heimerl, K., Markovic, M. Z., Perring, A. E., and Ziemba, L.: Aircraft measurements of black carbon vertical profiles show upper tropospheric variability and stability, *Geophys. Res. Lett.*, 44, 1132–1140, <https://doi.org/10.1002/2016GL071241>, 2017.
- Seibert, P. and Frank, A.: Source-receptor matrix calculation with a Lagrangian particle dispersion model in backward mode, *Atmos. Chem. Phys.*, 4, 51–63, <https://doi.org/10.5194/acp-4-51-2004>, 2004.

- Sherwood, S.: A microphysical connection among biomass burning, cumulus clouds, and stratospheric moisture, *Science*, 295, 1272–1275, 2002.
- Spracklen, D. V., Carslaw, K. S., Kulmala, M., Kerminen, V.-M., Mann, G. W., and Sihto, S.-L.: The contribution of boundary layer nucleation events to total particle concentrations on regional and global scales, *Atmos. Chem. Phys.*, 6, 5631–5648, <https://doi.org/10.5194/acp-6-5631-2006>, 2006.
- Stein, A. F., Draxler, R. R., Rolph, G. D., Stunder, B. J. B., Cohen, M. D., and Ngan, F.: NOAA's HYSPLIT atmospheric transport and dispersion modeling system, *B. Am. Meteorol. Soc.*, 96, 2059–2077, <https://doi.org/10.1175/BAMS-D-14-00110.1>, 2015.
- Stephens, M., Turner, N., and Sandberg, J.: Particle identification by laser-induced incandescence in a solid-state laser cavity, *Appl. Optics*, 42, 3726–3736, <https://doi.org/10.1364/ao.42.003726>, 2003.
- Stohl, A. and Thomson, D. J.: A density correction for Lagrangian particle dispersion models, *Bound.-Lay. Meteorol.*, 90, 155–167, <https://doi.org/10.1023/a:1001741110696>, 1999.
- Stohl, A., Hittenberger, M., and Wotawa, G.: Validation of the Lagrangian particle dispersion model FLEXPART against large-scale tracer experiment data, *Atmos. Environ.*, 32, 4245–4264, [https://doi.org/10.1016/s1352-2310\(98\)00184-8](https://doi.org/10.1016/s1352-2310(98)00184-8), 1998.
- Stohl, A., Eckhardt, S., Forster, C., James, P., Spichtinger, N., and Seibert, P.: A replacement for simple back trajectory calculations in the interpretation of atmospheric trace substance measurements, *Atmos. Environ.*, 36, 4635–4648, [https://doi.org/10.1016/s1352-2310\(02\)00416-8](https://doi.org/10.1016/s1352-2310(02)00416-8), 2002.
- Stohl, A., Forster, C., Frank, A., Seibert, P., and Wotawa, G.: Technical note: The Lagrangian particle dispersion model FLEXPART version 6.2, *Atmos. Chem. Phys.*, 5, 2461–2474, <https://doi.org/10.5194/acp-5-2461-2005>, 2005.
- Stolz, D. C., Rutledge, S. A., and Pierce, J. R.: Simultaneous influences of thermodynamics and aerosols on deep convection and lightning in the tropics, *J. Geophys. Res.*, 120, 6207–6231, <https://doi.org/10.1002/2014jd023033>, 2015.
- Talbot, R. W., Andreae, M. O., Andreae, T. W., and Harriss, R. C.: Regional aerosol chemistry of the Amazon Basin during the dry season, *J. Geophys. Res.*, 93, 1499–1508, 1988.
- Talbot, R. W., Andreae, M. O., Berresheim, H., Artaxo, P., Garstang, M., Harriss, R. C., Beecher, K. M., and Li, S. M.: Aerosol chemistry during the wet season in Central Amazonia: The influence of long-range transport, *J. Geophys. Res.*, 95, 16955–16969, 1990.
- Thalman, R., Thalman, R., de Sá, S. S., Palm, B. B., Barbosa, H. M. J., Pöhlker, M. L., Alexander, M. L., Brito, J., Carbone, S., Castillo, P., Day, D. A., Kuang, C., Manzi, A., Ng, N. L., Sedlacek III, A. J., Souza, R., Springston, S., Watson, T., Pöhlker, C., Pöschl, U., Andreae, M. O., Artaxo, P., Jimenez, J. L., Martin, S. T., and Wang, J.: CCN activity and organic hygroscopicity of aerosols downwind of an urban region in central Amazonia: Seasonal and diel variations and impact of anthropogenic emissions, *Atmos. Chem. Phys. Discuss.*, <https://doi.org/10.5194/acp-2017-251>, in review, 2017.
- Thornberry, T., Froyd, K. D., Murphy, D. M., Thomson, D. S., Anderson, B. E., Thornhill, K. L., and Winstead, E. L.: Persistence of organic carbon in heated aerosol residuals measured during Tropical Composition Cloud and Climate Coupling (TC4), *J. Geophys. Res.*, 115, D00J02, <https://doi.org/10.1029/2009jd012721>, 2010.
- Tröstl, J., Chuang, W. K., Gordon, H., Heinritzi, M., Yan, C., Molteni, U., Ahlm, L., Frege, C., Bianchi, F., Wagner, R., Simon, M., Lehtipalo, K., Williamson, C., Craven, J. S., Duplissy, J., Adamov, A., Almeida, J., Bernhammer, A.-K., Breitenlechner, M., Brilke, S., Dias, A., Ehrhart, S., Flagan, R. C., Franchin, A., Fuchs, C., Guida, R., Gysel, M., Hansel, A., Hoyle, C. R., Jokinen, T., Junninen, H., Kangasluoma, J., Keskinen, H., Kim, J., Krapf, M., Kürten, A., Laaksonen, A., Lawler, M., Leiminger, M., Mathot, S., Möhler, O., Nieminen, T., Onnela, A., Petäjä, T., Piel, F. M., Miettinen, P., Rissanen, M. P., Rondo, L., Sarnela, N., Schobesberger, S., Sengupta, K., Sipilä, M., Smith, J. N., Steiner, G., Tomè, A., Virtanen, A., Wagner, A. C., Weingartner, E., Wimmer, D., Winkler, P. M., Ye, P., Carslaw, K. S., Curtius, J., Dommen, J., Kirkby, J., Kulmala, M., Riipinen, I., Worsnop, D. R., Donahue, N. M., and Baltensperger, U.: The role of low-volatility organic compounds in initial particle growth in the atmosphere, *Nature*, 533, 527–531, <https://doi.org/10.1038/nature18271>, 2016.
- Twohy, C. H., Clement, C. F., Gandrud, B. W., Weinheimer, A. J., Campos, T. L., Baumgardner, D., Brune, W. H., Faloon, I., Sachse, G. W., Vay, S. A., and Tan, D.: Deep convection as a source of new particles in the mid-latitude upper troposphere, *J. Geophys. Res.*, 107, 4560, <https://doi.org/10.1029/2001JD000323>, 2002.
- Vestin, A., Rissler, J., Swietlicki, E., Frank, G., and Andreae, M. O.: Cloud nucleating properties of the Amazonian biomass burning aerosol: Cloud condensation nuclei measurements and modeling, *J. Geophys. Res.*, 112, D14201, <https://doi.org/10.1029/2006JD008104>, 2007.
- Virji, H.: A preliminary study of summertime tropospheric circulation patterns over South America estimated from cloud winds, *Mon. Weather Rev.*, 109, 599–610, 1981.
- Voigt, C., Schumann, U., Minikin, A., Abdelmonem, A., Afchine, A., Borrmann, S., Boettcher, M., Bucuchholz, B., Bugliaro, L., Costa, A., Curtius, J., Dollner, M., Doernbrack, A., Dreiling, V., Ebert, V., Ehrlich, A., Fix, A., Forster, L., Frank, F., Fuetterer, D., Giez, A., Graf, K., Grooss, J.-U., Gross, S., Heimerl, K., Heinold, B., Hueeneke, T., Jaervinen, E., Jurkat, T., Kaufmann, S., Kenttner, M., Klingebiel, M., Klimach, T., Kohl, R., Kraemer, M., Krisna, T. C., Luebke, A., Mayer, B., Mertes, S., Molleker, S., Petzold, A., Pfeilsticker, K., Port, M., Rapp, M., Reutter, P., Rolf, C., Rose, D., Sauer, D., Schaefer, A., Schlage, R., Schnaiter, M., Schneider, J., Spelten, N., Spichtinger, P., Stock, P., Walser, A., Weigel, R., Weinzierl, B., Wendisch, M., Werner, F., Wernli, H., Wirth, M., Zahn, A., Ziereis, H., and Zoger, M.: ML-CIRRUS: The airborne experiment on natural cirrus and contrail cirrus with the high-altitude long-range research aircraft HALO, *B. Am. Meteorol. Soc.*, 98, 271–288, <https://doi.org/10.1175/bams-d-15-00213.1>, 2017.
- von der Weiden, S. L., Drewnick, F., and Borrmann, S.: Particle Loss Calculator – a new software tool for the assessment of the performance of aerosol inlet systems, *Atmos. Meas. Tech.*, 2, 479–494, <https://doi.org/10.5194/amt-2-479-2009>, 2009.
- Waddicor, D. A., Vaughan, G., Choulaton, T. W., Bower, K. N., Coe, H., Gallagher, M., Williams, P. I., Flynn, M., Volz-Thomas, A., Pätz, H. W., Isaac, P., Hacker, J., Arnold, F., Schlager, H., and Whiteway, J. A.: Aerosol observations and growth rates

- downwind of the anvil of a deep tropical thunderstorm, *Atmos. Chem. Phys.*, 12, 6157–6172, <https://doi.org/10.5194/acp-12-6157-2012>, 2012.
- Walser, A., Sauer, D., Spanu, A., Gasteiger, J., and Weinzierl, B.: On the parametrization of optical particle counter response including instrument-induced broadening of size spectra and a self-consistent evaluation of calibration measurements, *Atmos. Meas. Tech.*, 10, 4341–4361, <https://doi.org/10.5194/amt-10-4341-2017>, 2017.
- Wang, H. and Fu, R.: The influence of Amazon rainfall on the Atlantic ITCZ through convectively coupled Kelvin waves, *J. Climate*, 20, 1188–1201, <https://doi.org/10.1175/jcli4061.1>, 2007.
- Wang, J., Krejci, R., Giangrande, S., Kuang, C., Barbosa, H. M. J., Brito, J., Carbone, S., Chi, X., Comstock, J., Ditas, F., Lavric, J., Manninen, H. E., Mei, F., Moran-Zuloaga, D., Pöhlker, C., Pöhlker, M. L., Saturno, J., Schmid, B., Souza, R. A. F., Springston, S. R., Tomlinson, J. M., Toto, T., Walter, D., Wimmer, D., Smith, J. N., Kulmala, M., Machado, L. A. T., Artaxo, P., Andreae, M. O., Petäjä, T., and Martin, S. T.: Amazon boundary layer aerosol concentration sustained by vertical transport during rainfall, *Nature*, 539, 416–419, <https://doi.org/10.1038/nature19819>, 2016.
- Wang, Q., Saturno, J., Chi, X., Walter, D., Lavric, J. V., Moran-Zuloaga, D., Ditas, F., Pöhlker, C., Brito, J., Carbone, S., Artaxo, P., and Andreae, M. O.: Modeling investigation of light-absorbing aerosols in the Amazon Basin during the wet season. *Atmos. Chem. Phys.*, 16, 14775–14794, <https://doi.org/10.5194/acp-16-14775-2016>, 2016.
- Watson, C. E., Fishman, J., and Reichle, H. G.: The significance of biomass burning as a source of carbon monoxide and ozone in the Southern Hemisphere tropics: A satellite analysis, *J. Geophys. Res.*, 95, 14443–14450, 1990.
- Weigel, R., Borrmann, S., Kazil, J., Minikin, A., Stohl, A., Wilson, J. C., Reeves, J. M., Kunkel, D., de Reus, M., Frey, W., Lovejoy, E. R., Volk, C. M., Viciani, S., D'Amato, F., Schiller, C., Peter, T., Schlager, H., Cairo, F., Law, K. S., Shur, G. N., Belyaev, G. V., and Curtius, J.: In situ observations of new particle formation in the tropical upper troposphere: the role of clouds and the nucleation mechanism, *Atmos. Chem. Phys.*, 11, 9983–10010, <https://doi.org/10.5194/acp-11-9983-2011>, 2011.
- Weigel, R., Spichtinger, P., Mahnke, C., Klingebiel, M., Afchine, A., Petzold, A., Krämer, M., Costa, A., Molleker, S., Reutter, P., Szakáll, M., Port, M., Grulich, L., Jurkat, T., Minikin, A., and Borrmann, S.: Thermodynamic correction of particle concentrations measured by underwing probes on fast-flying aircraft, *Atmos. Meas. Tech.*, 9, 5135–5162, <https://doi.org/10.5194/amt-9-5135-2016>, 2016.
- Weigelt, A., Hermann, M., van Velthoven, P. F. J., Brenninkmeijer, C. A. M., Schlaf, G., Zahn, A., and Wiedensohler, A.: Influence of clouds on aerosol particle number concentrations in the upper troposphere, *J. Geophys. Res.*, 114, D01204, <https://doi.org/10.1029/2008jd009805>, 2009.
- Weinzierl, B., Ansmann, A., Prospero, J. M., Althausen, D., Benker, N., Chouza, F., Dollner, M., Farrell, D., Fomba, W. K., Freudenthaler, V., Gasteiger, J., Gross, S., Haarig, M., Heinold, B., Kandler, K., Kristensen, T. B., Mayol-Bracero, O. L., Müller, T., Reitebuch, O., Sauer, D., Schafli, A., Schepanski, K., Spanu, A., Tegen, I., Toledano, C., and Walser, A.: The Saharan Aerosol Long-Range Transport and Aerosol–Cloud–Interaction Experiment: Overview and Selected Highlights, *B. Am. Meteorol. Soc.*, 98, 1427–1451, <https://doi.org/10.1175/bams-d-15-00142.1>, 2017.
- Wendisch, M., Pöschl, U., Andreae, M. O., Machado, L. A. T., Albrecht, R., Schlager, H., Rosenfeld, D., Martin, S. T., Abdelmonem, A., Afchine, A., Araújo, A. C., Artaxo, P., Aufmhoff, H., Barbosa, H. M. J., Borrmann, S., Braga, R., Buchholz, B., Cecchini, M. A., Costa, A., Curtius, J., Dollner, M., Dorf, M., Dreiling, V., Ebert, V., Ehrlich, A., Ewald, F., Fisch, G., Fix, A., Frank, F., Fütterer, D., Heckl, C., Heidelberg, F., Hüneke, T., Jäkel, E., Järvinen, E., Jurkat, T., Kanter, S., Kästner, U., Kenntner, M., Kesselmeier, J., Klimach, T., Knecht, M., Kohl, R., Kölling, T., Krämer, M., Krüger, M., Krisna, T. C., Lavric, J. V., Longo, K., Mahnke, C., Manzi, A. O., Mayer, B., Mertes, S., Minikin, A., Molleker, S., Münch, S., Nillius, B., Pfeilsticker, K., Pöhlker, C., Roiger, A., Rose, D., Rosenow, D., Sauer, D., Schnaiter, M., Schneider, J., Schulz, C., Souza, R. A. F. d., Spanu, A., Stock, P., Vila, D., Voigt, C., Walser, A., Walter, D., Weigel, R., Weinzierl, B., Werner, F., Yamasoe, M. A., Ziereis, H., Zinner, T., and Zöger, M.: ACRIDICON–CHUVA campaign: Studying tropical deep convective clouds and precipitation over Amazonia using the new German research aircraft HALO, *B. Am. Meteorol. Soc.*, 97, 1885–1908, <https://doi.org/10.1175/bams-d-14-00255.1>, 2016.
- Wiedensohler, A.: An approximation of the bipolar charge distribution for particles in the sub-micron size range, *J. Aerosol Sci.*, 19, 387–389, 1988.
- Wiedensohler, A., Ma, N., Birmili, W., Heintzenberg, J., Ditas, F., Andreae, M. O., and Panov, A.: Rare particle nucleation over remote forests, *Nature*, submitted, 2017.
- Williams, J., de Reus, M., Krejci, R., Fischer, H., and Ström, J.: Application of the variability-size relationship to atmospheric aerosol studies: estimating aerosol lifetimes and ages, *Atmos. Chem. Phys.*, 2, 133–145, <https://doi.org/10.5194/acp-2-133-2002>, 2002.
- Witte, K.: HALO Technical Note: Top Fuselage Aperture Plates – Particle Enrichment, DLR Flight Facility Oberpfaffenhofen, Weßling, Germany, p. 17, 2008.
- Yang, Q., Easter, R. C., Campuzano-Jost, P., Jimenez, J. L., Fast, J. D., Ghan, S. J., Wang, H., Berg, L. K., Barth, M. C., Liu, Y., Shrivastava, M. B., Singh, B., Morrison, H., Fan, J., Ziegler, C. L., Bela, M., Apel, E., Diskin, G. S., Mikoviny, T., and Wisthaler, A.: Aerosol transport and wet scavenging in deep convective clouds: A case study and model evaluation using a multiple passive tracer analysis approach, *J. Geophys. Res.*, 120, 8448–8468, <https://doi.org/10.1002/2015JD023647>, 2015.
- Yin, Y., Carslaw, K. S., and Feingold, G.: Vertical transport and processing of aerosols in a mixed-phase convective cloud and the feedback on cloud development, *Q. J. Roy. Meteorol. Soc.*, 131, 221–245, 2005.
- Young, L. H., Benson, D. R., Montanaro, W. M., Lee, S. H., Pan, L. L., Rogers, D. C., Jensen, J., Stith, J. L., Davis, C. A., Camos, T. L., Bowman, K. P., Cooper, W. A., and Lait, L. R.: Enhanced new particle formation observed in the northern midlatitude tropopause region, *J. Geophys. Res.*, 112, D10218, <https://doi.org/10.1029/2006jd008109>, 2007.
- Yu, F., Wang, Z., Luo, G., and Turco, R.: Ion-mediated nucleation as an important global source of tropospheric aerosols, *Atmos. Chem. Phys.*, 8, 2537–2554, <https://doi.org/10.5194/acp-8-2537-2008>, 2008.

- Yu, F., Luo, G., Nadykto, A. B., and Herb, J.: Impact of temperature dependence on the possible contribution of organics to new particle formation in the atmosphere, *Atmos. Chem. Phys.*, 17, 4997–5005, <https://doi.org/10.5194/acp-17-4997-2017>, 2017.
- Yu, P. F., Murphy, D. M., Portmann, R. W., Toon, O. B., Froyd, K. D., Rollins, A. W., Gao, R. S., and Rosenlof, K. H.: Radiative forcing from anthropogenic sulfur and organic emissions reaching the stratosphere, *Geophys. Res. Lett.*, 43, 9361–9367, <https://doi.org/10.1002/2016gl070153>, 2016.
- Zhou, J., Swietlicki, E., Hansson, H.-C., and Artaxo, P.: Submicrometer aerosol particle size distribution and hygroscopic growth measured in the Amazon rain forest during the wet season, *J. Geophys. Res.*, 107, 8055, <https://doi.org/10.129/2000JD000203>, 2002.
- Zhou, J. C., Swietlicki, E., Berg, O. H., Aalto, P. P., Hameri, K., Nilsson, E. D., and Leck, C.: Hygroscopic properties of aerosol particles over the central Arctic Ocean during summer, *J. Geophys. Res.*, 106, 32111–32123, 2001.
- Zhou, J. Y. and Lau, K. M.: Does a monsoon climate exist over South America?, *J. Climate*, 11, 1020–1040, 1998.
- Zhuang, Y., Fu, R., Marengo, J. A., and Wang, H.: Seasonal variation of shallow-to-deep convection transition and its link to the environmental conditions over the Central Amazon, *J. Geophys. Res.*, 122, 2649–2666, <https://doi.org/10.1002/2016JD025993>, 2017.
- Ziereis, H., Schlager, H., Schulte, P., van Velthoven, P. F. J., and Slemr, F.: Distributions of NO, NO_x, and NO_y in the upper troposphere and lower stratosphere between 28° and 61° N during POLINAT 2, *J. Geophys. Res.*, 105, 3653–3664, <https://doi.org/10.1029/1999jd900870>, 2000.
- Zipser, E. J.: Mesoscale and convective-scale downdrafts as distinct components of squall-line structure, *Mon. Weather Rev.*, 105, 1568–1589, [https://doi.org/10.1175/1520-0493\(1977\)105<1568:macdad>2.0.co;2](https://doi.org/10.1175/1520-0493(1977)105<1568:macdad>2.0.co;2), 1977.

Supplement of Atmos. Chem. Phys., 18, 921–961, 2018
<https://doi.org/10.5194/acp-18-921-2018-supplement>
© Author(s) 2018. This work is distributed under
the Creative Commons Attribution 4.0 License.



Supplement of

Aerosol characteristics and particle production in the upper troposphere over the Amazon Basin

Meinrat O. Andreae et al.

Correspondence to: Meinrat O. Andreae (m.andreae@mpic.de)

The copyright of individual parts of the supplement might differ from the CC BY 4.0 License.

Figure S1: Example of the center of a back-tracked parcel starting at the location of the HALO aircraft during flight AC18. This parcel started at 2014-09-28 20:34:53 UTC (same time as the HALO measurement) and was traced back in time in one-hour steps up to 120 hours, as shown in the time color scale on the right. The solid gray line is the full flight track of AC18. The top panel shows longitude vs. latitude and the bottom panel shows the longitude vs. altitude positions. We can see that this parcel stays in the UT within the 120 hours considered.

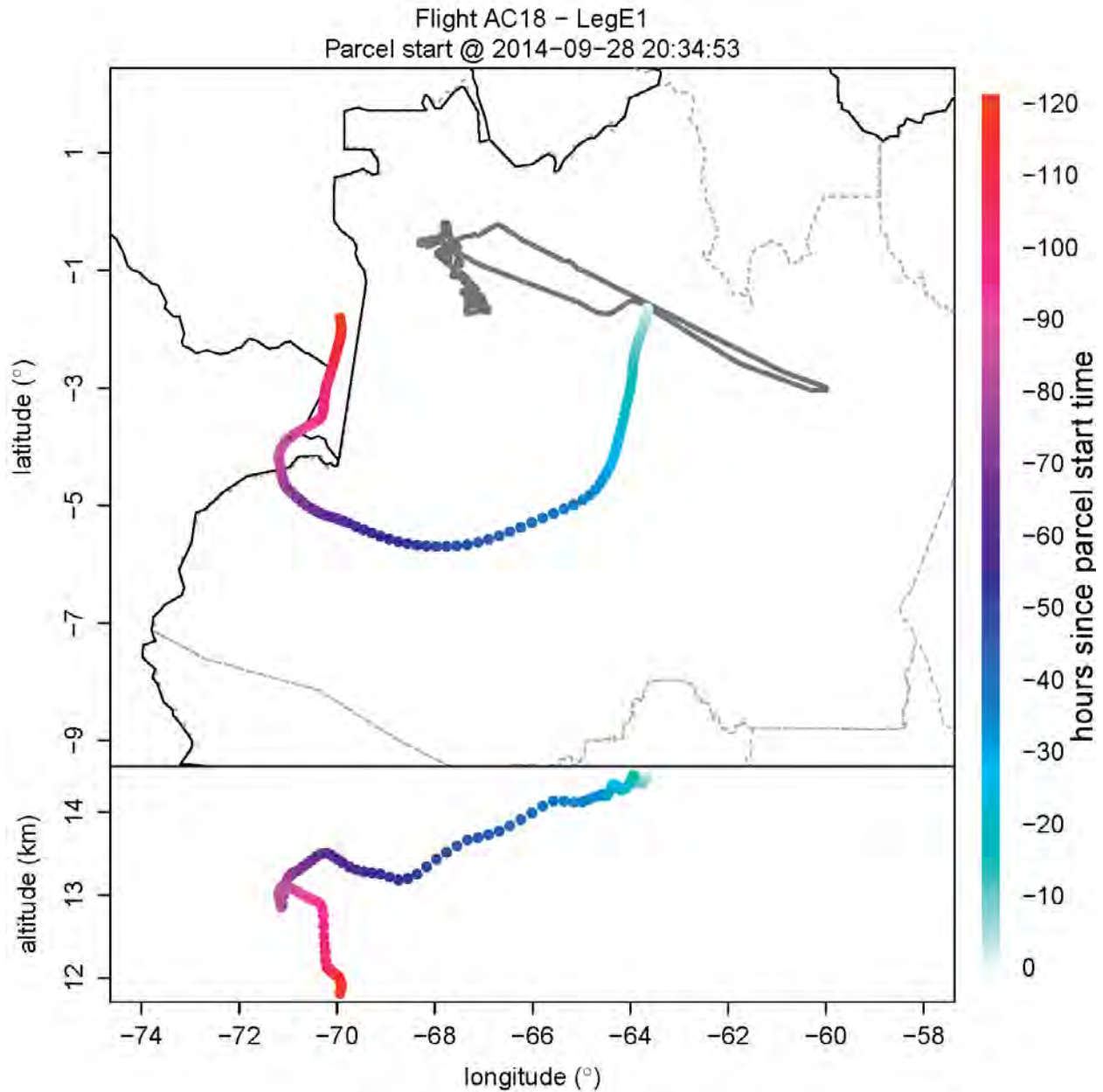


Figure S2: Examples of snapshots of the back-tracked parcel shown in Figure S1 matched in time to the closest GOES-13 infrared brightness temperature (T_b). Color dots are the same ones as in Figure S1, representing the position and backward time (in hours). Here the snapshots are zoomed in a $6^\circ \times 6^\circ$ box centered at the parcel location at the time shown on the top the snapshots and the number in parentheses is the number of hours backward from the parcel start (and flight measurement). Dashed boxes show the $1^\circ \times 1^\circ$ box centered in the back-tracked parcel within which we looked up the minimum T_b . This value is shown at the left bottom corner of each snapshot as well as the parcel altitude (in m) and GOES-13 infrared (IR) time.

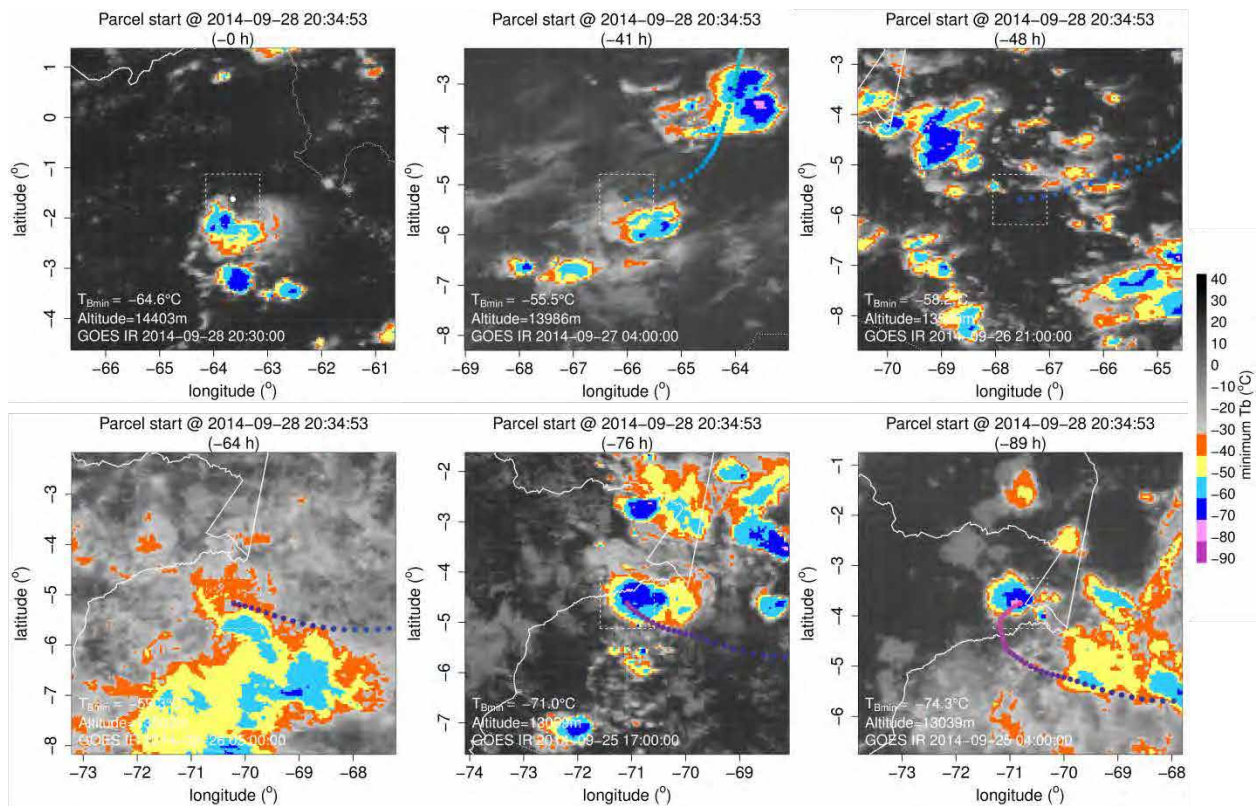


Figure S3: Summary of the back-tracked parcel positions (as in Fig. S1) with the minimum T_b tracked as shown in the snapshot examples of Figure S2. Here the back-track parcel position is colored with the value of minimum T_b found in the $1^\circ \times 1^\circ$ box.

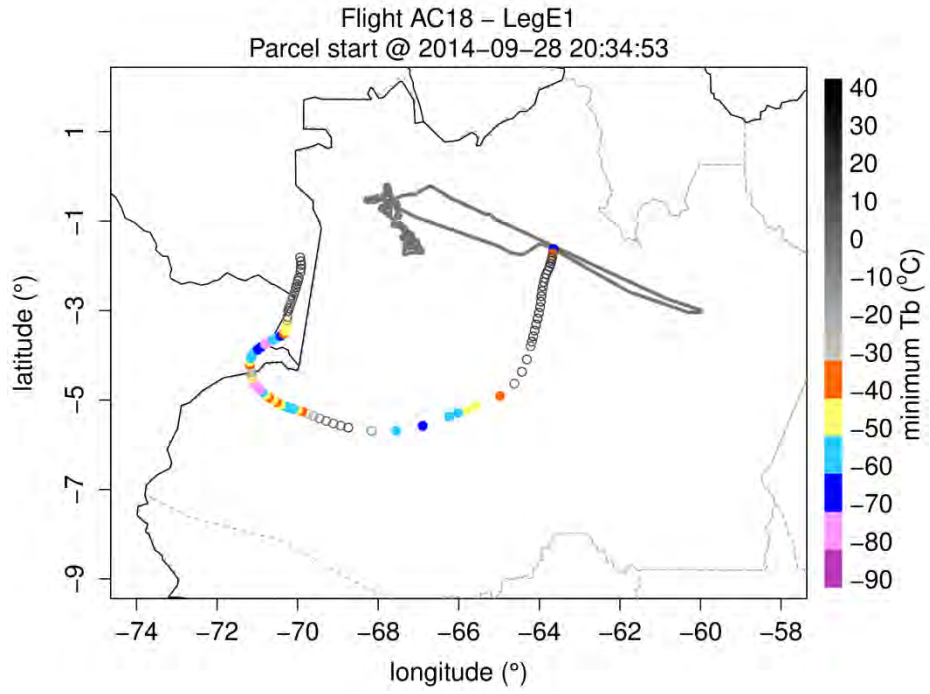


Figure S4. Mean vertical profiles of temperature, relative humidity and potential temperature (θ) from radiosoundings at Manacapuru.

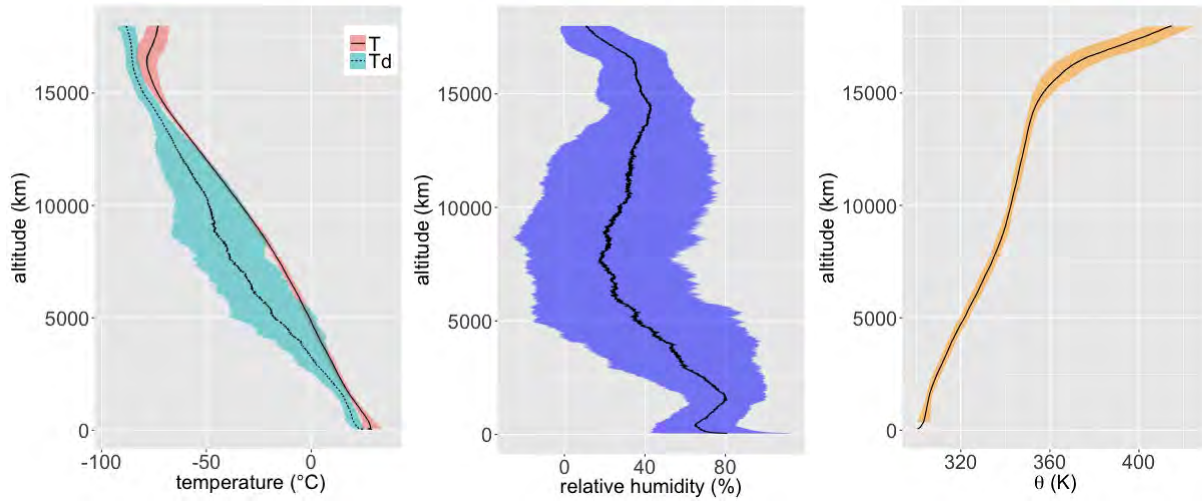
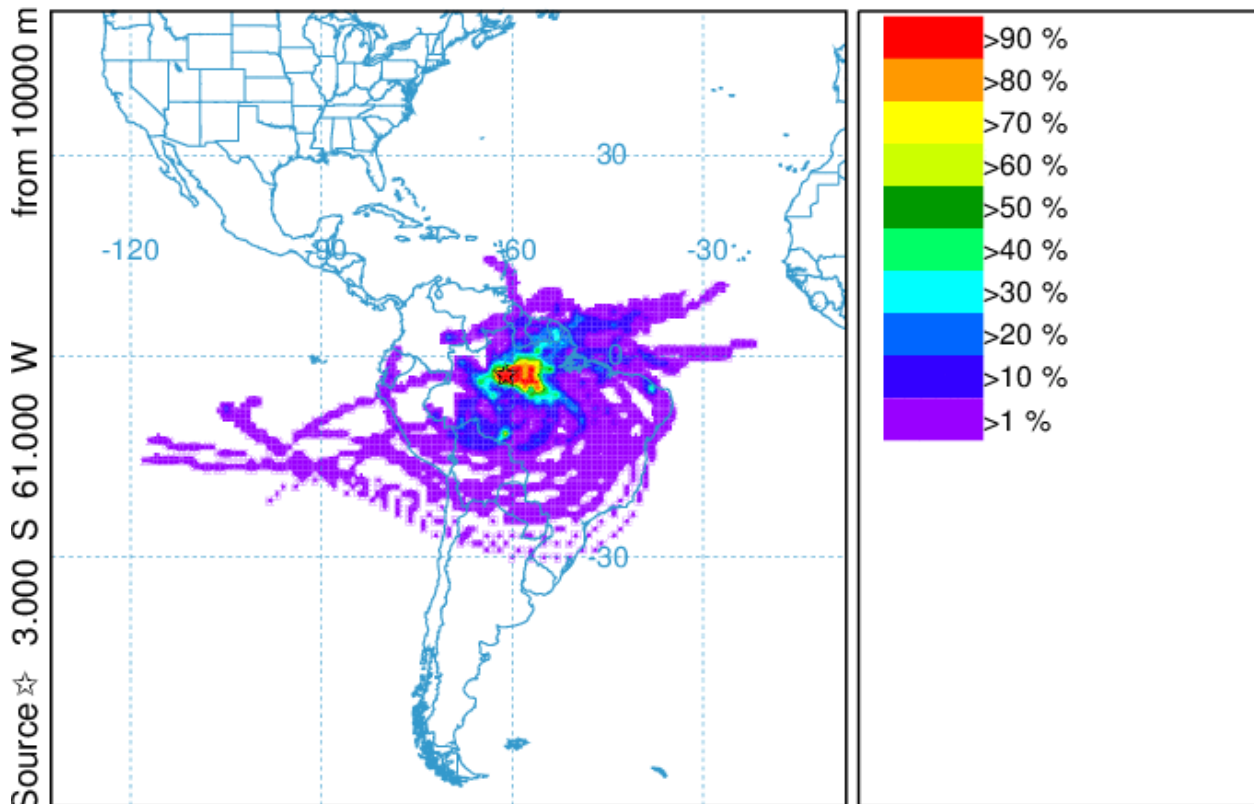


Figure S5: Trajectory statistics based on 120-hour backtrajectory calculations for September 2014, initialized at Manaus at an elevation of 10 km.

NOAA HYSPLIT MODEL - TRAJECTORY FREQUENCIES

endpts per grid sq./# trajectories (%) 0 m and 99999 m
Integrated from 2100 30 Sep to 0900 27 Aug 14 (UTC) [backward]
Freq Calculation started at 0000 00 00 (UTC)



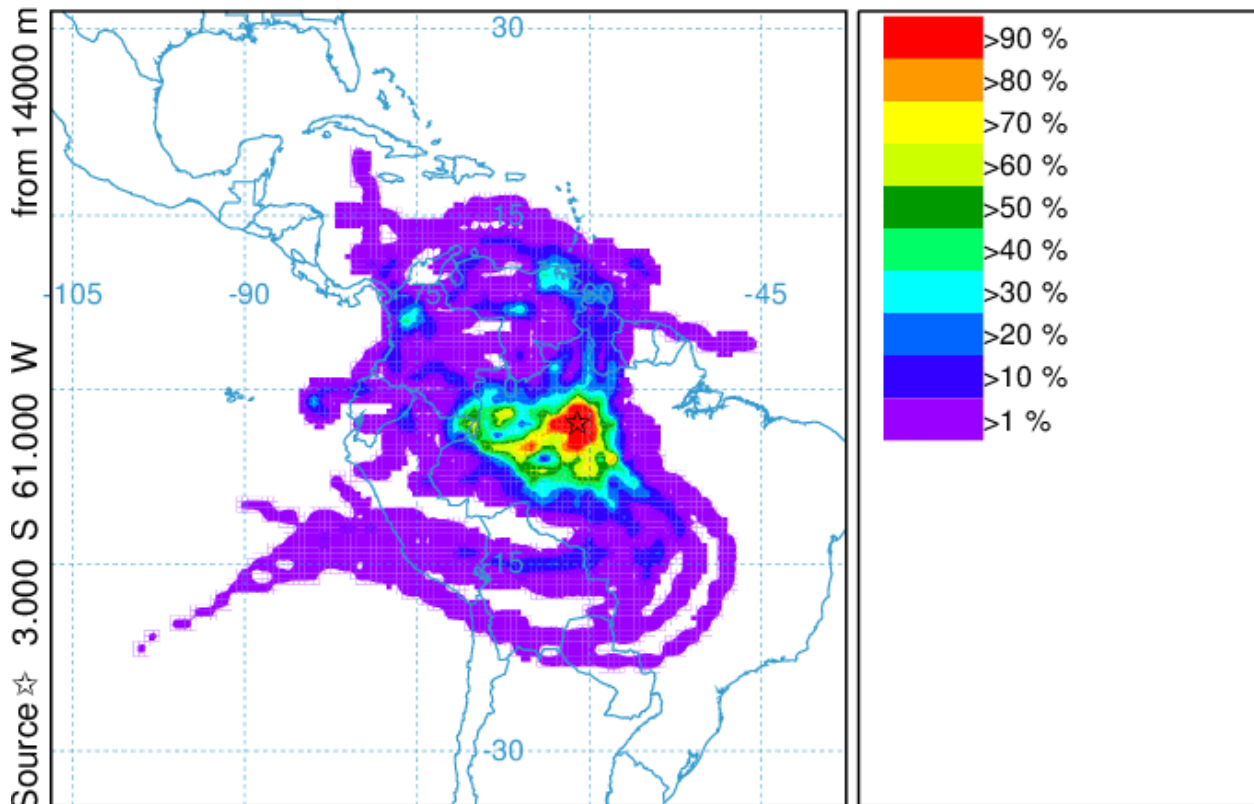
METEOROLOGICAL DATA

Job ID: 113173 Job Start: Wed Jan 11 22:11:28 UTC 2017
Source 1 lat.: -3.000000 lon.: -61.000000 height: 10000 m AMSL
Initial trajectory started: 2100Z 30 Sep 14
Direction of trajectories: Backward Trajectory Duration: 120 hrs
Frequency grid resolution: 1.0 x 1.0 degrees
Endpoint output frequency: 60 per hour
Number of trajectories used for this calculation: 60
Meteorology: 0000Z 29 Sep 2014 - GDAS1

Figure S6: Trajectory statistics based on 120-hour backtrajectory calculations for September 2014, initialized at Manaus at an elevation of 14 km.

NOAA HYSPLIT MODEL - TRAJECTORY FREQUENCIES

endpts per grid sq./# trajectories (%) 0 m and 99999 m
 Integrated from 2100 30 Sep to 0900 27 Aug 14 (UTC) [backward]
 Freq Calculation started at 0000 00 00 (UTC)



METEOROLOGICAL DATA

Job ID: 113224 Job Start: Wed Jan 11 22:18:03 UTC 2017
 Source 1 lat.: -3.000000 lon.: -61.000000 height: 14000 m AMSL
 Initial trajectory started: 2100Z 30 Sep 14
 Direction of trajectories: Backward Trajectory Duration: 120 hrs
 Frequency grid resolution: 1.0 x 1.0 degrees
 Endpoint output frequency: 60 per hour
 Number of trajectories used for this calculation: 60
 Meteorology: 0000Z 29 Sep 2014 - GDAS1

Figure S7: Time series plot of CN and CCN(0.52%) concentrations and flight altitude from flight AC09.

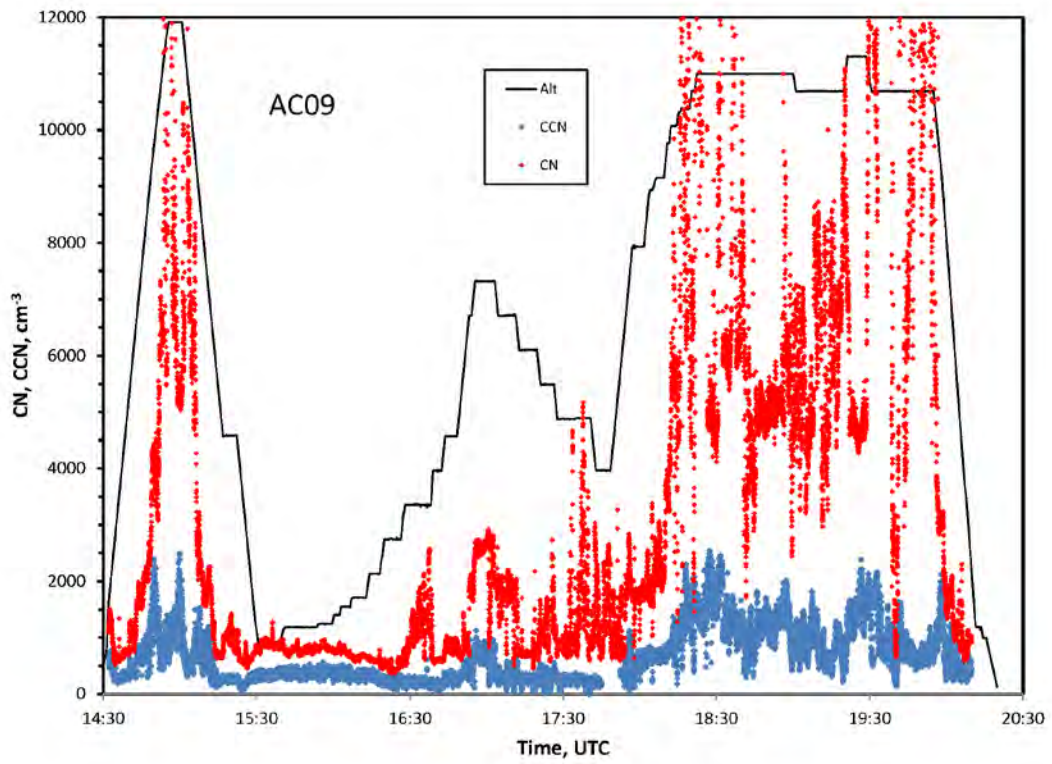


Figure S8: Scatter plot of CN vs O₃ concentrations from the UT in flight AC09.

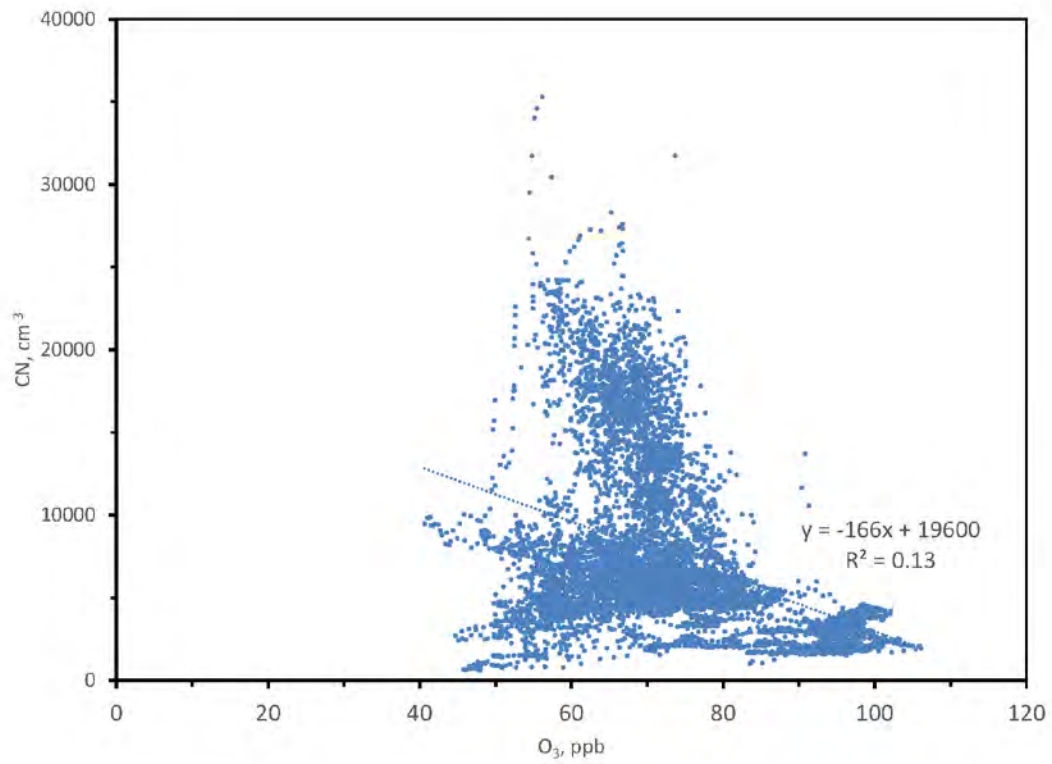


Table S1: Properties of the flight legs on which low aerosol concentrations were measured in the UT during ACRIDICON-CHUVA.

Flight	Leg	Start UTC	End UTC	Altitude range m	N _{CN} max. cm ⁻³	N _{CN} mean cm ⁻³	N _{CCN0.5} mean cm ⁻³	N _{acc} mean cm ⁻³	Ultrafine fraction	Trajectory type	Min T _b [min,max] ^a °C	Time since last DC [min,max] ^b hours	Time in DC [min,max] ^c hours	Sampling environment
AC16	L	16:23	16:30	12200-12600	3840	2460	169	142	0.94	B	[-62, -40]	[17, 18]	[5, 11]	clear air
AC18	L	15:17	15:19	9000-10500	1980	1620	487	236	0.85	C	[-2, 4.6]	-	-	clear air
AC19	L	20:14	20:23	11300-13800	2950	2160	834	207	0.90	A	[-74, -29]	[63, 104]	[3, 23]	clear air near outflow
AC20	L1	19:21	19:23	13600-13900	3040	1460	291	-	-	A	[-75, -70]	[0, 0]	[14, 16]	clear air near outflow
AC20	L2	19:33	19:35	14400	2190	1350	300	-	-	A	[-62, -61]	[0, 0]	[10, 12]	clear air near outflow
AC20	L3	19:52	19:57	14100	1950	1200	256	-	-	A	[-67, -68]	[0, 0]	[10, 13]	clear air near outflow

^{a)} Minimum and maximum temperature at top of most recent deep convection in grid boxes through which the center trajectories for the flight leg had passed.

^{b)} Trajectories were calculated for each minute of the leg, and for each trajectory the time between sampling and the most recent encounter with DC was determined. Given are the shortest and the longest of these time intervals.

^{c)} Minimum and maximum length of time that the trajectories from each leg had spent in grid boxes with DC.